Engineering DNA liquids towards macroscopic separation of biomolecules

Thesis by
Olivia Aoli Zou

In Partial Fulfillment of the Requirements for the
Degree of
Doctor of Philosophy

CALIFORNIA INSTITUTE OF TECHNOLOGY
Pasadena, California

2026
Defended November 18, 2025

Olivia Aoli Zou
ORCID: 0009-0007-1149-130X

ACKNOWLEDGEMENTS

The following acknowledgements could never fully convey my feelings to the individuals who have mentored, supported, and uplifted me during this academically grueling, yet rewarding journey. But I will do my best to express the love and gratitude I feel for them with these simple words.

From the moment I met him, my advisor Paul W. K. Rothemund was incredibly friendly and easy to talk to. I could converse with him for hours about science, philosophy, and life. I am grateful for the welcoming and supportive research environment he created and for treating me as an equal from day one. He gave me a lot of independence to do whatever I wanted and indulged me even when I was being stubborn on certain experiments. His mentorship and guidance helped me to grow into a confident and disciplined scientist, and I thank him for joining me on this wild ride of exploring DNA liquids.

My co-advisor, Lulu Qian, was the steady support I needed during scientifically and emotionally hard times. Whenever I show her my data, I am always amazed at how she cuts through all the fog surrounding it and points out the most salient details. I can only hope to someday develop the same level of acumen that she has. I also greatly appreciate all her efforts in organizing lab lunches, snacks, and Fika— all these events helped to build a wonderful lab culture and bring everyone together. I thank the rest of my committee members— Erik Winfree, Niles Pierce, and Deborah Fygenson— for all their mentorship and guidance throughout the years.

Once upon a time, the Rothemund group was a six member body. I am eternally grateful to the former postdocs— Byoung-jin Jeon, Jaimie Stewart, Vishal Maingi, and Tyler Ross— for being so welcoming at the beginning of my journey and for helping me get my research off the ground with the feedback and lessons they taught me. Thank you especially to Tyler, who was essentially my desk-mate during the pandemic, for commiserating with me endlessly, inviting me on hikes, and exploring boba shops with me.

Matteo Guareschi and I were in the same bioengineering cohort and we joined the Rothemund lab together when we started. We took many classes together, did problem sets together, and probably played way too much Bananagrams together. We shared so many ups and downs during our time here. He was always the calm to my storm; if there was ever an issue in the lab, Matteo would deftly and calmly

take care of it while I ran around like a headless chicken. I am so grateful for his friendship and support; it has made all the difference during my time here.

I have had the privilege of working with one of the nicest communities here at Caltech— the molecular programming groups which include the Winfree and Qian labs. I thank all lab members, past and present, for the thought-provoking conversations, feedback on research, pizza nights at Settebello, Fika, karaoke, and the infinite Bananagrams and Hanabi gaming sessions. I truly feel blessed to have had the chance to work with such wonderful people, and every single one of them inspires me to be a better scientist. I would especially like to thank Salvador Buse for always making me laugh with his stories, Cameron Chalk for yapping with me to no end, and Yancheng Du for all the fun adventures we embark on.

I would like to thank the Sloan collaboration group, which includes the labs of Deborah Fygenson from UCSB, Elisa Franco from UCLA, and Rebecca Schulman from Johns Hopkins. The collaboration was a rich and thought-provoking environment to discuss research with so many others who also worked on condensates.

I would also like to thank Jillian Blatti and the PCC nanostars for giving me the opportunity to translate my research into an educational setting. I have learned so much as a teacher, and Jillian has inspired me to explore careers outside of the traditional academic setting. I would also like to thank Heather Romero, who was my partner in crime every summer, for helping me lay the foundation for the annual summer bootcamp at UCLA.

Thank you to all my friends here in California and on the east coast for lifting me up during my time here: Manisha, Andrey, Eli, Janice, Claire, Michelle, Annie, Meredith, Dani, Rowan, Melissa, and Molly. Manisha was a wonderful roommate and is an incredible friend and exceptional scientist. We have so many fun adventures together, and she inspires me to be a better scientist and person every day. Her husband Andrey has also been a wonderful friend to go on adventures and play board games with. Eli is one of my dearest friends from college who somehow also ended up being part of the Sloan collaboration when he joined Rebecca Schulman's group (it was difficult not to yell at each other during Sloan meetings). He is one of the few friends that I can call at any time to talk about anything, whether it is about science or life, and I know that he will always pick up the phone and listen. His friendship means the world to me.

I must also thank W. Benjamin Rogers, who was my undergraduate thesis advisor

at Brandeis. He was the first person to tell me that I should go to graduate school and laid the foundations for me to become a scientist. Without his encouragement, I may have ended up miserably going to medical school instead.

And finally, my family. My aunt, uncle, and cousin Dongyi always welcomed me to the Bay Area for Thanksgiving and was my home away from home during my time here. Their cat Ninja (RIP) was the best kitty to ever exist and provided great emotional support through cuddles during some hard times. My parents and my brother have given me endless support and infinite love. I owe everything I am to them. Mom, Dad, and Ben: I love you very much. If multiple lifetimes existed, I would choose to be your daughter and sister in all of them. Thank you for being my family.

ABSTRACT

Liquid-liquid phase separation (LLPS) is a thermodynamic process by which a mixture of solutions de-mixes into separate, coexisting phases. In cells, macromolecules such as proteins and nucleic acids can undergo LLPS to form membraneless structures known as biomolecular condensates. These condensates are usually liquid-like droplets highly concentrated in the species they are composed of. Condensates are crucial to many cellular processes and functions, such as protein assembly, gene regulation, subcellular organization, storage, and stress response. On a larger scale, condensates are also implicated in various neurodegenerative diseases, such as Huntington's and Alzheimer's disease.

DNA condensates are easy to engineer due to the programmable nature of the molecule. DNA nanostars are multi-armed junctions with double-stranded arms and typically single-stranded, palindromic overhangs or 'sticky ends' that allow for transient interactions between the molecules. They can phase-separate to form liquid-like droplets at the microscopic scale. Centrifugation of a high concentration solution of nanostars coalesces condensates into a macroscopic liquid that is visible to the naked eye.

In biology, one of the key functions of condensates is to act as compartments and localize various molecules, such as enzymes and nucleic acids. Our goal is to engineer macroscopic DNA liquids to similarly act as compartments that can separate multiple biomolecular targets. We propose that these macroscopic DNA liquids are a potentially novel method for multiplexed separation that is fast, simple to use, and biocompatible with various high-value targets, such as protein therapeutics.

We designed multiple immiscible DNA liquids of different densities to act as macroscopic compartments. We present a set of design principles for engineering nanostars to create liquid layers in a microcentrifuge tube. We show via UV absorbance measurements how various nanostar features, such as arm length, sticky end strength, and valency, affect liquid phase density, which determines the order of layering between liquids. We further show that the interface quality between pairwise liquids is determined by a combination of density differences between liquids and the orthogonality of nanostar sticky ends, and we devise a metric to calculate this orthogonality. Using these design principles, we are currently able to create up to five orthogonal liquid layers in a tube.

With these DNA liquid layers, we envision separation to be a two step process. The first step is to localize specific target biomolecules into these layers. We demonstrate localization of oligos in a multilayer DNA liquid system by modifying nanostars with tag regions complementary to the target strand. We also demonstrate localization of fluorescent streptavidin to a single DNA liquid layer by modifying nanostars with a streptavidin-binding aptamer. The second step is to release targets from the liquid layers so that they can be collected for downstream use. After localization of the aforementioned targets, we added strands complementary to either the tag region or the aptamer. This causes targets to be displaced from their binding moiety and released into the supernatant.

TABLE OF CONTENTS

LIST OF ILLUSTRATIONS

LIST OF TABLES

Chapter 1

INTRODUCTION

The motivation behind this thesis draws from a number of sources. We were inspired by the inherent ability of condensates to act as compartments, by the simple programmability of DNA, and by the continual pursuit to improve current challenges in separation methods. The aim of this introductory chapter is to explain how these concepts meld together to form our goal of engineering DNA liquids as a possible novel separation method, which I will explain in Section 1.5.

I will begin by reviewing the history of biomolecular condensates and impress upon the reader the significance of how condensates can act as compartments and why we take advantage of this feature. I will then briefly discuss the history and principles of DNA nanotechnology to explain our choice in condensate material. Finally, I will examine the challenges of current separation techniques and discuss how our proposed method potentially addresses those issues.

1.1 Biomolecular condensates

Liquid-liquid phase separation (LLPS) is a thermodynamic process by which a mixture of solutions de-mixes into separate, coexisting phases. The most common example of this phenomenon is when one mixes oil and water together and observes that the two liquids do not mix. The separation of oil and water is a result of hydrophobic interactions, but LLPS can be driven by many other factors, such as temperature, pressure, and electrostatic interactions (Xu et al., 2023). While we usually consider phase separation in everyday examples such as salad dressings and peanut butter, there has been growing evidence in the past decade that LLPS plays an important role in cells.

Spatial organization within cells is crucial to allow for control of complex biochemical reactions. We are often taught that membrane bound organelles, such as the mitochondria or endoplasmic reticulum, are the main forms of subcellular organization. However, recent discoveries demonstrate that cells are capable of forming membraneless organelles via LLPS. Macromolecules such as proteins and nucleic acids can undergo LLPS to form membraneless structures known as biomolecular condensates. These condensates are usually liquid-like droplets highly concentrated

in the species they are composed of. The droplets are typically called the dense phase and can coexist with the surrounding dilute phase (Alberti, Gladfelter, and Mittag, 2019). Condensates are crucial to many cellular processes and functions, such as protein assembly, gene regulation, subcellular organization, storage, and stress response (Lyon, Peeples, and Rosen, 2021). On a larger scale, condensates are also implicated in various neurodegenerative diseases, such as Huntington's and Alzheimer's disease (Alberti and Hyman, 2021).

The first known observation of a membraneless structure was in the 1830s when scientists observed what would be called the nucleolus inside a neuron cell (Wagner, 1835; Valentin, 1837). In the decades that followed, many membraneless structures were observed, but the physical process behind how they formed was not well understood. In 2009, Clifford P. Brangwynne's seminal paper on the condensation of P granules provided the foundation for this understanding (Brangwynne et al., 2009). He observed that P granules—membraneless structures composed of RNA and proteins—in the germ cells of *C. elegans* were able to undergo shear, flow, and fusion. These observations led to the conclusion that P granules are a liquid-like material and form via separation from the surrounding cytoplasm. Since then, a number of studies have revealed many membraneless structures that form via LLPS, such as clusters of signaling proteins in kidney podocytes (Li et al., 2012), nucleolar subcompartments (Feric et al., 2016), and DNA damage repair sites (Patel et al., 2015).

Beyond studying the biological function of phase-separated structures *in vivo*, researchers have designed many *in vitro* systems of artificial phase separating biomolecules, which usually consist of proteins and/or RNA. Proteins that undergo LLPS tend to be intrinsically disordered proteins (IDPs) that either completely or partially lack a fixed structure. Engineering IDPs to control condensate formation can lead to many exciting new applications. Simon et al. developed an artificial protocell that contained thermally responsive, phase-separating IDPs that co-separate with RNA and can programmatically inhibit translation (Simon et al., 2019). Dzuricky et al. designed artificial IDPs that are capable of sequestering enzymes and controlling catalytic rates via the molecular properties of these artificial IDPs (Dzuricky et al., 2020). Clearly, there are many exciting avenues to explore with biomolecular condensates, both *in vivo* and *in vitro*.

A through line in this discussion is the idea that condensates naturally act as compartments. As mentioned earlier, condensates are sometimes known as membrane-

less organelles, and organelles are considered to be compartments that perform specialized functions in the cell. Biologically or synthetically, condensates have demonstrated their ability to sequester various cargo (Li et al., 2012; Dzuricky et al., 2020). We therefore want to take advantage of this natural feature and engineer condensates to sequester high-value target proteins of interest.

1.2 DNA nanotechnology

We now pivot to a brief discussion on the history of DNA nanotechnology. In the previous section, we established that both biology and scientists have mainly focused on protein and/or RNA-based condensates. Why, then, are we interested in engineering DNA condensates?

DNA is widely known as a biomolecule that encodes the genetic information of our cells. Generally composed of two strands that bind to each other in a double helical fashion, DNA is also a versatile molecule that has a wide range of applications. Strands are composed of four nitrogenous bases—adenine (A), thymine (T), cytosine (C) and guanine (G)—that bind specifically to each other (A-T and C-G) in what is known as Watson-Crick basepairing. This specific basepairing, along with the ease of chemically synthesizing the molecule, makes DNA an easily programmable, structural material. Examples such as DNA origami, DNA tiling, strand displacement circuits, and others (Rothemund, 2006; Qian and Winfree, 2011; Ke et al., 2012; Evans and Winfree, 2017) demonstrate how rational design of DNA sequences can lead to powerful and useful structures for engineering applications.

In comparison to DNA, proteins and RNA are more difficult and costly to synthesize and are not as chemically stable. Given these advantages and well-established principles of DNA as a structural material, we naturally gravitate to this particular nucleic acid as the material of choice to form condensates.

1.3 Nanostars and DNA condensates

Biffi *et al.* (Biffi et al., 2013) were the first to demonstrate phase separation of a programmable DNA structure, which they termed a 'nanostar', to form DNA condensates. Nanostars are multi-armed junctions with double-stranded arms and typically single-stranded, palindromic overhangs or 'sticky ends' (SE) that allow for transient interactions between the molecules (Fig 1.1). They can phase-separate to form either liquid or gel-like condensates. Colloquially, we follow the convention in literature and call the dense and dilute phases as the liquid phase and gas phase, respectively.

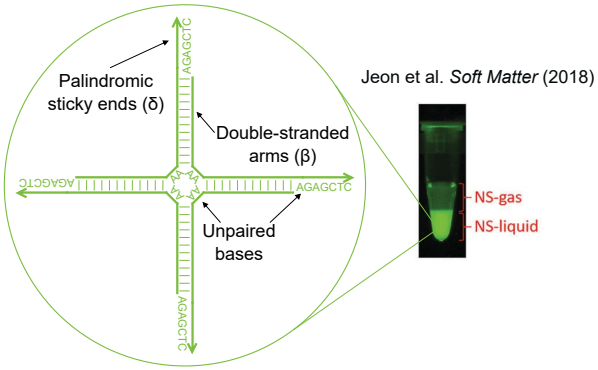

Figure 1.1: Nanostar structure. Nanostars are multi-armed junctions with double stranded arms (β = arm length in bp) that transiently interact via palindromic SEs (δ = SE identifier. See Table 1.1. The SE in this schematic is SE34). The unpaired bases in the center and between the arm and SE provide flexibility to the structure. Centrifugation of a high concentration solution of nanostars coalesces the liquid droplets into millimeter sized liquids.

Biffi *et al.* demonstrate phase separation of two nanostars of different valencies and show that decreasing valency decreases the critical concentration and temperature for phase separation. Many studies have followed since that focused on understanding various aspects of the nanostar structure, such as understanding phase behavior via coarse-grained models (Rovigatti, Bomboi, and Sciortino, 2014; Rovigatti, Smallenburg, and Romano, 2014; Locatelli et al., 2017), experimentally mapping phase diagrams (N. Conrad et al., 2019; Nathaniel Conrad et al., 2022; Hegde et al., 2024), and studying the influence of various nanostar architectures on the material properties of condensates (Dan T. Nguyen and Omar A. Saleh, 2017; Lee et al., 2021; Jeon, D. T. Nguyen, Abraham, et al., 2018; D. T. Nguyen et al., 2019; Sato, Sakamto, and Takinoue, 2020; Agarwal, Osmanovic, Klocke, et al., 2022). There are also many studies that demonstrate engineering of nanostars to perform interesting behaviors, such as formation of core-shell or Janus-like particles (Jeon, D. T. Nguyen, and O. A. Saleh, 2020; Sato, Sakamto, and Takinoue, 2020; Skipper and Wickham, 2024), control of condensate growth via biochemical factors (Agarwal, Osmanovic, Dizani, et al., 2024), localization of transcription within droplets (Kengmana et al., 2024) and design of droplets capable of performing computations (Do et al., 2022; Gong et al., 2022).

Of particular interest to us are studies that demonstrate engineering of nanostars to form condensates that compartmentalize various cargo. Nguyen *et al.* partitioned long double-stranded DNA (on the order of a few hundred basepairs in length) into droplets of DNA nanostars (D. T. Nguyen et al., 2019). Interestingly, double-

stranded DNA can localize within droplets up to a certain length. Longer lengths required stronger binding affinities between the nanostar and the DNA, but would result in a secondary phase separation of the DNA within droplets depending on experimental conditions. Sato *et al.* localized streptavidin inside droplets by binding streptavidin to biotinylated DNA, which was complementary to the sticky ends of the nanostars (Sato, Sakamto, and Takinoue, 2020). By changing the sequence of the biotinylated DNA, they were able to demonstrate selective partitioning of the protein into orthogonal droplets. Dizani *et al.* similarly localized streptavidin into condensates, but used an RNA aptamer bound to the DNA nanostars to recruit cargo (Dizani et al., 2024). In all of these cases, compartmentalization occurred in micron-sized droplets, which is analogous to how biomolecular condensates perform in cells.

Most studies focus on creating micron-sized droplets with these nanostars. It is possible, however, to scale up the concentration of nanostars to create millimeter-sized DNA liquids in a microcentrifuge tube (Fig 1.1), as demonstrated by Jeon *et al.* (Jeon, D. T. Nguyen, Abraham, et al., 2018). Centrifugation of this high concentration solution of nanostars coalesces condensates into a macroscopic liquid at the bottom of the tube that is visible to the naked eye. As will be explained in Section 1.5, we will use this macroscopic DNA liquid architecture to localize cargo.

1.4 Current separation techniques for biomolecules

Separation and extraction techniques are abundant and ubiquitous in chemistry and biology fields, as the need to isolate and purify compounds is crucial for downstream processes and/or usage. In pharmaceuticals, purification of protein therapeutics is of utmost importance. Protein therapeutics are proteins that are designed for the treatment of various diseases. Common examples of protein therapeutics are antibodies, albumin, coagulation factors, and hormones such as insulin. All of these are used in the treatment of diseases such as cancer, diabetes, anemia, and more. Due to their medical applications, the purity requirements for protein therapeutics are quite stringent. In fact, the purification processes for such drugs cost more than $40 billion per year and are the main cost of manufacturing (Decker et al., 2024). As a result, improvement of purification processes to make them more efficient and low cost is an ongoing effort by many.

Protein purification can involve many steps and many types of purification processes. Most processes initially involve a rough fractionation step, where the majority of

contaminants, such as cell debris, nucleic acids, and lipids, will be removed from the cell extract. Typically, this would involve using low resolution techniques such as precipitation or centrifugation, as these kinds of processes are low cost and simple to employ. After removal of most contaminants, what is leftover is the protein of interest along with harder to remove impurities or other proteins that are similar in characteristic to the target one. The purification process now moves on to a fine fractionation step to obtain higher purity. This would typically involve chromatographic methods, such as ion-exchange or affinity chromatography. Chromatography involves flowing the protein mixture through a stationary material—most often a column—that is embedded with a substrate or ligand that has an affinity with the protein of interest. In this way, other contaminants can flow or be washed through the column and leave just the target protein behind. The target can then be collected by washing the column with an elution buffer (Du et al., 2022).

Of all the chromatographic techniques, affinity chromatography provides the highest form of specificity. It relies on specific binding interactions between the protein of interest and a substrate embedded in the column. Common examples of embedded substrates are enzymes, antigens, nucleic acids, metal ion chelates, aptamers, and more (Rodriguez et al., 2020). Aptamer-based affinity chromatography has been growing in popularity for its many advantages over other types of chromatographic methods. Aptamers are synthetic oligonucleotides that are designed to bind to a specific target molecule. They are capable of binding to small molecules, proteins, and even whole cells. Selection of aptamer sequences is made possible by a method known as systematic evolution of ligands by exponential enrichment (SELEX), which not only allows for selection for a specific target, but also allows for counter selection against proteins that are similar in charactersitic to the target of interest. This allows for highly increased specificity between the aptamer and target. Compared to protein-based ligands, aptamers are easier and cheaper to synthesize and are more tolerant to caustic conditions. In addition, aptamers are biocompatible with protein targets and would not lead to poisoning of proteins via use of toxic metal ions. However, like most chromatographic techniques, aptamer-based affinity chromatography requires the use of a column upon which the oligonucleotides will be grafted on to. These columns can not only be expensive, but the binding capacity of aptamers to the column and the duration of binding are still not well known (Gérald Perret and Egisto Boschetti, 2018).

While chromatography is the standard method for protein purification, the cost

of the columns used in such processes can be exorbitant. In fact, these columns are the major cost driver in purification processes (Decker et al., 2024). While the high specificity and advantages of chromatographic methods cannot be denied, alternative purification methods that are lower in cost and produce similar protein purity levels are being explored. One possible method is purification via phase separation. Utilizing phase separation as a purification technique is not novel. In fact, chemists have long performed liquid-liquid extractions via separatory funnels to purify and separate mixtures of solutes. Purifying proteins via phase separation is a growing technique of interest not just in academia but also in industrial sectors. Plasma proteins and insulin are some examples of protein therapeutics that are purified in this manner (Burnouf, 2007; dos Santos, Carvalho, and Roque, 2017). The most common reagents used in such processes are a mixture of polymers and inorganic salts, but reagents range from using solutions of polyelectrolytes to alcohol to surfactants (Decker et al., 2024). While the cost-effectiveness of these phase separation processes in comparison to chromatographic ones is still unclear, the diversity of phase separating agents, the rapid separation that can occur on the order of minutes, and the inexpensive reagents and equipment involved make phase separation processes an attractive alternative (Decker et al., 2024).

1.5 Summary of thesis

Let us briefly summarize what we have learned in the previous sections. Biomolecular condensates arise out of phase separation and are capable of acting as compartments. Synthetic DNA condensates can be formed from DNA nanostars and can be engineered to localize various cargo, which most studies currently focus on performing at the microscopic scale. Phase separation as a purification or separation technique is growing in popularity for the reasons listed in Section 1.4.

The goal of this work is to engineer DNA nanostars to form macroscopic DNA liquids that can separate multiple biomolecular targets (Fig 1.2). By attaching aptamers to DNA nanostars, these nanostar-aptamer complexes can bind to a target of interest via the aptamer and then sequester it into a condensate upon phase separation of the nanostar. This novel separation technique can be considered an amalgamation of aptamer-based affinity chromatography and liquid-liquid extraction via separatory funnels. The use of aptamers provides specificity to targets that low resolution liquid-liquid extraction techniques usually do not have. The use of a phase-separating monomer allows for the formation of multiple orthogonal condensates that can each be designed to capture a unique target. Centrifugation

of a high concentration of these nanostars can form macroscopic orthogonal liquid layers, similar to how solvents in a separatory funnel would form phases. The ability to form multiple liquid layers affords this technique a multiplexing feature, i.e., the separation of multiple targets can occur in a single binding step unlike traditional methods which would require serially performing multiple steps. To collect the targets, we draw from well-established DNA nanotechnology principles and release the target from the aptamer by performing the kleptamer reaction (Lloyd et al., 2018), which involves binding a complementary strand to the aptamer, causing it to unfold and release its analyte into the gas phase. Unlike traditional affinity chromatography, our proposed method does not require an expensive column support (see Chapter 5 for a discussion on the cost-effectiveness of this method), nor does it subject the target to potentially harsh conditions to strip it from said support.

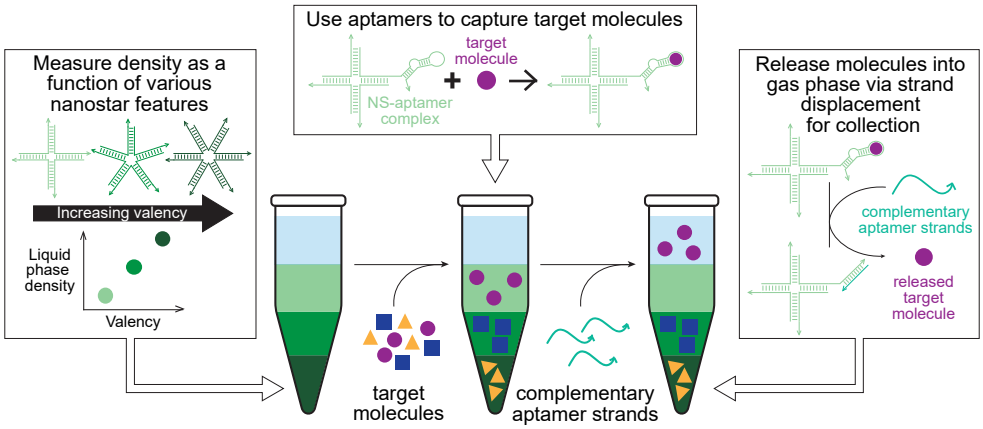

Figure 1.2: Our goal is to engineer macroscopic DNA liquids to act as compartments to capture and separate multiple target molecules. We study how nanostar features affect liquid phase density to control formation of macroscopic DNA liquid layers (left tube). With this understanding of how to form layers, we can modify nanostars with a binding moiety, like an aptamer, to localize various target molecules into unique compartments (center tube). To collect our targets, we can unfold aptamers by adding a strand complementary to it. The target molecule would then release into gas phase, where it can be collected for downstream use (right tube).

The chapters in this thesis discuss the work towards this overall goal. Chapter 2 focuses on a capillary-based method we developed for the measurement of liquid phase concentrations. Chapter 3 discusses the design principles we have discovered to form macroscopic DNA liquid layers. Chapter 4 demonstrates rudimentary experiments localizing various biomolecules in these liquid layers.

In Chapter 2, we describe a capillary-based method we developed to measure liquid phase concentrations. The order in which DNA liquids will layer in a microcen-

trifuge tube depends on their density, which is directly proportional to the liquid phase concentration. We therefore required a method by which we can measure that property and predict the layering order. We compare our method to current ones in the field and discuss its limitations, particularly how our method is not robust to noise from manufacturer replicates.

In Chapter 3, we present a set of design principles for engineering nanostars to create liquid layers in a microcentrifuge tube. Using the method described in Chapter 2, we show how various nanostar features, such as arm length, sticky end strength, and valency, affect liquid phase density, which determines the order of layering between orthogonal liquids. We further show that the interface quality between pairwise liquids is determined by a combination of the density differences between liquids and the orthogonality of sticky ends between nanostars, and we devise a metric to calculate this orthogonality. Using these design principles, we are currently able to create up to five orthogonal liquid layers in a tube.

Chapter 4 demonstrates rudimentary experiments involving the localization of various biomolecules. We demonstrate localization of oligos in a multilayer DNA liquid system by modifying nanostars with tag regions complementary to the target strand. We also demonstrate, in a separate system, localization of fluorescent streptavidin to a single DNA liquid layer by modifying nanostars with a streptaviding-binding aptamer (Bing et al., 2010). After localization of targets in each system, we added strands complementary to either the tag region or the aptamer. This caused targets to be displaced from their binding moiety and released into the gas phase.

1.6 A note on nanostar nomenclature

Over the course of my graduate school career, I have designed over one hundred nanostars. This large number of designs required that I devise a systematic way to name my nanostars so that I maintain some semblance of organization. The names of all nanostars used in this thesis are written as follows:

$$\alpha\text{-ns}\beta\text{-}\gamma\text{SE}\delta\text{-v}\varepsilon$$

where each Greek letter is a number that represents a particular feature of the nanostar. α denotes the valency, β denotes the arm length in basepairs, γ represents the length of the SE in nucleotides, δ is an identifier for a specific sticky end sequence (see Table 1.1), and ε denotes the nanostar version number. For example, the name 4-ns15-6SE34-v1 indicates that the nanostar has four arms, each with an arm length

of 15 bp, and that the SE is 6 nt in length and has the sequence 'GAGCTC' according to Table 1.1. A nanostar given the name 4-ns15-6SE34-v2 has the same features as 4-ns15-6SE34-v1, with the exception that the arm domain sequences are different between the two versions.

Sticky end	Sequence (5' to 3')	ΔG (kcal/mol)
SE17	ATTGCAA	-10.60
SE20	ATTCGAA	-10.26
SE21	ACTTAAG	-9.69
SE23	ACCTAGG	-11.30
SE24	AAACGTT	-10.41
SE25	ATCCGGA	-12.23
SE27	AGGATCC	-10.85
SE29	ACAATTG	-10.37
SE30	AGGTACC	-10.85
SE31	ACCATGG	-11.98
SE34	AGAGCTC	-11.21
SE35	AGGGCCC	-13.28
SE36	AGCTAGC	-11.39
SE42	AGTGCAC	-11.83
SE43	AAGGCCT	-11.92
SE44	AGACGTC	-11.56
SE45	AGTCGAC	-11.49
SE48	ACACGTG	-12.66
SE49	ACGATCG	-12.52
SE50	ATGATCA	-10.14
SE53	AACATGT	-10.25
SE54	AGGCGCC	-14.20
SE60	AAGCGCT	-12.85

Table 1.1: Sequences and free energy of sticky ends. All sticky ends are 6 nt palindromic sequences, with a free 'A' base on the 5' end. This free 'A' base was included in the calculation of the free energy. Free energies calculated using NUPACK3 model with the following parameters: 0.5 M NaCl, 20°C, which reflect the experimental conditions in this work. Free energies listed are the complex free energies.

Chapter 2

CAPILLARY-BASED METHOD FOR MEASURING LIQUID PHASE CONCENTRATION

Our goal is to form macroscopic DNA liquid layers, which will layer according to their densities. As we would like to be able to predict and control the order in which liquids will layer in a microcentrifuge tube, we required a method for measuring the liquid phase density.

The density of the liquid phase is directly proportional to its concentration via the following equation:

$$\rho_{\text{liq}} = C_{\text{liq}} + \rho_{\text{sol}} \left(1 - \frac{C_{\text{liq}}}{\rho_{\text{DNA}}}\right) \tag{2.1}$$

where C_{liq} is the concentration of DNA in the liquid phase and ρ_{liq}, ρ_{sol}, and ρ_{DNA} are the densities of the liquid phase, solvent, and DNA, respectively (see Appendix A for a derivation of this equation). C_{liq} is in units of mass concentration, i.e., mg/mL. As concentration is easily measurable via spectrophotometry, we were interested in measuring the concentration of liquid phases as a proxy for their densities.

2.1 Current measurement methods

In the 2013 Biffi *et al.* paper, phase diagrams of a four- and three-arm nanostar were constructed by centrifuging capillaries filled with nanostar solutions, cutting them open, and then measuring the absorbance of the liquid and gas phase via a spectrophotometer. Jeon *et al.* similarly measured the absorbance of DNA liquids, but instead of capillaries, they centrifuged solutions in microcentrifuge tubes and removed the gas phase via pipette before measurement (Jeon, D. T. Nguyen, Abraham, et al., 2018). Observation of the phase diagram from the Biffi *et al.* study and my own attempts of the method described in Jeon *et al.* show that direct measurement of the liquid phase concentration can result in large error bars (Fig 2.1a). DNA liquids can be very viscous, which makes them difficult to handle, and are highly concentrated, which could saturate the photodetectors in a spectrophotometer. These characteristics require dilution of the liquid phase prior to measurement. While this step is not explicitly written in either of the aforementioned studies, discussions with the first author of the Jeon *et al.* paper revealed this necessary step. We suspect that dilution of this viscous material

contributes to the large error bars. The need to remove the gas phase as described in Jeon *et al.* also contributes to errors in measurement, as incomplete removal would result in mixing of the liquid and gas phase, which would alter the overall concentration. In addition, removal of the gas phase can be difficult if the interface between the liquid and gas phases is not clearly defined.

A more efficient and high throughput method to measure liquid phase concentrations can be done via microfluidics. Conrad *et al.* and Hegde *et al.* constructed full phase diagrams in this manner by encapsulating various concentrations of nanostars in micron-sized water-in-oil emulsions (Nathaniel Conrad et al., 2022; Hegde et al., 2024). By measuring the volume fraction of the condensate droplet relative to the emulsion droplet as a function of nanostar concentration, one could then extract the dense and dilute phase concentrations according to the lever rule:

$$C_{\text{tot}} = C_{\text{liq}} f_{\text{liq}} + C_{\text{gas}} f_{\text{gas}} \tag{2.2}$$

where C_{tot}, C_{liq}, and C_{gas} are the total, liquid phase, and gas phase concentration, respectively. f_{liq} and f_{gas} are the liquid and gas phase volume fraction, respectively, and $f_{\text{liq}} + f_{\text{gas}} = 1$.

While this method is more efficient and less prone to error, it requires a complex microfluidics setup. The methods described in Biffi *et al.* and Jeon *et al.* are easier to implement, but as stated, requires direct handling of the liquid phase, which can lead to large error bars. We therefore aimed to develop a method that does not require direct handling of the liquid phase nor a complex setup.

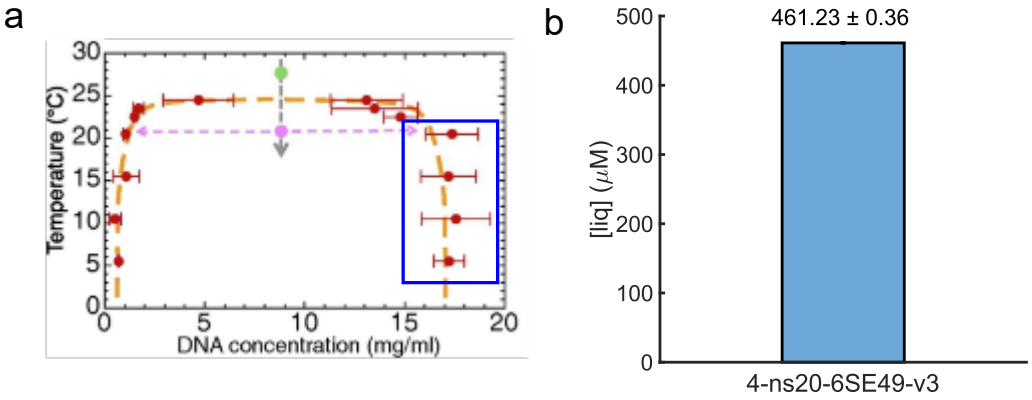

Figure 2.1: Our capillary method results in small error bars. (a) Adapted from Biffi *et al.* Phase diagram of a four-arm nanostar. As their method involves direct handling and measurement of the liquid phase, the error bars tend to be large (blue box). (b) Our measurement of the liquid phase concentration of the same nanostar results in smaller error bars when we use our capillary method.

2.2 Capillary method

We developed a capillary-based method that is easily implementable. It is similar to the one described in Biffi *et al*. We, however, report smaller error bars compared to the measurements in that study as our protocol does not require direct handling of the liquid phase (Fig 2.1b). Liquid phase concentration measurements were performed in the following manner.

Sample preparation

Nanostar strands were mixed and annealed at a concentration of 100 μM for each strand in 1xTE, pH 7.5 buffer with 0.5 M NaCl. This buffer and salt concentration were used in all liquid phase quantification experiments reported in this thesis. YOYO-1 intercalating dye (ex 491 nm / em 509 nm) was added at 1% of the total concentration of nanostars to allow for visualization of the liquid phase. Afterwards, thin capillaries were filled with the nanostar solution and sealed with UV gel nail polish before centrifugation.

Centrifugation

Capillaries were initially spun in an angled rotor at a speed of 40000 rcf followed by a spin in a swinging bucket rotor at 2000 rcf. The need for two spins is due to the speed limits of each rotor. The high speed of the angled rotor helps the liquid phase sediment quickly to the bottom of the capillary. However, because the rotor is angled, the interface of the liquid and gas phase would also be angled, which can affect volume fraction measurements. A spin in the swinging bucket rotor helps flatten the liquid phase. One could potentially do a single spin with the swinging bucket rotor; however, such rotors typically have very low spin speeds, which would require long spin times. The use of these two rotors helps ensure full sedimentation of liquid phase in a reasonable time.

The time and temperature at which capillaries should be spun in the angled rotor depends on the particular nanostar. Nanostars that form high viscosity liquids can stick to the sides of the capillary (see Fig 2.2b). Such samples typically require longer spin times and/or higher temperature spins to ensure that all liquid phase sediments to the bottom of the capillary (see Appendix B for a discussion on the effect of high temperature spins). Otherwise, the measured liquid phase volume fraction will be inaccurate. Fig 2.2c shows an example of how volume fraction measurements, and subsequently the calculated liquid phase concentrations, are impacted if not all of the liquid phase is spun down. In general, the measured liquid phase volume

fraction will be smaller than expected, which then artificially increases the liquid phase concentration calculated from the lever rule. Typically, nanostars with short arms, strong sticky ends, and/or high valency tend to form more viscous liquids.

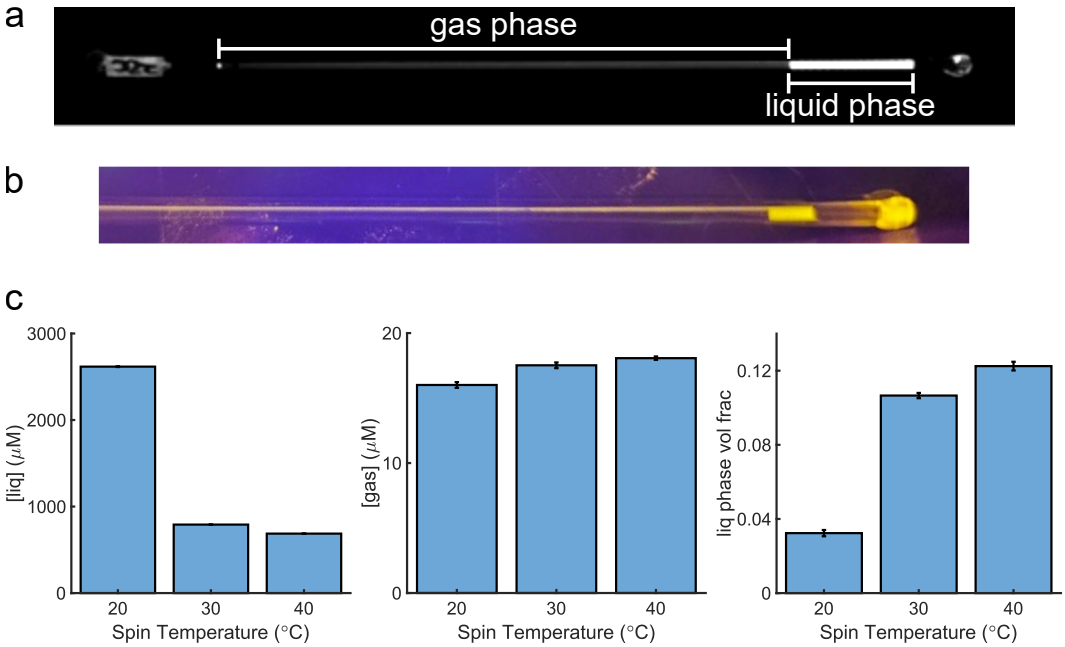

Figure 2.2: Viscous liquids require higher spin temperatures. (a) Image of a capillary taken on a gel scanner. Nanostar solution was dyed with YOYO-1 to allow for visualization. Liquid phase (white region) sediments to the bottom of the capillary after centrifugation. (b) Image of a capillary taken on a blue LED transilluminator. Liquid phase appears yellow under this lighting. This sample (4-ns15-6SE36-v2) was spun at 20°C; however, because the liquid phase was quite viscous, we observed that it sticks to the length of the capillary, resulting in a reduced amount of liquid phase at the bottom. (c) Measurements of liquid phase concentration (*left*), gas phase concentration (*middle*), and liquid phase volume fraction (*right*) of samples of 4-ns15-6SE36-v2 spun under different temperatures. At the typical 20°C spin, we observed that the volume fraction is very small because most of the liquid phase did not sediment to the bottom. As a result, the calculated liquid phase concentration at 20°C was artificially high. Increasing the spin temperature caused the liquid to become less viscous and to flow more, allowing it to sediment to the bottom and thereby increase the liquid phase volume fraction and obtain a more accurate calculation of the liquid phase concentration.

Sample measurement

After spinning, capillaries were imaged on a gel imager (Fig 2.2a). These images were processed via a Matlab script to calculate the liquid phase volume fraction. We then broke the capillaries open and collected the gas phase. The absorbance of gas phase solutions at 260 nm was measured on a Nanodrop spectrophotometer (ThermoFisher) and converted to molar concentrations. We use these two measured

properties (liquid phase volume fraction and gas phase concentration) to calculate the liquid phase concentration via the lever rule.

When converting from absorbance to molar concentrations via Beer's law, we used the extinction coefficient of a fully formed nanostar. The use of this particular extinction coefficient is technically not accurate. The gas phase is composed of a multitude of DNA species, such as uncondensed nanostars, single strands, and malformed nanostars (Biffi et al., 2013). There is no single extinction coefficient value that perfectly describes this solution. We therefore chose the extinction coefficient of a fully formed nanostar to try and account for any secondary structures that form and acknowledge that this choice could systematically change the true value of the measured gas phase concentration.

2.3 Benzamide contamination in standard desalted strands

Absorbance measurements of DNA solutions are useful in determining not just the concentration, but also the purity of the sample. The ideal DNA absorbance spectrum typically has a large peak at 260 nm, a 260/280 ratio of ~1.8, and a 260/230 ratio of ~2 (see Fig 2.3). The two ratios listed are used to determine the purity of DNA. The 260/280 ratio is used to determine protein contamination, which is not a concern for our oligonucleotides as they are synthetically made. The 260/230 ratio indicates the level of contamination from salts and organic compounds. Such contaminants present in the solution would increase the absorbance around 230 nm, thereby lowering the 260/230 ratio.

In our initial experiments where we used the method described in Jeon *et al.*, we measured the absorbance of both the liquid and gas phases of our samples (Fig 2.3a,b). The strands were ordered from IDT and were of standard desalted (STD) purification. We observed that while the spectra of the liquid phases are qualitatively similar to the ideal DNA absorbance spectrum, the spectra of the gas phases exhibit an abnormally high peak around 230 nm. We suspect that contaminants are what contribute to this peak. More specifically, we believe that benzamide, which is a protecting group byproduct in oligonucleotide synthesis, is the main contributor. Benzamide has an absorption maximum near 226 nm (see Fig 2.3d) (Addison et al., 2011), which aligns with what we see in our spectra. In fact, when we measured the absorbance of single nanostar strands, we note that the the 260/230 ratio is not at the ideal value of 2 (Fig 2.3c). We hypothesize that the high 230 nm peak observed in the absorbance spectra of the gas phase is due to condensed nanostars

"self-purifying" and ejecting the benzamide contaminants from the liquid phase, leading to an increased concentration of the compound in the gas phase.

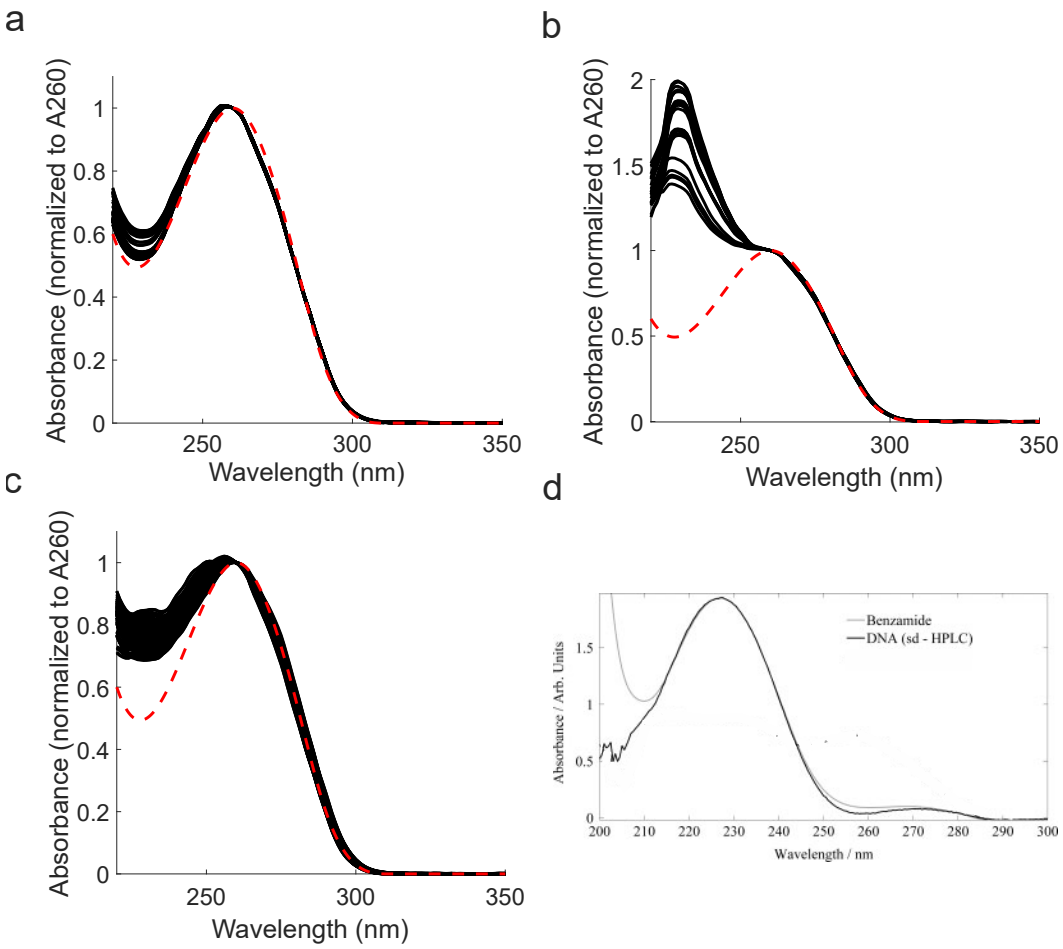

Figure 2.3: Absorbance spectra of STD strands reveal benzamide contamination. UV-Vis absorbance spectra of (a) liquid phase, (b) gas phase, and (c) single STD strands. Black lines are measured spectra of various samples normalized to the A260 value. The dotted red line in all three plots is a schematic of the ideal DNA absorbance curve. The spectra of liquid phase most closely align with the ideal absorbance curve, while the spectra of gas phase exhibit an abnormally high peak around 230 nm, which suggests the presence of benzamide. (d) Adapted from Addison et al., 2011. Absorbance spectrum of benzamide (light gray line) and spectrum difference between STD and HPLC DNA strands ordered from IDT (dark gray line). Benzamide has an absorption maximum around 226 nm, which aligns with the maximum observed in the DNA spectrum, indicating that benzamide is a prominent contaminant in STD strands. Benzamide also has a second absorption maximum near 268 nm, which could potentially interfere with proper quantification of DNA.

A 2011 study by Addison *et al.* suggests that benzamide potentially interferes with proper quantification of DNA strand concentrations. Benzamide has a second absorption maximum near 268 nm (see Fig 2.3d). As DNA is quantified using the absorbance value at 260 nm, it is possible that the presence of benzamide contributes

to the absorbance at 260 nm, leading to an overestimation of strand concentration. Interestingly, Addison *et al*. measured the absorbance of only polyA strands and found that quantification errors may be negligible in the presence of benzamide for such strands. This is due to an apparent redshift of the benzamide around 268 nm, leading to reduced overlap around 260 nm. However, they emphasize that their study was limited to polyA strands, and no other sequences of DNA were tested in this study. They also claim that beyond possible quantification errors, benzamide potentially forms hydrogen bonds with the bases of oligomers. The redshift observed suggests that electrons are redistributed to parts of the nucleotide that participate in hydrogen bonding. If true, the kinetics and thermodynamics of DNA binding could be affected.

In our experiments, we have also visibly observed contaminants in our tubes when we form macroscopic liquids (Fig 2.5c). IDT states that these visible precipitates are possibly trityl groups, which is another type of protecting group used in oligo synthesis, or controlled-pore glass, which is the material oligos are synthesized on[1]. However, benzamide also has low solubility in aqueous solutions (Ouyang et al., 2019). We therefore suspect that these visible precipitates also contain benzamide. In addition, we observe a fair amount of fluorescence in the gas phase, which suggests increased amounts of DNA in this region. If benzamide hydrogen bonds with nucleotide bases, the interactions between nanostars could be weakened due to competition with this contaminant and result in an increased amount of nanostars in the gas phase. The large peak at 230 nm observed in Fig 2.3b also gives us concern that proper quantification of gas phase concentrations may be affected.

Effect of benzamide on DNA quantification

To estimate how adversely benzamide could affect DNA quantification, we measured the absorbance spectra of a single ethanol precipitated strand (see next section on ethanol precipitation) mixed with various amounts of benzamide, as shown in Fig 2.4a. The dotted red line is the spectrum of pure single-stranded DNA. We observe that benzamide begins to affect the A260 value of DNA when its concentration is fifty times higher than that of DNA. We especially note how qualitatively similar the spectra of highly concentrated benzamide samples (100X; dark blue line) look to the gas phase absorbance spectra shown in Fig 2.3.

Fig 2.4b plots the A260 value from each spectrum shown in Fig 2.4a normalized to

[1] https://www.idtdna.com/pages/education/decoded/article/tips-for-resuspending-and-diluting-your-oligonucleotides

the A260 value of pure DNA (dotted red line) as a function of benzamide concentration. This normalized value quantifies how much benzamide causes overestimation of DNA concentrations. Depending on the amount of benzamide in the solution, one could overestimate the concentration by 10-20%.

We estimated that a tube of STD strands from IDT could have on the order of ~30 mM of benzamide (see Appendix C for this calculation). As gas phase concentrations range on the order of tens of micromolar, the concentration of benzamide in gas phase is potentially a hundred times more than the concentration of DNA. This falls within the regime of when benzamide can cause overestimation of DNA concentrations. In addition, we can extrapolate the error observed in Fig 2.4b to be the potential error measured in gas phase concentrations given how similar the spectra in Fig 2.4a and Fig 2.3b are. Assuming that gas phase concentrations are overestimated, but the volume fractions and total concentration are not affected by the presence of benzamide, we estimate that the liquid phase concentration can be underestimated by up to 26% depending on the error and absolute value of the gas phase concentration. See Appendix D for a discussion on the assumptions and calculations of this estimate.

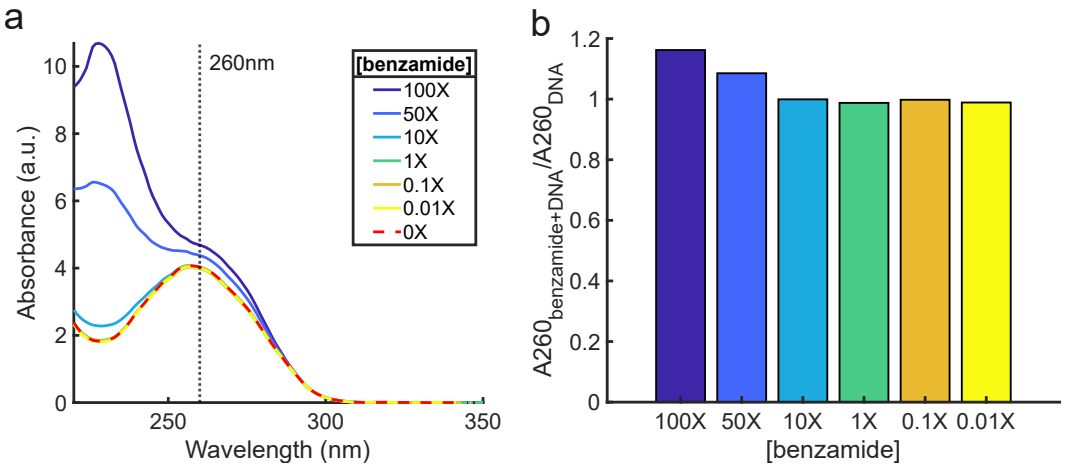

Figure 2.4: Effect of benzamide on DNA quantification. (a) Raw absorbance spectra of single-stranded EP DNA mixed with various concentrations of benzamide. The DNA concentration is at 1X, where 1X = 10 μM. The dotted red line is the spectrum of pure DNA, i.e. no benzamide addition. At a benzamide concentration of 50X, we observe that the A260 value increases, which indicates the potential to overestimate the DNA concentration when benzamide is present in solution. (b) We plot the A260 value of each spectra in (a) normalized to the A260 value of pure DNA (dotted red line) to quantify the error in DNA quantification when benzamide is present in solution. In this experiment, the error ranges from 10-15%. Observation of the gas phase absorbance spectra in Fig 2.5b indicates that the amount of benzamide present in gas phase can be more than 100X based on the A230/A260 ratio. We estimate that the error in a general experimental setting could then range from 10-20%.

Removal of benzamide via ethanol precipitation

Clearly, the removal of benzamide is necessary to improve not only the appearance of our macroscopic liquids but also the quantification of DNA. Ethanol precipitation is a cheap and simple method to remove such contaminants. This procedure involves adding salts and ethanol to DNA, which will precipitate out of solution. Since benzamide is more soluble in ethanol than in water (Ouyang et al., 2019), centrifugation and then removal of the supernatant should remove the benzamide contaminants. Ordering HPLC strands from IDT also removes any synthesis byproducts, but is significantly more expensive and results in less yield than performing ethanol precipitation in house.

Fig 2.5a compares the UV-vis absorbance spectra of STD strands from IDT with the spectra of the same STD strands after ethanol precipitation (hereafter known as EP strands). We observed that the absorbance of EP strands around 230 nm decreases and that the 260/230 ratio is closer to the ideal value of 2 for each strand, indicating successful removal of benzamide from the solution. We also measured the gas phase concentration of various nanostar solutions composed of these EP strands and observed a dramatic reduction in the absorbance values at around 230 nm compared to the same gas phase composed of STD strands (Fig 2.5b). In addition, when we use EP strands to form macroscopic liquid layers, we noticed an improvement in the appearance of the layers (see Section 3.2 for a discussion on layering quality) and a decreased amount of fluorescence in the gas phase (Fig 2.5d). We attribute these changes to improved interactions between nanostars due to the removal of the competing benzamide binding to bases.

2.4 Impact of benzamide on sample variability

In our attempts to understand the contamination in our DNA strands, we discovered an interesting aspect about sample variability with products from IDT. Before continuing with this discussion, we will first define some terminology. We define *technical* replicates as repeated measurements with the same stock of strands. We define *sample* replicates as measurements of different synthesis batches of the same sequence, i.e., we order the same sequences from IDT on different dates[2]. Ideally and theoretically, such sample replicates should produce the same result (assuming technical replicates are reproducible) as these strands are synthetically made.

[2]In the life sciences, these terms are usually called *technical* and *biological* replicates. The use of the word *biological*, however, may be confusing as it usually refers to cell samples. We therefore opted for *sample* replicates.

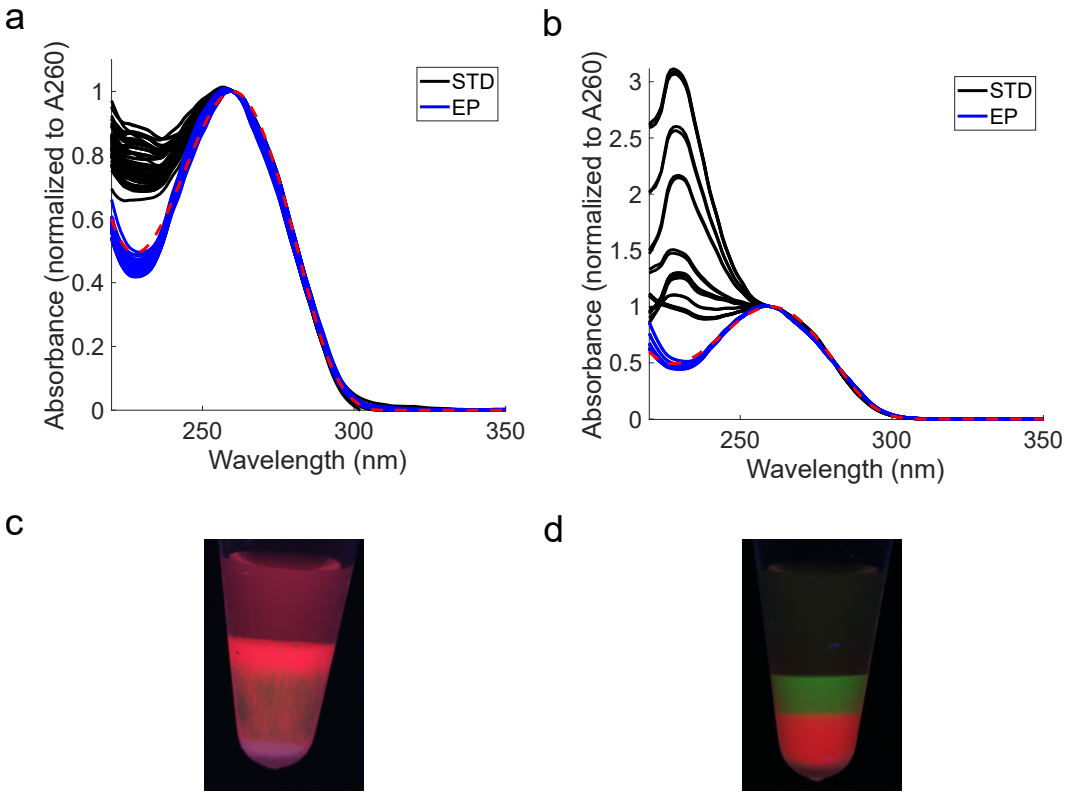

Figure 2.5: Comparison of STD and EP strands. UV-Vis absorbance spectra of various samples of (a) single strands and (b) gas phase samples. Black and blue lines are measured spectra normalized to the A260 value. The dotted red line in both plots is a schematic of the ideal DNA absorbance curve. In both plots, the spectra of EP strands (blue lines) are more closely aligned with the ideal absorbance curve than the spectra of STD strands (black lines). (c) Image of two liquids (dyed red and green) composed of STD strands. Contaminants are clearly visible at the bottom of the tube as white precipitants. (d) Image of the same two liquids composed of EP strands. The quality of layering has drastically improved compared to (c) and no precipitants are visible in the tube. Liquids were dyed with UV-excitable dyes and imaged on a UV transilluminator.

To see if our technical replicates are reproducible, we measured the liquid phase concentration of the same stock of STD strands on different days via the capillary method. Fig 2.6a shows the liquid phase concentration, gas phase concentration, and liquid phase volume fraction of the same sample measured on different dates. Across all three of these properties, the variability in these values is less than 5% from each other, indicating that the capillary method is a precise one when measuring the same sample multiple times.

When testing to see if this method is robust to sample replicates, we observed a completely different result. Fig 2.6b shows the measured properties of three different nanostars, each of which was ordered from IDT on three separate dates.

The three nanostars have equal valency and identical SE sequences, but varied in arm length. Unlike the technical replicates, the measured properties of the sample replicates can vary up to 50% from each other. The most disturbing result is that one of the nanostars (4-ns21-6SE36-v2; ordered on 240813) did not show visible phase separation in the capillary, even though the other two samples of the same nanostar sequence did (Fig 2.6c). Interestingly, despite the observed variability of measurements between identical nanostars ordered on different dates, the measured properties of nanostars ordered on the same date were always systematically higher or lower than those of all other dates across all arm lengths.

We suspect that this variability is again due to benzamide and other contaminants leftover from oligo synthesis. The amount of contaminants in each sample most likely varies depending on the day of manufacturing. Indeed, when we observed the absorbance spectra of the gas phases, we note that samples ordered on the same date have qualitatively similar spectra (Fig 2.6d). This potentially explains why samples from the same order date are always systematically more or less than samples of other order dates. In other words, strands synthesized on the same day have the same amount of contaminants. As the amount of contaminants varies by day, that could result in the variability we observe in our measurements across sample replicates.

These discrepancies across sample replicates is concerning. They suggest that not only the measured concentrations of the liquid phase can change depending on when they are synthesized, but also their behavior relative to layering, as these measured values are a predictor for layering order. To determine if contaminants are the cause of these discrepancies, we ethanol precipitated the strands to remove them. Fig 2.7a shows the measured properties of the same nanostars after ethanol precipitation. We were unable to ethanol precipitate samples ordered on 240425 because there was not enough material to do so. We observed that the difference in liquid phase concentrations across sample replicates for two of the nanostars has been reduced to almost zero. The most surprising result is that the sample that previously did not show visible phase separation now does (Fig 2.7b), and we were able to measure the properties of that sample. We suspect that nanostar interactions were so severely weakened due to adverse binding with benzamide that nanostars pre-precipitation were not able to phase separate properly. Despite this improvement, we still observe a difference in liquid phase concentration between sample replicates for that particular nanostar.

While ethanol precipitation seemingly reduced variability in our measurements of

the liquid phase concentration, we still observed discrepancies across sample replicates in the gas phase concentrations and liquid phase volume fractions, which are the properties we directly measure. In comparing the measurements between STD and EP strands, we noticed aspects that nevertheless suggest an overall improvement nanostar interactions after precipitation. The difference in volume fraction between sample replicates does not change after precipitation; however, the absolute value does increase for both samples. We also note that not only does the absolute value of gas phase concentration decreases for both samples after precipitation, but the *difference* between the samples also decreases. Taken together, these facts suggest more nanostars have condensed into the liquid phase after ethanol precipitation. This increase in condensed nanostars is possibly due to stronger binding between the sticky ends, which previously may have been weakened by benzamide competing to bind to the bases before precipitation.

The difference in gas phase concentrations and volume fractions across sample replicates even after ethanol precipitation of strands suggests that other factors are still potentially affecting the reproducibility of our measurements. We hypothesized that perhaps truncated strands and possibly other contaminants that are not removed via precipitation could be contributing factors. We therefore ordered HPLC purified strands of the same nanostars from IDT and measured two sample replicates for each nanostar. We believed that HPLC purified strands should remove all contaminants and some amount of truncations, but not all. Fig 2.7c shows the measured properties of these samples. While there is a dramatic decrease in sample variability in the liquid phase concentration and volume fraction measurements, the gas phase concentration measurements still show some moderate differences between samples. Interestingly, the absolute values of the gas phase concentrations for HPLC strands is significantly lower than those of either STD or EP strands. We hypothesize that these low concentration values are a result of the HPLC purification process removing more contaminants and truncated strands than the ethanol precipitation procedure does. Not all impurities are removed, however, since we still observe discrepancies between sample replicates.

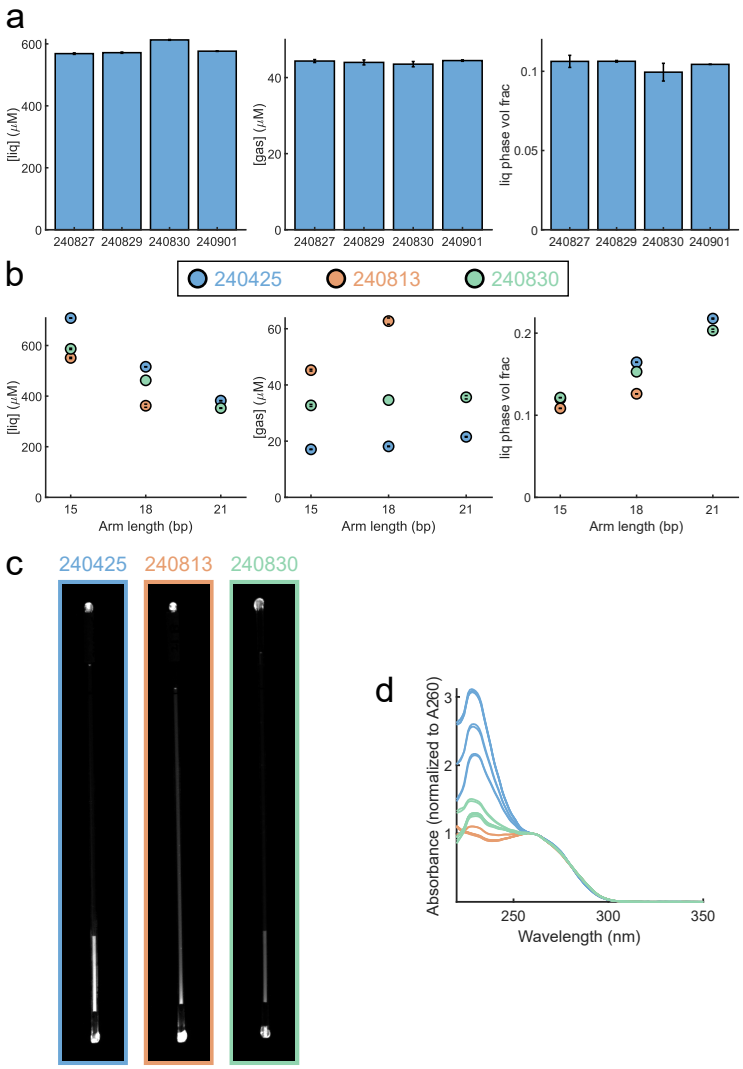

Figure 2.6: Benzamide contamination potentially causes sample variability. Measurements of the liquid phase concentration (*left*), gas phase concentration (*center*), and liquid phase volume fraction (*right*) of (a) technical replicates and (b) sample replicates. (a) Measurements were performed on four different dates, which are written in YYMMDD format on the x-axis. Across all four dates, measurements varied less than 5% from each other, indicating reproducibility of the capillary method. (b) Three nanostars (4-ns15-6SE36-v2, 4-ns18-6SE36-v2, 4-ns21-6SE36-v2) of equal valency and identical SE, but with various arm lengths, were each ordered on three different dates from IDT. Order dates, written in YYMMDD format, were 240425 (blue circles), 240813 (orange circles), and 240830 (green circles). Measurements varied up to 50% across sample replicates. The size of data points are larger than plotted error bars. No measurements were taken of the 240813 sample of 4-ns21-6SE36-v2 because we did not observe visible phase separation of that sample. (c) Images of capillaries containing solutions of sample replicates of 4-ns21-6SE36-v2. The sample ordered on 240813 (orange outline) did not have visible phase separation compared to the other sample replicates. (d) Absorbance spectra of the gas phase of sample replicates. Samples that were ordered on the same date had qualitatively similar spectra, indicating that the amount of contaminants varied based on the manufacturing date.

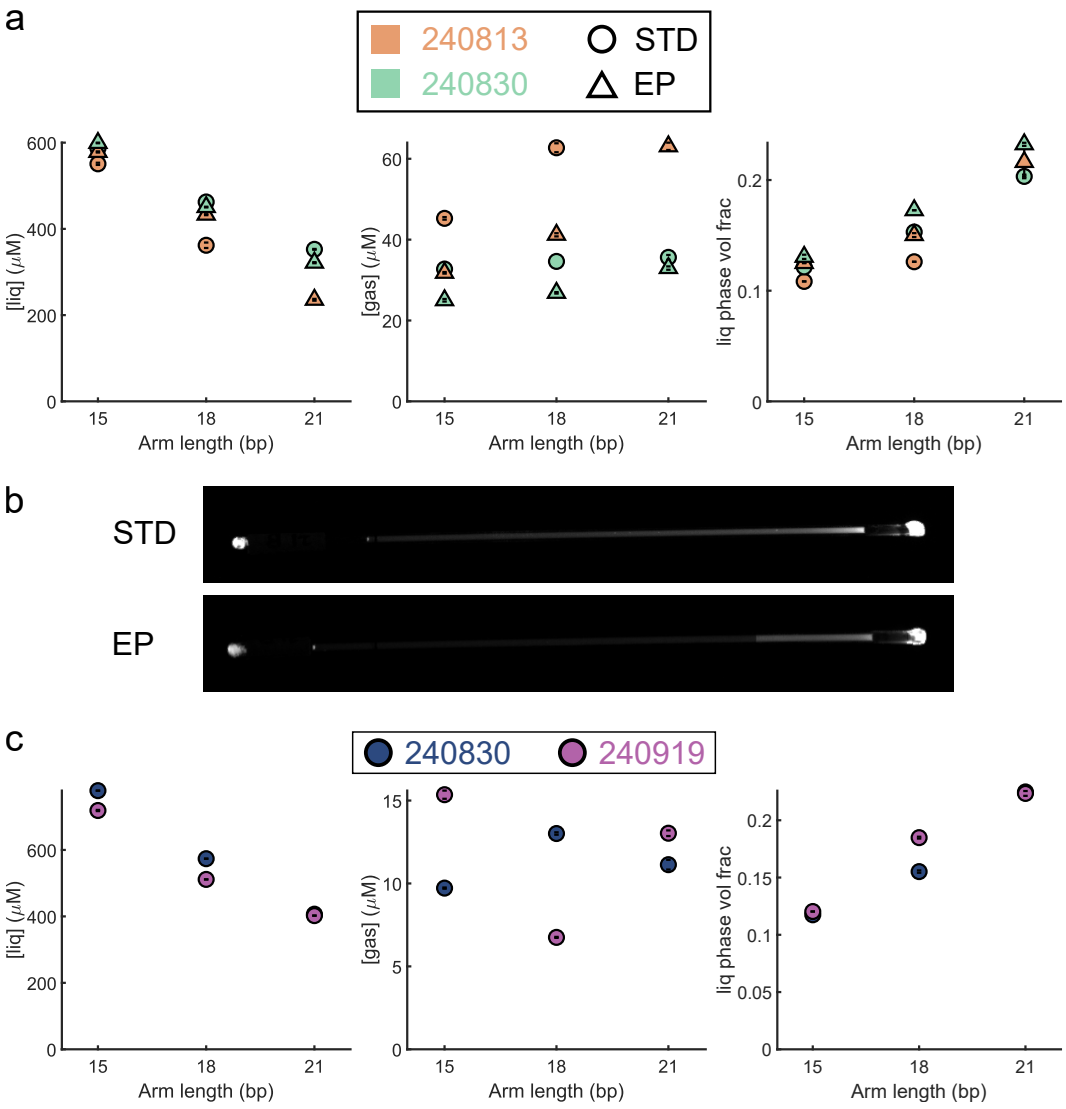

Figure 2.7: Ethanol precipitation and HPLC purification helps reduce some variability. Measurements of the liquid phase concentration (*left*), gas phase concentration (*center*), and liquid phase volume fraction (*right*) of (a) EP strands and (c) HPLC strands. The size of data points are larger than plotted error bars. (a) Only samples ordered on 240813 and 240830 were ethanol precipitated. Measurements of EP samples (triangles) had smaller differences between sample replicates than STD samples (circles). (b) Images of capillaries containing solutions of 4-ns21-6SE36-v2 ordered on 240813. After strands were ethanol precipitated, we observed clear phase separation. (c) Two samples of HPLC strands were ordered on 240830 and 240919. Measurements of gas phase concentration still show moderate differences between samples.

2.5 Gas phase concentration measurements are a limitation of capillary method

In observing the distribution of gas phase concentrations and volume fractions of sample replicates across all three purification types (STD, EP, and HPLC), we noticed that measurements of the gas phase concentration had a wider distribution of values than measurements of the volume fraction. We hypothesize that our direct measurement of the gas phase is the biggest contributor to the variability we observe in our liquid phase concentration calculations. Indeed, any impurities would reside in the gas phase and be reflected more in the measurements of this property than in measurements of volume fraction. We could potentially avoid measuring the gas phase concentration by instead measuring the volume fraction of samples at different total concentration of nanostars. This would be similar to the microfluidic methods described in Hegde *et al*. and Conrad *et al*., except with the use of capillaries. The drawback to such a method with capillaries would be the significant amount of materials and time required.

Our capillary-based method is certainly not the most accurate or efficient one for measuring liquid phase concentrations[3], but this protocol has revealed interesting details about the byproducts of oligonucleotide synthesis and how they could affect experiments. These results encouraged us to ethanol precipitate all STD strands ordered from IDT (see Appendix E for a comparison of IDT with ThermoFisher strands), as the high cost and low yield of HPLC strands made it financially impractical to use them in our experiments. All experiments reported in this thesis were done with EP strands unless otherwise noted. In addition, we ensured that the same synthesis batch of strands used to create a macroscopic liquid were also used to measure the corresponding liquid phase concentration. This is so that the order of the liquid relative to layering aligns with the measured concentration as a predictor.

[3] In fact, I think the most precise and accurate methods come from the work of Thomas Reese, a graduate student in Deborah Fygenson's group at UCSB.

Chapter 3

DESIGN PRINCIPLES OF IMMISCIBLE DNA LIQUID LAYERS

Formation of multilayer DNA liquids depends on two properties: layering order and layering quality. Layering order refers to the order in which liquids will layer according to their densities in a tube. Layering quality refers to the interfacial definition between two liquids. In this chapter, we explore how various design features affect these two properties.

Layering order is determined by the density of the liquids, which in turn is determined by nanostar features such as arm length, sticky end strength, and valency. Understanding the relationship between density and nanostar features would allow us to control the layering order of liquids by simply tuning these various features.

Through our explorations, we discovered that the layering quality of liquids is dependent on a combination of the density differences between liquids and the orthogonality of sticky ends between nanostars. High layering quality is important to achieve distinct layers in a tube. Qualitatively, we define optimal layering quality as the ability to draw a line along the interface of two liquids, and each liquid lies entirely above or below the line (see Fig 3.4). We quantitatively defined a metric for layering quality in Section 3.2.

Using the design principles we developed for these two properties (layering order and quality), we are able to create up to five liquid layers in a tube. We could potentially achieve more layers by refining experimental conditions and designing liquids to have smaller density differences while maintaining sticky end orthogonality.

3.1 Protocol for forming multilayer DNA liquids

Before we discuss design principles, let us first describe our protocol for forming multilayer DNA liquids. We mixed all nanostar strands into a single microcentrifuge tube. For each nanostar, a fluorescently labeled strand was substituted for 2% of that strand's non-fluorescent concentration. All fluorescent strands were UV-excitable and can be excited by the same wavelength on a UV transilluminator. We then followed a two-step protocol that first involved annealing nanostars at an optimal rate and then centrifuging tubes.

Annealing

Fig 3.2 shows images of three pairs of liquids annealed at different rates. Samples in the top and middle row were annealed at a rate of 0.1°C/min and 0.5°C/min, respectively. Samples were not annealed in the bottom row. Each pair of liquids has varying arm length difference between the nanostars they are composed of. The red liquid is composed of a 20 bp arm length nanostar (4-ns20-6SE23-v1) across all three tubes, while the nanostars that form the green liquids vary in arm length (15, 17, and 19bp) but have equal valency (four arms) and identical sticky end sequence (SE34).

Across all three pairs, we observe that slower annealing rates (0.1°C/min) resulted in layered liquids with clearly defined interfaces. However, when the annealing rate is increased to 0.5°C/min, we observe differences in the layering quality (see Section 3.2 for a definition of layering quality). The pair with the largest arm length difference (Δ5bp) had the most defined interface at this annealing rate, while other samples had a more gradient-like one. We suspect that as the arm length of green liquid nanostar increases, the transition temperature (the temperature at which liquid droplets begins to form) of the green liquid approaches that of the red (see Appendix F). Slower annealing rates not only allow for proper formation of the nanostar structure, but also allow for one liquid to condense before the next liquid begins to sediment out.

We suspect that the transition temperature difference between nanostars in the Δ1bp and Δ3bp is smaller compared to that of the Δ5bp sample. At the suboptimal annealing rate of 0.5°C/min, the time between liquid formation of each nanostar in the Δ1bp and Δ3bp samples is small, resulting in possible entanglement of the two liquids. The Δ5bp sample has a larger difference in transition temperatures, which potentially allows the green liquid to condense completely before the red one begins to nucleate (see Fig 3.1). At the optimal annealing rate of 0.1°C/min, these transition temperature differences do not play a significant role as the time between nucleation of liquids is long enough such that unlike nanostars do not interact. All liquid layers presented in this work were annealed at a rate of 0.1°C/min unless otherwise noted.

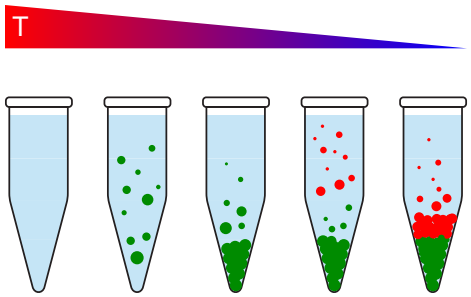

Figure 3.1: Schematic of layer formation during annealing. At high temperatures, nanostars do not interact and no liquids form. As the temperature decreases, the liquid with the higher transition temperature will begin to nucleate first (green liquid in this schematic). The droplets will begin to phase separate and sediment to the bottom of the tube. When the temperature cools to the transition temperature of the red liquid, it will also begin to separate out of solution and sediment on top of the green liquid. Slow annealing rates allow for a long enough buffer time between the transition temperatures of the two liquids to avoid mixing of the two liquids.

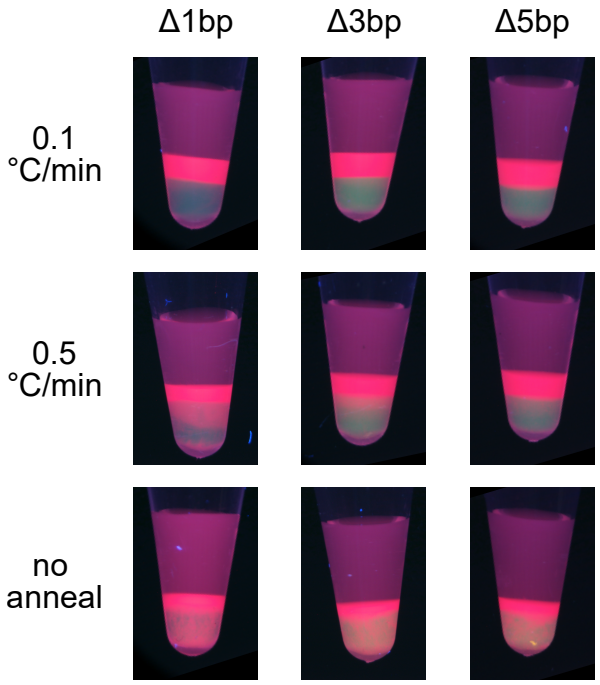

Figure 3.2: Images of pairwise liquids annealed at various rates. Nanostars have an arm length difference of 1 bp (left column), 3 bp (middle column), and 5 bp (right column). The red liquid nanostar in every image is 4-ns20-6SE23-v1. The green liquid nanostar of each column is 4-ns19-6SE34-v1, 4-ns17-6SE34-v1, and 4-ns15-6SE34-v1 from left to right. Each sample was annealed at a rate of 0.1°C/min (top row) and 0.5°C/min (middle row). Samples in the bottom row were not annealed. Slower annealing rates allow for one liquid to condense completely before the other, which usually results in well-defined interfaces between liquids. Strands were STD. All tubes were annealed and then centrifuged before imaging.

Centrifugation

Fig 3.3a shows an image of a pair of liquids after annealing at a rate of 0.1°C/min but before centrifugation. Annealing at a slow rate allows for a majority of like droplets to coalesce; however, we observe that some green droplets seem to be "stuck" in the red liquid. This is most likely a stochastic occurrence where not all of the green liquid coalesced together before the red one started to condense. Centrifugation is required to allow liquids to coalesce completely and form clearly defined layers. Fig 3.3b is an image of the same tube after centrifugation in a 90° rotor. We observe complete coalescence of both liquids and more defined interfaces. We used a 90° rotor so that the centrifugal force is perpendicular to the interface of liquids and prevents an angled appearance. All liquid layers presented in this work were centrifuged with a 90° rotor after annealing.

Centrifugation is also required to ensure that liquids layer according to their densities and not their transition temperatures. These two properties do not necessarily correlate, and one can have instances where the order of layers flip after centrifugation. Fig 3.3c and d demonstrates such an example. Before centrifugation, the red liquid layers on top of the green, suggesting that the transition temperature of the green liquid is greater than that of the red. After centrifugation, the red sediments to the bottom, indicating that the density of the red liquid is greater than that of the green. It should be noted that we observe some red "splotches" throughout the green liquid prior to centrifugation. We suspect that given enough time, gravity would pull the red liquid down to the bottom of the tube; however, centrifugation helps hasten the system to its equilibrium state.

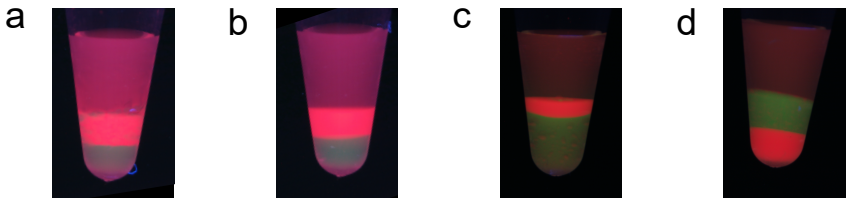

Figure 3.3: Comparison of layers pre- and post-centrifugation. (a, b) Images of the pairwise layering of 4-ns20-6SE23-v1 (red liquid) and 4-ns15-6SE34-v1 (green liquid) (a) before and (b) after centrifugation. Centrifugation helps liquids to coalesce completely. Strands were STD. (c, d) Images of 4-ns15-6SE21-v2 (red liquid) and 4-ns21-6SE44-v2 (green liquid) (c) before and (d) after centrifugation. Before centrifugation, liquids were layered according to their transition temperatures. After centrifugation, they layered according to their densities.

3.2 Defining layering quality

So far, we have loosely defined layering quality as the distinction of the interface between two liquids. Qualitatively, we define optimal layering quality as the ability to draw a line along the interface of two liquids, and each liquid lies entirely above or below the line. Note that we define the layering of liquids as a subset of the separation of liquids. Fig 3.4 demonstrates a schematic example. Separation can result in multiple distinct domains and nonlinear interfaces between two orthogonal liquids. Layering is the separation of two liquids into only two domains with a single interface between them, and each liquid lies entirely on one side or the other of the interface.

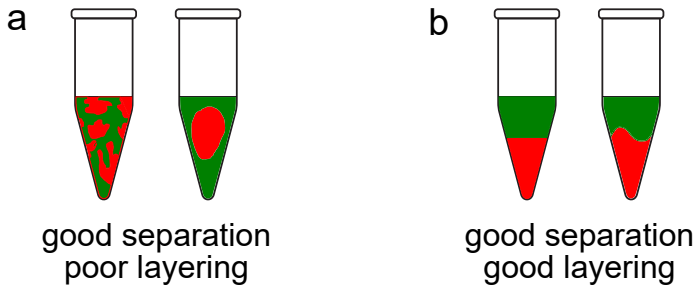

Figure 3.4: Separation versus layering. (a) The immiscibility of two orthogonal liquids can result in good separation, where there can be multiple domains or a nonlinear interface between the two liquids. (b) Layering is a subset of separation, where there is only a single interface between liquids, and each liquid lies entirely on one side or the other of the interface.

As observed in Fig 3.2, the appearance of liquid layers can range dramatically. While it is easy to determine "good" versus "bad" layer quality in certain cases (e.g. compare samples annealed at 0.1°C/min with those that were not annealed), it can be difficult in others, especially when the interface between layers is blurry and gradient-like (e.g. compare Δ1bp and Δ3bp samples annealed at 0.5°C/min). To help us compare the layering quality between pairs of liquids, we defined a quantitative layering metric (LQ) .

Fig 3.5 demonstrates how we calculate LQ. Since each liquid is labeled with a different fluorophore, we image tubes on a gel scanner to obtain a two-channel image. For each channel, we draw a rectangle over the tube and average across the width to obtain an intensity profile over the length of the rectangle. We draw the rectangle so that its length is perpendicular to the interface of the two liquids to ensure that we average along it. If an interface is not distinguishable, we draw the rectangle so that its length is perpendicular to the interface between the dense and

dilute phase. After normalization, we then calculate LQ as the area of intersection of the two line profiles divided by the total area of both profiles. The range of LQ is between 0 and 1, with 0 representing complete separation of the two liquids and 1 representing complete mixing.

In this thesis, we generally described liquids with an LQ $\leq$ 0.3 as having good layer formation. The LQ metric is not a definitive one and only provides an estimation of the layering quality. For example, pairwise liquids that have defined, but nonlinear interfaces (Fig 3.12) tend to result in LQ > 0.3 because of the metric's dependence on linear interfaces. Determining if liquids layered well or not is subjective to the viewer and the application of the liquids, and one could change this threshold value of 0.3 to fit their definition of optimal layering.

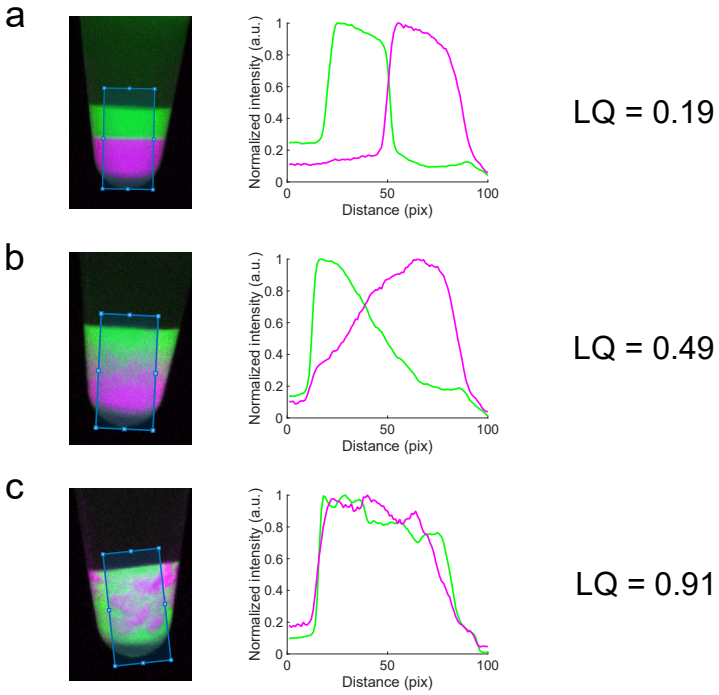

Figure 3.5: Calculation of LQ. LQ is our quantitative measure of the layering quality of pairwise liquids. We show three examples of how LQ is calculated for different layering qualities. A rectangle is drawn over liquids such that its length is perpendicular to the interface. If an interface is not distinguishable, the rectangle is drawn perpendicular to the dense/dilute interface. We average across the width of the rectangle to obtain a line profile for each channel, which is plotted to the right of each image. Fluorescence of each channel is normalized to the maximum intensity. LQ is calculated as the area of intersection of the two profiles divided by the total area of both profiles. The LQ value for each image is written to the right of the corresponding line profiles. Samples that have better layering quality have a lower LQ.

3.3 Effect of nanostar features on dense phase concentration

The material properties of a condensate depend on the structure of the monomer it is composed of. In terms of geometric nanostar features, we were most interested in understanding how changes in arm length, sticky end strength, and valency, i.e., the number of arms, affect liquid density.

There are many other geometric varieties that one can explore, such as the number of free bases in the junction, the presence of a free base between the arm domain and the sticky end, the presence of a blunt arm, i.e., an arm with no sticky end, or even anisotropic arm lengths. The design space of all possible nanostar geometries is vast. We therefore opted to explore a small subset of features that would still result in a rich variety of nanostar geometries.

Previous studies on the effect of nanostar features on density of liquids are quite limited in scope. Conrad *et al*. and Biffi *et al*. both measured phase diagrams for various nanostar valencies and showed that the concentration of liquid phase increases with increasing valency (Biffi et al., 2013; Nathaniel Conrad et al., 2022). However, there are no systematic studies on how arm length, sticky end strength, and valency affect liquid phase density. Past studies involving arm length and sticky end strength focus on their influence on phase transition temperatures (Sato, Sakamto, and Takinoue, 2020) and the growth rate of droplets (Agarwal, Osmanovic, Klocke, et al., 2022), but no direct measurement of how these features affect density.

We set out to fill in this knowledge gap in the literature by designing nanostars where we systematically varied each of these three features while keeping the other two constant. Fig 3.6 shows the liquid phase concentration as a function of changes in each nanostar feature. We plot the concentration in units of molarity (Fig 3.6a,b,c) and mass concentration (Fig 3.6d,e,f). In our explorations, we found it important to report concentration in both of these units. Mass concentration can be directly translated to density via equation 2.1. Molarity units inform us of the number of monomers in liquid phase as well as the binding capacity of liquids when nanostars are modified with aptamers. We note that the trend is opposite when comparing the two concentration graphs where valency is varied. In units of molarity, the concentration decreases (Fig 3.6c). Nanostar size increases with increasing valency, which results in larger volumes of liquid phase, as evidenced by Fig 3.6g. As molarity units do not consider nanostar sizes, concentration appears to decrease with increasing valency due to the increase in volume of liquid phase. The conversion to mass concentration takes into account the size of the nanostar and therefore results

in the increasing trend observed in Fig 3.6f, which aligns with results from previous studies (Biffi et al., 2013; Nathaniel Conrad et al., 2022).

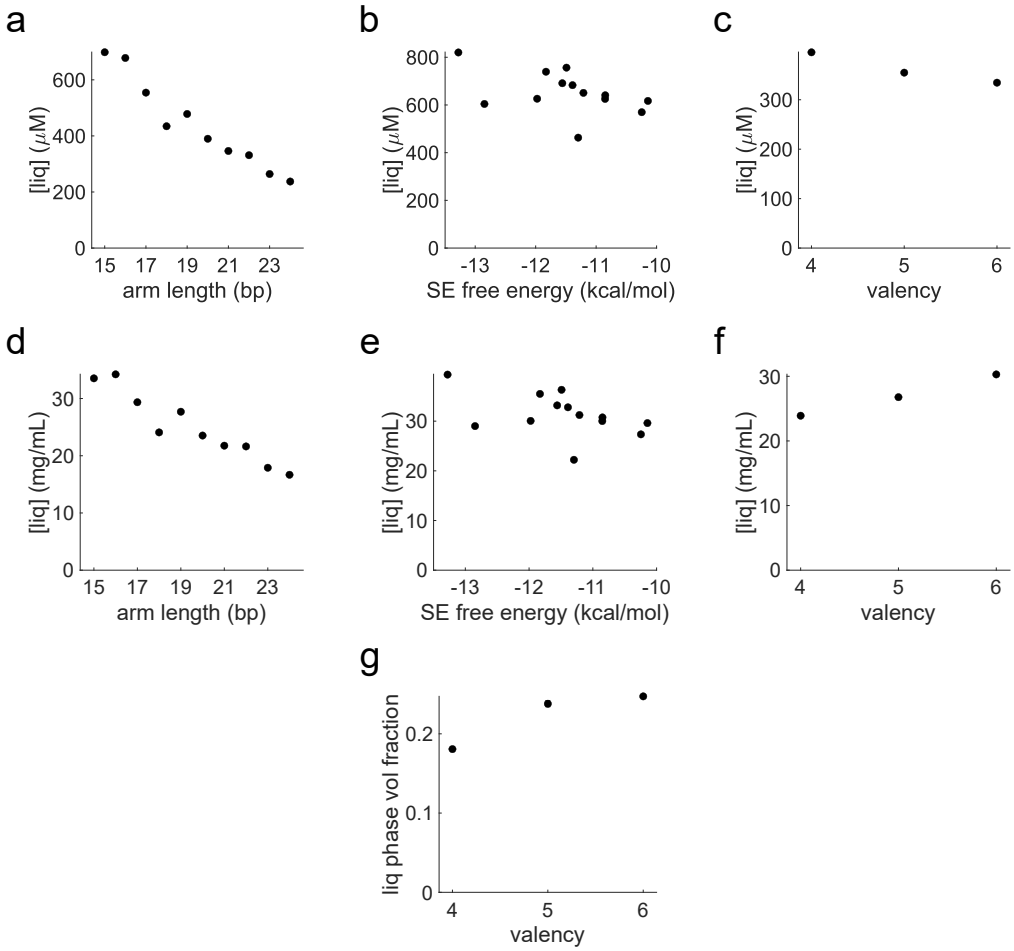

Figure 3.6: Effect of nanostar features on liquid phase concentration. Liquid phase concentration as a function of arm length (a,d), sticky end strength (b,e), and valency (c,f). a, b, and c are plotted in units of molarity. d, e, and f are plotted in units of mg/mL. Free energies in b and e were calculated via NUPACK. The general trend we observe in units of mass concentration is that a decrease in arm length, increase in sticky end strength, and/or increase in valency contribute towards increasing the liquid phase concentration. Units of mass concentration takes into account the size of nanostars, which is why we see opposing trends between c and f. (g) Volume fraction of liquid phase as a function of valency shows that increasing valency increases the volume fraction. Data plotted in a and d was measured using STD strands.

The general trend we observe in units of mass concentration is that a decrease in arm length, increase in sticky end strength, and/or increase in valency contribute towards increasing the liquid phase concentration, and by extension, the liquid phase density. Increasing the sticky end strength results in stronger hybridization between nanostars, while increasing valency increases the maximum number of interactions.

Increases in either or both of these features lead to more complete condensation of nanostars with fewer monomers remaining in the gas phase. Decreasing arm length decreases the effective volume of a single nanostar and thereby decreases the liquid phase volume fraction. According to the lever rule, a decrease in volume fraction results in an increase in liquid phase concentration.

We remark that the trend described for varying sticky end strength is not as strong compared to the one observed when varying arm length. Sticky end strength can be impacted by stoichiometry and synthesis errors. For example, as strands are STD, truncations would occur on the 5' end, which would result in longer 3' sticky ends than intended. In addition, previous studies have suggested that accurate calculation of free energies for oligos less than 15 bp in length is difficult to obtain (Huguet et al., 2010). The theoretical free energies as calculated by the nearest-neighbor model are probably affected by a combination of these factors and therefore provide only a coarse ordering of sticky end strengths. A more reliable method of determining the effective sticky end strengths would be to experimentally measure their melting temperatures. We also consider the possibility that the observed weak trend may be a result of the liquid phase concentration approaching a saturation regime when sticky end free energies are strong. See Appendix G for further disucssion on this topic.

With this knowledge of the relationship between density and nanostar features, we can tune any one of these three features to modulate the density of the liquid. In Fig 3.7, we demonstrate a reordering of two DNA liquids by simply changing the arm length of one of the nanostars. Initially, both nanostars have identical valencies (four arms), arm lengths (15 bp), and similar sticky end strengths ($\Delta\Delta G$ = 0.11 kcal/mol). As we increase the arm length of the green liquid nanostar, we observe the liquids mix when the arm length is equal to 18 bp. This suggests that at this particular arm length, the density of the green liquid approximately equals to that of the red. Increasing the arm length to 19 bp results in the green liquid layering on top. The density of the green liquid is now less than that of the red and causes the layers to reorder. Programmable control of the order of layers can be achieved in this way.

We note that the initial ordering of layers does not follow our expectation. The nearest-neighbor model predicts SE23 (the sticky end of the red liquid nanostar) to have a free energy of -11.30 kcal/mol, while SE34 (the sticky end of all green liquid nanostars) is predicted to have a free energy of -11.21 kcal/mol. Given that the arm lengths and valency of these two nanostars are equal, we expected the nanostar with

the more negative sticky end free energy (SE23) to form the denser liquid and be layered at the bottom. We clearly observed that the opposite happened. Given the reasons explained above about the accuracy of theoretical sticky end free energies, we suspect that the effective free energy of SE23 is more positive than that of SE34.

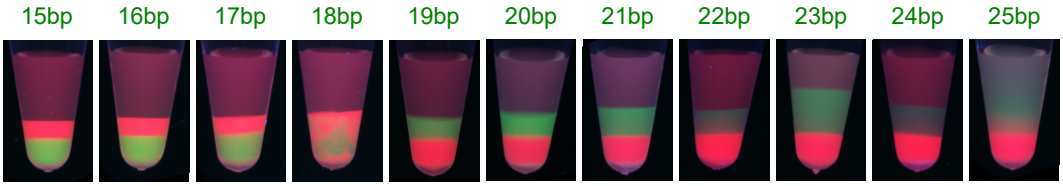

Figure 3.7: We can reorder layers by changing arm lengths. The red liquid nanostar in all images is 4-ns15-6SE23-v1. The green liquid nanostar in all images has four arms and has sticky end sequence SE34. The arm lengths vary from 15 bp to 25 bp, as written above each image. When the arm length of the green liquid nanostar equals 18 bp, the red and green liquid mix, suggesting they are of equal density. At 19 bp, the green liquid becomes less dense than the red and layers on top. At an arm length of 25 bp for this particular sticky end sequence and valency, the nanostar phase separates poorly under the specific experimental conditions. Strands are STD.

3.4 Layering quality depends on density differences and sticky end orthogonality

In our initial attempts to form DNA liquid layers, we were interested in determining the minimum density difference between liquids to achieve well-defined layers. We attempted to control density differences between liquids by varying nanostar features according to the trends found in Section 3.3. For example, given two nanostars that have equal valency and arm lengths, we were curious to know what is the minimum sticky end free energy difference ($\Delta\Delta G$) needed between the two monomers to achieve well-defined layers. We expected that layering quality would improve as $\Delta\Delta G$ increases, since the density difference between the two liquids should increase with increasing $\Delta\Delta G$. To test this idea, we pairwise layered 4-ns20-6SE34-v1 (dyed red in Fig 3.8 in all images except for the leftmost one, where it is dyed green), with five other nanostars that have the same arm length (20 bp) and valency (four-arms), but varying sticky end strengths. The sticky end identities of these five nanostars are listed in Table 3.1, where we also list the free energy of SE34 interacting with them.

We considered sticky ends to be orthogonal if they have little to no interactions between them, i.e., the free energy of two unlike sticky ends binding is more positive than when each of the sticky ends binds to themselves. Orthogonal sticky ends minimizes the amount of interactions between unlike nanostars; otherwise, liquids

of two unlike nanostars could mix. Of course, orthogonality is a spectrum and the degree of mixing between two liquids depends on the free energy of interaction between two nanostars. In Table 3.1, as the free energy of binding for unlike sticky ends is more positive than the free energy of like sticky ends binding (see Table 1.1), we assumed that these pairs of sticky ends were orthogonal and should not interact significantly.

Sticky end	ΔG (kcal/mol)
SE23	-5.75
SE25	-5.35
SE49	-5.68
SE60	-8.17
SE35	-6.71

Table 3.1: Free energy of SE34 binding with unlike sticky ends.. The sticky ends listed here correspond to the ones shown in Fig 3.8. Free energies calculated using NUPACK3 model with the following parameters: 0.5 M NaCl, 20°C, which reflect experimental conditions. Free energies listed are the complex free energies. See Table 1.1 for a list of the free energies of like sticky ends binding.

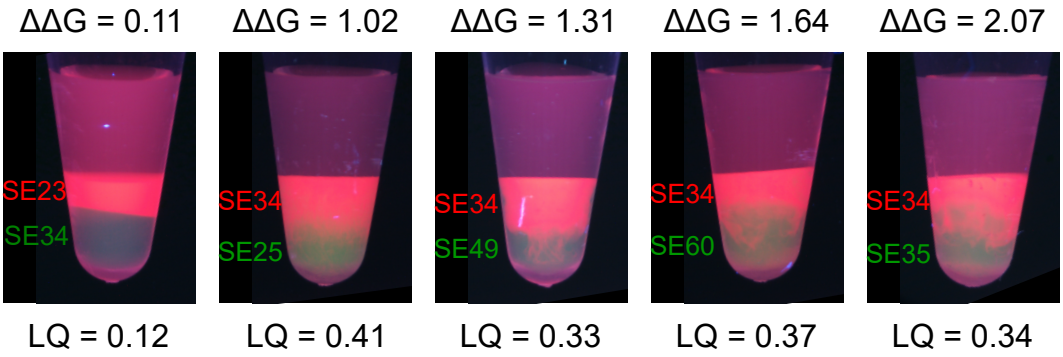

Figure 3.8: Initial attempts to form layers did not follow our expectations. 4-ns20-6SE34-v1 is dyed red in all images except for the leftmost one, where it is dyed green. As only 2% of nanostars are fluorescent, we assume that the change in fluorophore does not affect the material properties of liquids. We pairwise layered 4-ns20-6SE34-v1 with five other nanostars that have equal valency and arm length but different sticky end sequences, which is written next to each layer. The free energy difference (ΔΔG; kcal/mol) between each pair of sticky ends is written at the top of each image. ΔΔG increases from left to right. LQ of each image is written at the bottom. See Table 3.1 for a list of free energies of SE34 binding with unlike sticky ends. We had expected that larger ΔΔG would result in layers with lower LQ. Surprisingly, the two nanostars with the lowest ΔΔG (leftmost image) formed liquids that layered well, both qualitatively and quantitatively. Strands were STD.

Surprisingly, we found that the pairwise layer with the smallest ΔΔG (0.11 kcal/mol) had the lowest LQ (Fig 3.8; leftmost image), while pairs that had larger ΔΔG had a comparably worst layering quality, both qualitatively and quantitatively. We had

expected for the sample with the smallest $\Delta\Delta G$ to mix, as nanostars with such similar architectures would have similar densities.

We suspected that these results might be due to our assumption of the orthogonality of sticky ends. If unlike sticky ends are not orthogonal, liquids could potentially mix even with a sufficient density difference between them. As mentioned in Section 3.3, the effective sticky end free energy potentially differs from the theoretical one due to a combination of experimental factors and poor accuracy of the nearest-neighbor model to predict thermodynamics for short oligo lengths. We therefore suspected that the calculated free energies listed in Table 3.1 did not accurately reflect the orthogonality of sticky end pairs. We especially note that the the free energy of SE23 and SE34 was not significantly more positive than the other four pairs, which we would have expected given the results of Fig 3.8.

We were thus inspired to devise our own metric for determining sticky end orthogonality that did not depend on the thermodynamics of binding and instead minimized crosstalk by maximizing sequence differences. We examined our experiments thus far to determine if there was a pattern in pairs of sticky end sequences that would correlate with the layering quality observed. As a result, we developed a heuristic metric, which we term $[h, s]$, to measure the orthogonality of a pair of sticky end sequences.

$[h, s]$ is a two-value metric defined as follows. h is the Hamming distance between the two sticky end sequences. In the space of 6 nt palindromic sticky ends, the maximum Hamming distance is 6, and the minimum is 2. s is the slip factor, which we define as the number of canonical basepairs that can form if sticky ends aligned in antiparallel direction were to slip against each other by one base in either direction. In the space of 6 nt palindromic sticky ends, the maximum slip factor is 4 and the minimum is 0. Given the short length of sticky ends used, we assumed that slipping by more than one base would result in duplexes ≤ 4 bp in length. We assumed such small lengths to have very weak and transient interactions and therefore negligible. This, of course, ignores the fact that sticky ends could potentially strand displace into the arm domains, which would result in longer duplexes. We discuss how such assumptions contribute to the limitations of this metric at the end of this section.

Our hypothesis is that pairs of nanostars whose sticky ends have an $[h, s]$ value of [6,0] are orthogonal, which consequently leads to pairwise layers with good layering quality. This value essentially maximizes the Hamming distances and minimizes the slip factor. Conversely, sticky ends that have an $[h, s]$ value that is not [6,0] are

nonorthogonal. Nanostars with nonorthogonal sticky ends results in liquids with low layering quality unless there is an appreciable density difference between the two liquids. Note that if the densities of two liquids are equal, they will not form layers and will just mix even if sticky ends are orthogonal.

To see if this metric is a good predictor for layering quality, we systematically pairwise layered a single "constant" nanostar (4-ns15-6SE34-v2; dyed red in Fig 3.9) with twelve other nanostars (dyed green) that were of equal arm length and valency, but each had a different sticky end sequence such that each pairing with the constant nanostar resulted in a different sticky end $[h, s]$ value (first row of Fig 3.9). Our prediction was that out of these twelve pairs, the [6,0] sample would have the lowest LQ. In addition, we extended the arm lengths of these twelve nanostars by 3 bp and 6 bp and pairwise layered them with the constant one to see if increasing the density difference between the two liquids would improve layering quality. We expected LQ to decrease with increasing arm length differences. Table 3.2 lists the names of all nanostars used in this experiment. We also list the free energy of the constant nanostar's sticky end (SE34) binding with the sticky ends of the twelve other nanostars in Table 3.3.

Fig 3.9 shows images of the thirty-six pairs of liquids formed in this experiment. Each row shows pairs of liquids whose nanostars have an arm length difference of 0 bp (top row), 3 bp (middle row), and 6 bp (bottom row). Each column shows pairs of liquids whose nanostar sticky ends have the $[h, s]$ value listed at the top. The LQ of each image is written at the top (white text).

Qualitatively, we observe that for pairs of liquids whose nanostars are equal in arm length (top row), samples that had the most defined interfaces were [6,0] and [6,2]. Fig 3.10a quantitatively demonstrates this as well, as LQ is the smallest for these two samples out of the twelve. The [6,0] sample having the lowest LQ aligns with our prediction. Surprisingly, the [6,2] sample had the same LQ value as [6,0]. This is most likely a consequence of the heuristic $[h, s]$ metric not capturing more complex features, such as stacking energies, to accurately predict the orthogonality of every sticky end pair. As a result, we do not expect every predicted [6,0] sample to have low LQ (see Fig 3.12) nor do we expect every non-[6,0] sample to have high LQ, as demonstrated by this example. We also note that the free energies listed in Table 3.3, which represent thermodynamic predictions of sticky end orthogonality, do not correlate with the layering quality observed, further suggesting that these interaction energies do not provide a good metric for determining sticky end orthogonality for

our experiments.

In observing each column of Fig 3.9, we qualitatively and quantitatively (Fig 3.10b) observe that the layering quality improves as the arm length difference between nanostars increases. Fig 3.11 shows the concentration of each liquid displayed in Fig 3.9. Red bars correspond to the concentration of the constant nanostar, while the green bar in each plot is the concentration of the green liquid in the corresponding image in Fig 3.9. As the arm length of a green liquid nanostar with a specific sticky end increases, we see a decrease in the concentration (see Appendix I). This corresponds to the trend observed in Section 3.3. The density difference between the red and green liquid increases with increasing arm length difference between the two nanostars and allows non-[6,0] pairs that initially mixed when arm lengths were equal to now have improved layering quality. This aligns with our initial theory that non-[6,0] pairs of liquids require appreciable density differences to achieve low LQ. See Appendix J for a discussion on the reproducibility of this experiment.

We remark that there is no ordering of $[h, s]$ values that are not [6,0]. For example, we do not observe that liquids with an $[h, s]$ value of [6,1] necessarily have a lower LQ than ones with a value of [2,2]. See Appendix H for a more in-depth discussion on this topic.

	Δ0bp	Δ3bp	Δ6bp
[6,0]	4-ns15-6SE23-v2	4-ns18-6SE23-v2	4-ns21-6SE23-v3
[6,1]	4-ns15-6SE31-v1	4-ns18-6SE31-v2	4-ns21-6SE31-v2
[6,2]	4-ns15-6SE53-v1	4-ns18-6SE53-v2	4-ns21-6SE53-v2
[6,3]	4-ns15-6SE50-v1	4-ns18-6SE50-v2	4-ns21-6SE50-v2
[6,4]	4-ns15-6SE60-v1	4-ns18-6SE60-v2	4-ns21-6SE60-v2
[4,0]	4-ns15-6SE36-v2	4-ns18-6SE36-v2	4-ns21-6SE36-v3
[4,1]	4-ns15-6SE45-v1	4-ns18-6SE45-v2	4-ns21-6SE45-v2
[4,2]	4-ns15-6SE30-v1	4-ns18-6SE30-v2	4-ns21-6SE30-v2
[4,3]	4-ns15-6SE27-v1	4-ns18-6SE27-v2	4-ns21-6SE27-v2
[2,0]	4-ns15-6SE42-v2	4-ns18-6SE42-v2	4-ns21-6SE42-v2
[2,1]	4-ns15-6SE44-v1	4-ns18-6SE44-v2	4-ns21-6SE44-v2
[2,2]	4-ns15-6SE35-v1	4-ns18-6SE35-v2	4-ns21-6SE35-v2

Table 3.2: The names of all green liquid nanostars used in Fig 3.9. The constant nanostar is 4-ns15-6SE34-v2 (red liquid in Fig 3.9). Each row of nanostars has a unique sticky end and $[h, s]$ value with SE34, which is listed in the first column. Each column of nanostars has an arm length difference with the constant nanostar that is listed in the first row.

[h,s]	Sticky end	ΔG (kcal/mol)
[6,0]	SE23	-5.75
[6,1]	SE31	-5.23
[6,2]	SE53	-5.25
[6,3]	SE50	-6.38
[6,4]	SE60	-8.17
[4,0]	SE36	-8.23
[4,1]	SE45	-5.32
[4,2]	SE30	-5.87
[4,3]	SE27	-6.09
[2,0]	SE42	-7.11
[2,1]	SE44	-5.38
[2,2]	SE35	-6.71

Table 3.3: Free energy of SE34 binding with unlike sticky ends. We list the free energy of SE34 binding with each of the twelve sticky ends listed in Table 3.2. These represent the thermodynamic predictions of the orthogonality of sticky ends. We list the $[h, s]$ value for each sticky end pair in the first column. Free energies calculated using NUPACK3 model with the following parameters: 0.5 M NaCl, 20°C, which reflect experimental conditions. Free energies listed are the complex free energies. See Table 1.1 for a list of the free energies of like sticky ends binding.

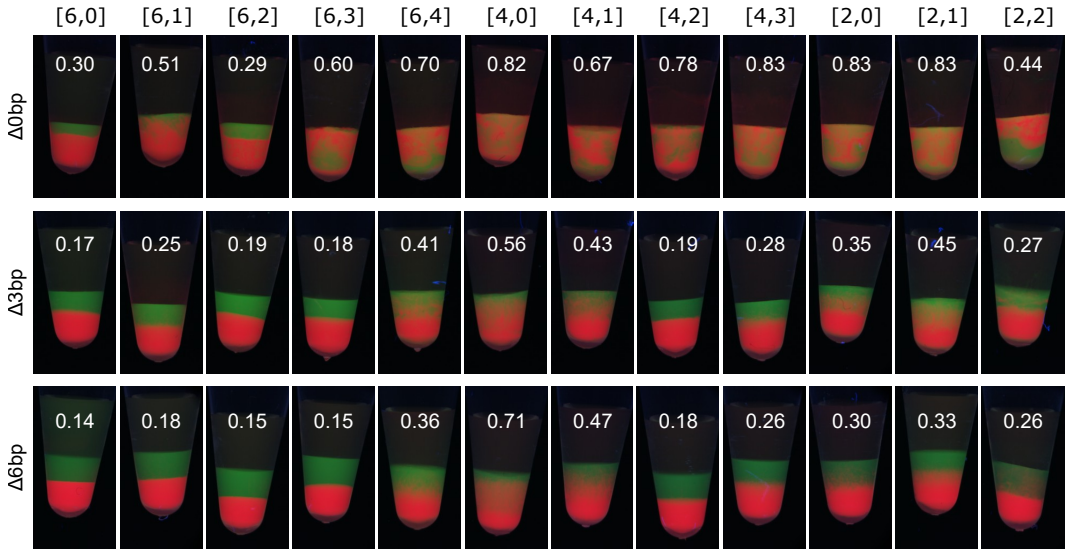

Figure 3.9: Pairwise liquids to test $[h, s]$ **metric.** The red liquid nanostar in all samples is 4-ns15-6SE34-v2. The name of green liquid nanostars are listed in Table 3.2. The arm length difference between red and green liquid nanostars is 0 bp, 3 bp, and 6 bp in the top, middle, and bottom row, respectively. Each column is a unique sticky end pair and $[h, s]$ value, which is written at the top. The LQ value of each image is written in white text. In general, we observe that LQ decreases as arm length of the green liquid nanostar increases. In addition, the [6,0] sample in the top row, where nanostar architectures are equal, has the lowest LQ value.

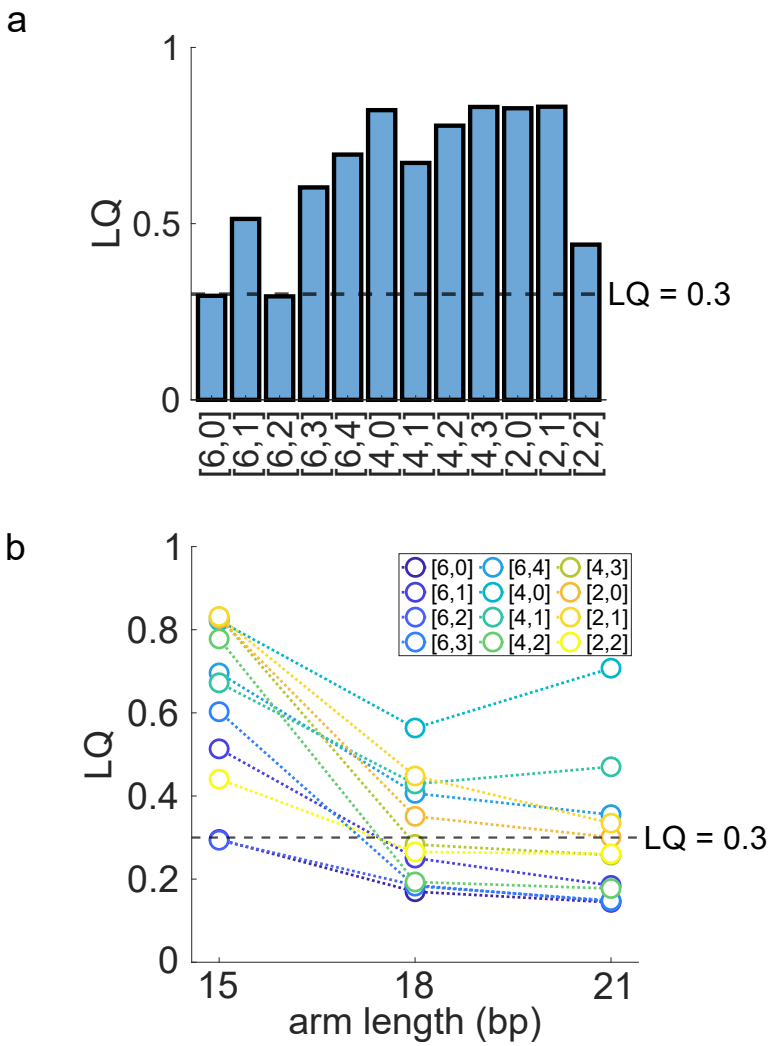

Figure 3.10: LQ as a function of $[h, s]$ and arm length. (a) LQ of the first row of images in Fig 3.9 as a function of $[h, s]$. Nanostars in these samples had equal arm lengths. [6,0] and [6,2] had the lowest LQ values. (b) LQ of each $[h, s]$ value in Fig 3.9 as a function of arm length. As arm length increases, the LQ value decreases, indicating that larger density differences between liquids improves layering quality. Dashed black lines on both graphs represent the optimal LQ value of 0.3.

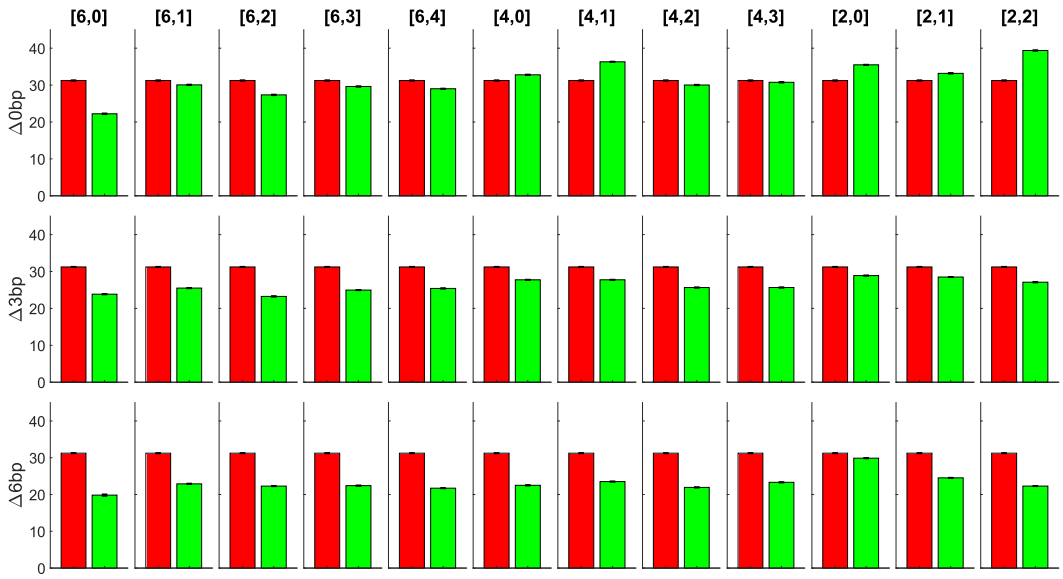

Figure 3.11: Liquid phase concentrations of liquids in corresponding images of Fig 3.9. Concentrations are in units of mg/mL. Red bars are the concentration of the constant nanostar. Green bars are the concentration of green liquid nanostars. For each sticky end pair, the concentration of green liquid nanostars decrease with increasing arm length. See Appendix I for an extended discussion on this topic.

While this initial experiment seems to be in line with our hypothesis, we were concerned about how this result might be biased due to the density difference of the [6,0] sample in the first row of Fig 3.11. We note that in the first row, where nanostars had equal arm lengths, the [6,0] sample had the largest concentration difference between the red and green liquid, which might suggest that sticky end orthogonality did not play a large role in the layering quality. To try and eliminate this bias, we performed an experiment following the same concept as the one shown in Fig 3.9, but this time the $[h, s]$ value of all sticky end pairs was [6,0]. In this way, we can obtain a range of samples with varying density differences between paired liquids and observe if the magnitude of this difference affects the layering quality of [6,0] pairs. Table 3.4 lists the names of all nanostars used in this experiment. Note that the constant nanostar (4-ns15-6SE21-v2; dyed red in Fig 3.12) in this experiment is different from the one used in Fig 3.9. Table 3.5 lists the free energy of the constant nanostar's sticky end (SE21) binding with the other sticky ends used in this experiment.

Fig 3.12 and 3.13 shows images of the pairwise liquids and the associated liquid phase concentrations, respectively. The top of each column is labeled with the free energy difference between the red and green liquid nanostar sticky ends. The sticky end free energy difference increases from left to right.

ΔΔG (kcal/mol)	Δ0bp	Δ3bp	Δ6bp
0.73	4-ns15-6SE24-v1	4-ns18-6SE24-v1	4-ns21-6SE24-v1
1.52	4-ns15-6SE34-v3	4-ns18-6SE34-v2	4-ns21-6SE34-v2
1.87	4-ns15-6SE44-v1	4-ns18-6SE44-v2	4-ns21-6SE44-v2
2.23	4-ns15-6SE43-v3	4-ns18-6SE43-v1	4-ns21-6SE43-v1
3.16	4-ns15-6SE60-v1	4-ns18-6SE60-v2	4-ns21-6SE60-v2
3.59	4-ns15-6SE35-v1	4-ns18-6SE35-v2	4-ns21-6SE35-v2
4.52	4-ns15-6SE54-v1	4-ns18-6SE54-v1	4-ns21-6SE54-v1

Table 3.4: The names of all green liquid nanostars used in Fig 3.12. The constant nanostar is 4-ns15-6SE21-v2 (red liquid in Fig 3.12). The first column lists the sticky end free energy difference (ΔΔG) of SE21 and the sticky end of that row. Each column of nanostars has an arm length difference with the constant nanostar that is listed in the first row.

[h,s]	Sticky end	ΔG (kcal/mol)
[6,0]	SE24	-4.93
[6,0]	SE34	-5.59
[6,0]	SE44	-5.30
[6,0]	SE43	-6.12
[6,0]	SE60	-5.86
[6,0]	SE35	-5.23
[6,0]	SE54	-5.11

Table 3.5: Free energy of SE21 binding with unlike sticky ends. We list the free energy of SE21 binding with each of the seven sticky ends listed in Table 3.4. These represent the thermodynamic predictions of the orthogonality of sticky ends. The $[h, s]$ value of all sticky end pairs is [6,0]. Free energies calculated using NUPACK3 model with the following parameters: 0.5 M NaCl, 20°C, which reflect experimental conditions. Free energies listed are the complex free energies. See Table 1.1 for a list of the free energies of like sticky ends binding.

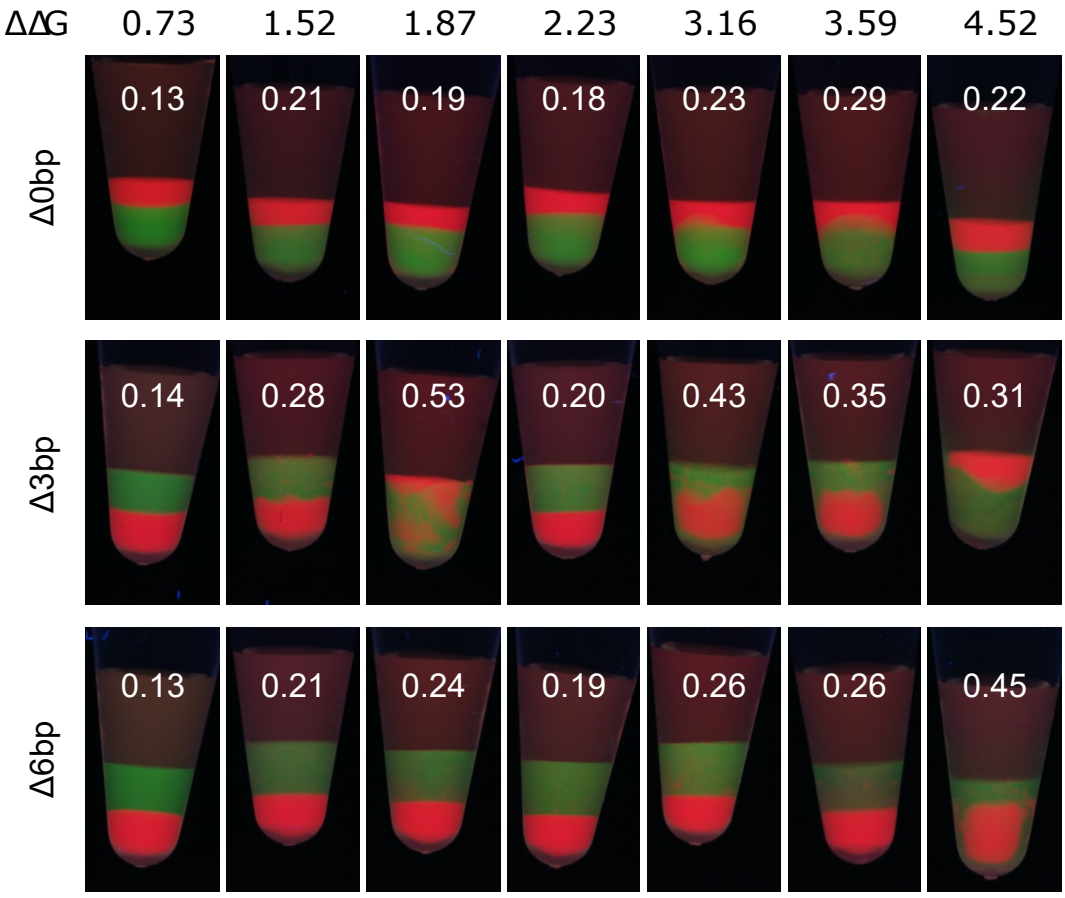

Figure 3.12: Pairwise layers of nanostars with [6,0] sticky ends. The red liquid nanostar in all samples is 4-ns15-6SE21-v2. The name of green liquid nanostars are listed in Table 3.4. The arm length difference between red and green liquid nanostars is 0 bp, 3 bp, and 6 bp in the top, middle, and bottom row, respectively. The $[h, s]$ value of all pairs of sticky ends is [6,0]. Each column is a unique sticky end pair with the free energy difference (ΔΔG; kcal/mol) written at the top. The LQ value of each image is written in white text. In the top row of images, we observe that the red liquid is layered on top of the green in all samples. In the bottom row, the order flips. This indicates that the densities of both liquids have to be equal at some arm length difference, which we believe occurs around Δ3 bp. Because densities are similar, we see a range of morphologies in the middle row, resulting in higher LQ values.

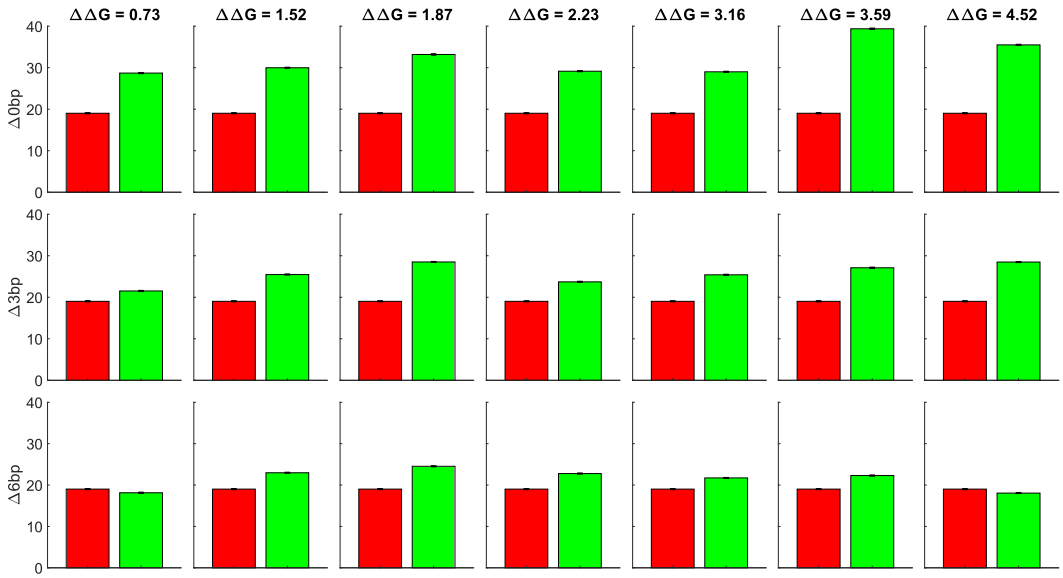

Figure 3.13: Liquid phase concentrations of liquids in corresponding images of Fig 3.12. Concentrations are in units of mg/mL. Red bars are the concentration of the constant nanostar. Green bars are the concentration of green liquid nanostars. The order of concentrations in the middle and bottom row do not correspond with the order of layers in Fig 3.12, which we attribute to some systematic error in measurement. See Fig 3.14 for adjusted concentrations.

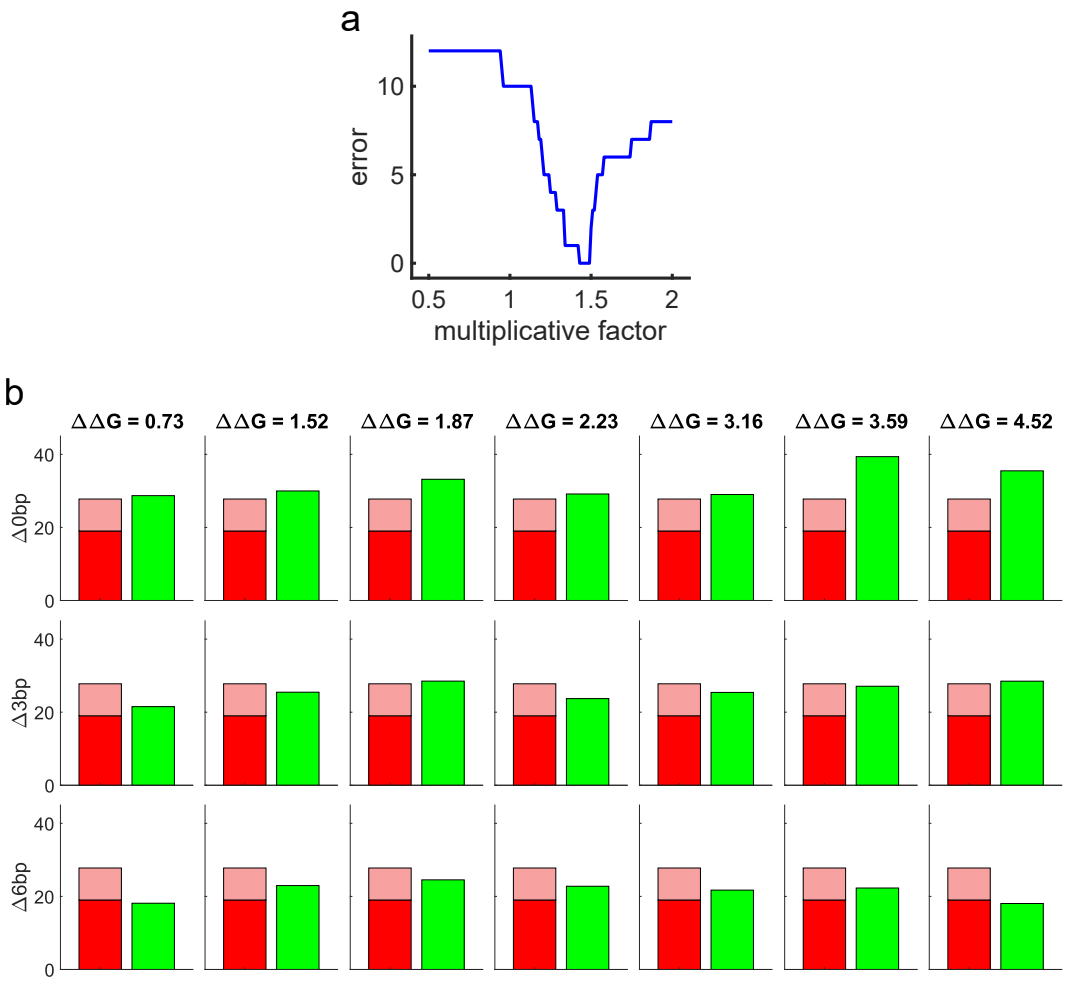

Figure 3.14: Adjusted concentration of 4-ns15-6SE21-v2 to account for systematic errors in measurement. (a) Number of discrepancies (error) between the quantitative data in Fig 3.13 and the qualitative data in Fig 3.12 as a function of multiplicative factors applied to the red liquid concentration of Fig 3.13. Error is zero in the range of 1.43 and 1.49. We multiply the measured red liquid concentration by the median value of 1.46. (b) We re-plot Fig 3.13 with this adjusted red liquid concentration (colored a lighter shade to indicate adjustment). The order of concentrations for each pairwise liquid now aligns with the order of layers observed in the Fig 3.12. While the magnitude of the red liquid concentration may not exactly be this value, the difference in concentration between each red and green liquid is more accurately represented with this adjustment.

Unlike what we observed in the previous experiment, we do not see a decrease in LQ as the arm length difference increases because the order of the layers flip. In the first row, where the arm length of both nanostars are equal, we observe that the red liquid is layered on top of the green across all samples; however, in the bottom row, where the arm length difference is 6 bp, we observe that the green liquid is now layered on top of the red. This layer flipping suggests that the densities of the red and green liquid have to be equal at some point as the arm length difference increases. We believe that this occurs when the arm length difference is around 3 bp, which results in the various morphologies and higher LQ values observed in the middle row. As the density of red and green liquid are approximately equal for most samples in the middle row, separation of the two liquids is difficult at the centrifugation speeds we employ, resulting in the nonlinear interfaces (e.g. second and seventh column) and "encapsulating" (e.g. fifth and sixth column) appearances we observe. In particular, for samples that have an "encapsulating" appearance, we suspect that the red liquid was initially layered on top of the green before centrifugation. In other words, the transition temperature of the red liquid is lower than that of the green. However, the red liquid is denser than the green liquid, but still close in value, such that during centrifugation, the red liquid "sieves" its way through the green liquid. Since the densities of the two liquids are probably close in value, the centrifugation speed used was not able to push the red liquid all the way through the green, thus resulting in this "encapsulating" appearance. The densities of the red and green liquid for the sample with $\Delta\Delta G = 1.87$ (third column) are probably closer in value compared to other samples in this row, resulting in the more mixed appearance. At higher centrifugation speeds, we believe samples with such morphologies would separate more.

We observe that the LQ of all samples shown in the first and bottom row (with the exception of 4-ns21-6SE54-v1) of Fig 3.12 have an LQ ≤ 0.3. Fig 3.13 shows that the concentration difference between these pairwise liquids vary from almost zero to 20 mg/mL. This demonstrates that orthogonal sticky ends—with the term orthogonal here quantified by an $[h, s]$ value of [6,0]—potentially helps achieve defined layers regardless of the density difference between liquids.

We acknowledge that the order of liquid phase concentrations shown in Fig 3.13 do not completely correlate with the order of layers observed in Fig 3.12. These discrepancies are particularly apparent when comparing the middle and bottom rows of both figures. We believe that the error mainly lies in our quantitative

measurement of the concentrations. As mentioned in Section 2.3, our capillary method is precise but not accurate due to our reliance on direct measurements of the gas phase concentration. The gas phase can be composed of nanostars—both properly formed and malformed—single strands, contaminants, and microscopic droplets that did not sediment to the bottom of the capillary. As we cannot determine the exact composition of species in the gas phase, we assume that measurements are of a fully formed nanostar and use the extinction coefficient and molecular weight associated with such a structure. This would result in a systematic error in our measurements.

To adjust for this systematic error, we multiply the concentration of the red liquid by some constant such that the quantitative data agrees with the order of layers in the images. We believe that the order of layers shown in Fig 3.12 is accurate, as liquids should layer according to their inherent densities. Fig 3.14a shows the number of discrepancies (error) between the quantitative and qualitative data as a function of a range of multiplicative factors applied to the red liquid concentration. In other words, when we multiply the red liquid concentration by some constant factor, the error is the number of plots that do not align with the order of layers in the images. The error is zero between the range of 1.43 and 1.49. We therefore take the median value of 1.46 and multiply the measured red liquid concentration by this factor. Fig 3.14b shows this adjusted concentration alongside the measured concentration of the green liquids. The order of concentrations for each pairwise liquid now aligns with the order of layers observed in the images. While the magnitude of the red liquid concentration may not exactly be this value, the difference in concentration between each red and green liquid is more accurately represented with this adjustment.

Relationship between sticky end orthogonality and density differences

To help visualize the relationship between sticky end orthogonality and density difference between pairs of liquids, we plot LQ as a function of liquid phase concentration differences in Fig 3.15. The concentration differences of Fig 3.15a and b are calculated from the measured concentrations as shown in Fig 3.13, while c and d plot the differences from the adjusted red liquid concentration shown in Fig 3.14. We plot the x-axis of one graph in units of molarity (μM; Fig 3.15a and c) and the other in units of mass concentration (mg/mL; Fig 3.15b and d) to demonstrate the universality of the relationship in either unit. We observe that non-[6,0] data points (circles) with LQ $\leq$ 0.3 tend to have higher concentration differences, while the majority of [6,0] data points (crosses) have an LQ value less than 0.3 at even low

concentration differences. This suggests for pairs of liquids with similar densities, selection of orthogonal sticky end sequences can improve layering quality. If sticky ends are not orthogonal, increasing the density difference between the two liquids can also improve layering quality. See Appendix K for a comparison of the $[h, s]$ metric and nearest-neighbor model in predicting layering quality.

The relationship between sticky end orthogonality and density differences also suggests a tradeoff in the number of layers one can form and the orthogonality of nanostars. One could potentially relax the stringency of orthogonality and still obtain good layering quality but with only a few liquids that have large density differences. On the other hand, many layers can be obtained using liquids with small density differences but require high sticky end orthogonality.

Limitations of $[h, s]$ metric

The $[h, s]$ metric is very simplistic. It considers only the number of canonical basepairs that form if sticky ends were to slip by only one base. This simplicity ignores many factors, such as bulge loop penalties, stacking energies, any noncanonical basepair formation, and interactions between sticky ends and arm domains. The consequences of ignoring these factors on layering quality are most apparent in samples containing two nanostars of similar architecture, as any differences in arm length or valency would introduce density differences as a contributing factor towards layering quality. For example, the layering quality of the Δ0bp, [6,2] sample in Fig 3.9 (first row, third column) is similar to the Δ0bp, [6,0] sample (first row, first column). One possible explanation is that the adjacent base in the arm domain of the green liquid nanostar potentially has strong stacking interactions with the sticky end. This strong stacking could stabilize like sticky end interactions, which could lead to the high layering quality we observe, even though $[h, s]$ is not [6,0]. Another example is the Δ0bp, ΔΔG = 3.59 kcal/mol sample (first row, sixth column) in Fig 3.12, where the $[h, s]$ value of this pair of sticky ends is [6,0]. While LQ for this sample is less than 0.3, we observe that the interface between liquids is blurred (this is also an example of how LQ is an estimation of layering quality, not a definitive metric). In this sample, sticky ends could potentially be interacting with arm domains, leading to binding of unlike nanostars and the blurred interface we observe.

The $[h, s]$ metric comes with a tradeoff between accuracy and complexity in predicting sticky end orthogonality, which in turn contributes towards predicting layering

quality. The simplicity of the metric does not capture all aspects of sticky end interactions, but is sufficient in predicting layering quality for most instances without the need for a complex model.

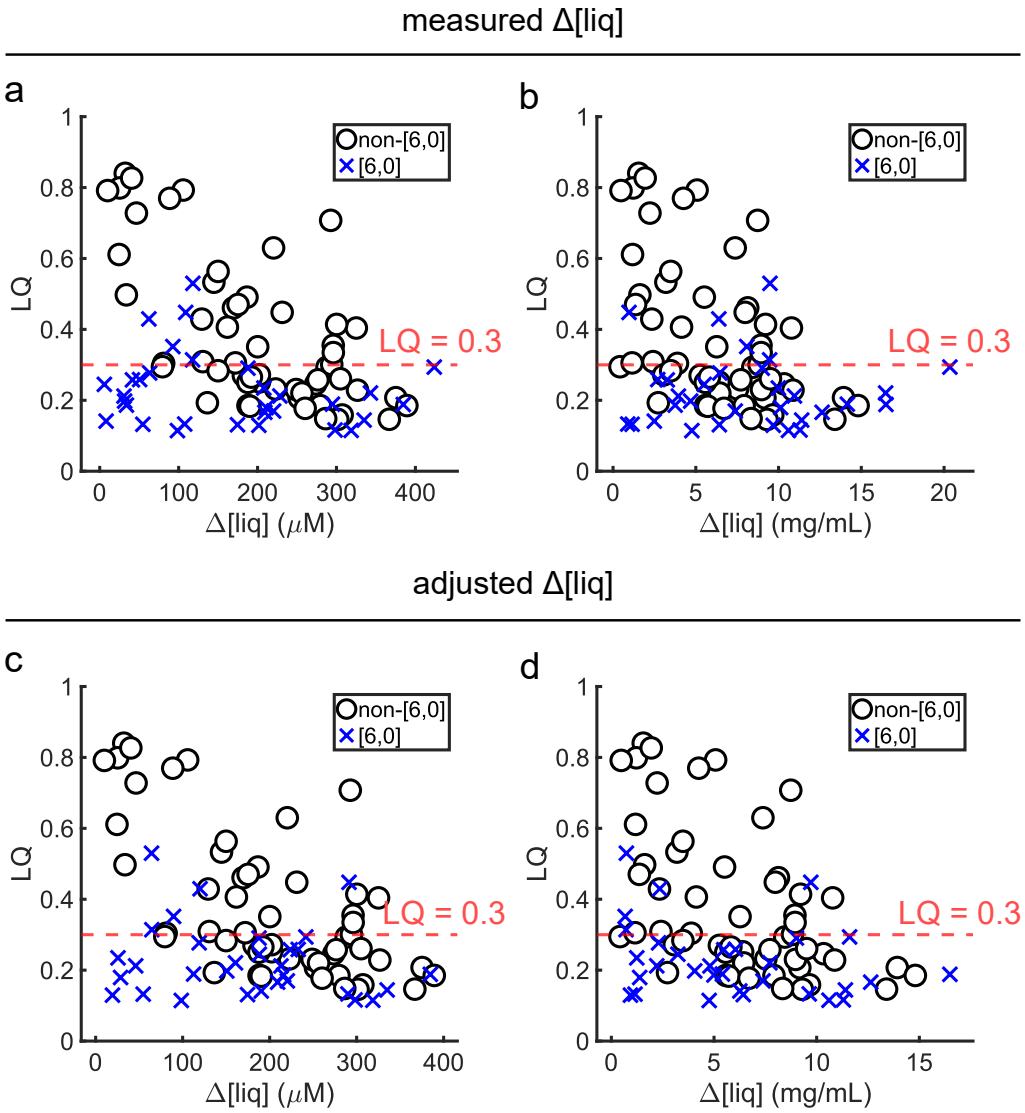

Figure 3.15: LQ as a function of liquid phase concentration differences. LQ of samples from Fig 3.9 and 3.12 as a function of their liquid phase concentration differences in (a,c) molarity and (b,d) mass concentration units. The plotted concentration differences of a and b are the measured concentrations taken from Fig 3.11 and 3.13, while c and d plot the adjusted concentration differences from Fig 3.14. The majority of [6,0] data points (blue crosses) have an LQ value less than 0.3 in a wide range of concentration differences, while non-[6,0] data points (black circles) tend to have low LQ when concentration differences are large.

3.5 Forming multilayer orthogonal DNA liquids

Using the lessons we learned in the previous sections, we successfully designed five nanostars to create five immiscible DNA liquids in a tube (Fig 3.16a). The clear layer at the bottom of the tube is perfluorodecalin, an inert solution that acts as a base for the liquids to sit upon. This is to prevent markings on the plastic tube from distorting the view of the liquids.

Using our knowledge of the relationship between density and nanostar features explored in Section 3.3, we designed nanostars such that those that form liquids near the top have lower valencies, longer arm lengths, and weaker sticky end sequences. Conversely, liquids towards the bottom of the tube were composed of nanostars that had higher valencies, shorter arm lengths, and stronger sticky end sequences. Fig 3.16b shows the measured liquid phase concentration of the five nanostars. The concentration increases as we go from the top to bottom layer and agrees with the order of layers we observe in Fig 3.16a.

The sticky end sequences of nanostars that formed liquids adjacent to each other were chosen such that they had an $[h, s]$ value of [6,0] (see Fig 3.16c). In our limited design space of 6 nt palindromic sequences, it was not possible to find five sticky end sequences where every pair satisfied the orthogonality requirement of [6,0]. We therefore decided that it was most important for adjacent liquids to satisfy this requirement in order to obtain defined interfaces between layers. Fig 3.16d shows an image of the same five liquids, but layers are dyed in alternating red and green dyes. This is to allow for the creation of a two-channel image and calculation of LQ for adjacent layers, which are written in white text (see Appendix L). LQ values are all less than 0.3 with the exception of the value for the bottom two layers, which is a little higher than our standard of 0.3, but we view the overall formation of five immiscible layers as successful.

We note that in an initial design, we set the arm length of the nanostar that forms the yellow liquid to be 15 bp. However, initial experiments showed that it would layer on top of 4-ns15-6SE29-v1 (dyed orange in Fig 3.16a and dyed red in Fig 3.16e) despite the fact that the free energy of SE17 was predicted to be more negative than that of SE29. This again demonstrates that the effective free energy of sticky ends differs from what is theoretically predicted. Using the concepts we learned from our experiment in Fig 3.7, where we reordered layers by changing arm lengths, we decreased the arm length of the yellow nanostar to 10 bp to ensure that the order of liquids will be as desired.

Five layers is potentially the maximum number of layers achievable under the particular design space and experimental conditions that we work under. However, if we expanded to the usage of longer palindromic (or maybe even non-palindromic) sticky ends or other nanostar architectures (e.g. anisotropic arm lengths, lack of free bases at the junction) or even having multiple monomer species per liquid, the number of layers one could form in a single test tube could increase (perhaps to ten layers or more!). The only practical limitation might be the solubility limit of DNA, as in our experience, each layer requires a final concentration on the order of ~100 μM to be visible by the naked eye; this experimentally suggests that the starting concentration of strands has be on the order of millimolars.

3.6 Summary of design principles

We summarize here the design principles discussed in this chapter. When designing nanostars to form liquid layers, there are two main properties to consider: layering order and layering quality.

Layering order is determined by the density of the liquid, which in turn is determined by the geometric features of the nanostar. In general, nanostars with shorter arm lengths, stronger sticky ends, and higher valencies tend to form denser liquids. Tuning of any one of these nanostar features can modulate the density of liquids and can allow one to reorder layers as desired.

Layering quality is determined by a combination of density differences between adjacent layers and the sticky end orthogonality of nanostars. We use the heuristic $[h, s]$ metric to define the orthogonality of sticky ends and state that a pair of sticky ends with a value of [6,0] is considered to be orthogonal; all other values are considered non-orthogonal. If a pair of liquids has small density differences, then it is recommended to choose a pair of sticky end sequences where $[h, s] = [6, 0]$. If a pair of sticky end sequences do not have an $[h, s]$ value of [6,0], then it is recommended to design nanostars such that the density difference between liquids is large.

As a first step for forming multilayer liquids, we recommend choosing sticky end sequences first. One can then design the arm lengths and valencies based on the orthogonality and free energy of the chosen sequences.

a

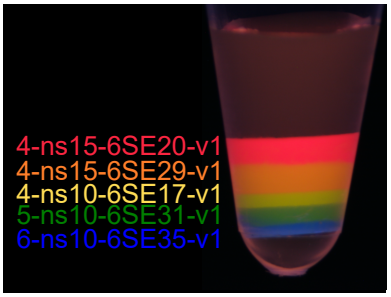

b

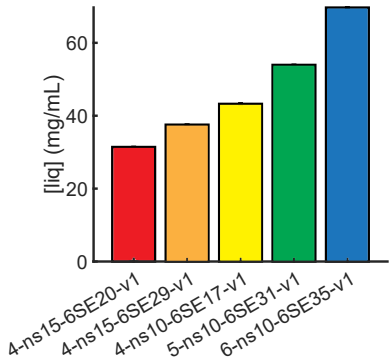

c

	20	29	17	31	35
20		[6,0]	[2,3]	[6,1]	[6,1]
29			[6,0]	[2,2]	[6,0]
17				[6,0]	[4,1]
31					[6,0]
35					

d

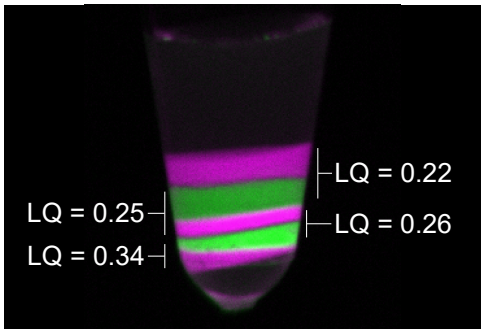

e

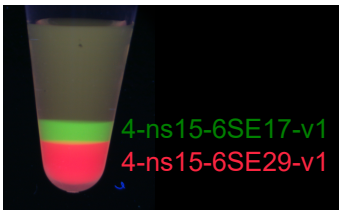

Figure 3.16: Five layer liquids. (a) We designed five nanostars to create five liquid layers. Nanostar names are written next to their corresponding liquid. Nanostars with shorter arm lengths, higher valency, and stronger sticky end sequences layered towards the bottom. (b) Liquid phase concentration of the five nanostars used. The concentration increases going from the red to blue liquid, which corresponds to the order we observe in (a). (c) Table of all pairwise $[h, s]$ values between the five sticky ends used. Adjacent layers (highlighted in purple) were designed to have a value of [6,0]. Non-adjacent layers could have any $[h, s]$ value. (d) Two-channel image of the five layers. LQ values of adjacent layers are written in white text. (e). In initial tests, the green liquid nanostar, which had an arm length of 15 bp and SE17, layered on top of 4-ns15-6SE29-v1 (dyed red in this image; dyed orange in (a)). As SE17 was not orthogonal with SE20, we decreased the arm length to 10 bp so that the nanostar with SE17 (4-ns10-6SE17-v1; dyed yellow in (a)) would layer below 4-ns15-6SE29-v1.

Chapter 4

TOWARDS MACROSCOPIC SEPARATION OF BIOMOLECULES

We impart functionality to these macroscopic liquid layers by modifying nanostars with a binding moiety and demonstrate localization of biomolecules, such as oligos and streptavidin, within them. These experiments are a step towards a potential multiplexed method of separating high-value biological molecules. The use of a binding moiety like aptamers in conjunction with DNA nanostars to form macroscopic liquid compartments makes this a novel separation technique that can be considered a new type of aptamer based affinity chromatography (G. Perret and E. Boschetti, 2017). However, unlike traditional affinity chromatography, our proposed method does not require magnetic beads or a column support, nor does it subject the target to potentially harsh conditions to strip it from said support. In addition, the separation of multiple targets can occur in a single binding step unlike traditional methods which would require serially performing multiple steps.

We localize oligos in a multilayer DNA liquid system by modifying nanostars with tag regions complementary to the target strand. We also demonstrate, in a separate system, localization of fluorescent streptavidin to a single DNA liquid layer by modifying nanostars with a streptavidin-binding aptamer. After localization of targets in each system, we added strands complementary to either the tag region or the aptamer. This caused targets to be displaced from the liquid and released into the gas phase.

These rudimentary experiments provide insight into the mechanics of how to realistically use these liquids as a separation tool. For example, we found that the uptake of oligos inside of these liquids can take on the order of hours unless we provided a mechanical force, such as vigorous pipetting or vortexing, to increase the kinetics of localization. The use of such force, however, would be detrimental to fragile proteins. We discuss such issues and potential solutions to advance towards our goal of implementing macroscopic liquids as a novel separation method at the end of this chapter.

4.1 Localization and displacement of oligonucleotides

As a simple first attempt, we localized oligos within DNA liquids as they can easily bind to nanostars via simple basepairing. Previous studies have demonstrated successful localization of nucleic acids of varying sizes and structures within microscopic DNA condensates. Nguyen *et al*. partitioned various sizes of long, double-stranded DNA linkers into DNA liquid droplets (D. T. Nguyen et al., 2019). They designed linkers to have the same sticky end sequence as the phase-separated nanostars, such that uptake would be via binding of the overhangs. They found that partitioning depends on the length of the linker, with long strands being excluded from droplets due to the characteristic mesh size of liquids. Do *et al*. similarly designed multiple DNA "clients" that can simultaneously partition into condensates via toeholds and demonstrate accelerated strand displacement reactions within these droplets (Do et al., 2022). Unlike the Nguyen *et al*. study, Do *et al*. specifically designed their clients to bind to toeholds on the arm domains of nanostars instead of to sticky ends. They found that high concentrations of clients binding to the nanostar sticky ends would result in the dissolution of the condensate.

In our initial design, we designed a nanostar-tag structure where one arm of the nanostar is extended and called a tag domain. The tag domain can bind to a complementary fluorescent reporter strand (Fig 4.1a; *left*). In our experiments, we initially formed a two-layer system, where each liquid layer was composed of a mixture of the typical nanostar and nanostar-tag structures. For each liquid, 2% of monomers were substituted with a nanostar-tag structure that was bound to a unique reporter strand. Initial formation of liquid layers would thus be fluorescent (Fig 4.2a-i). To selectively quench the fluorescence of just one layer, we designed quencher strands that were complementary to the reporter (Fig 4.1a; *center*). To recover fluorescence, we designed a displacer strand that can undergo strand displacement with the quencher (Fig 4.1a; *right*). We thus can add quencher and displacer strands sequentially to quench or recover the fluorescence of each layer individually. The use of displacer strands is to mimic the idea of releasing targets into gas phase for downstream collection and use.

After each addition of an oligo, the solution was vigorously pipetted and vortexed for at least 30-60 seconds at room temperature. This was to allow for faster localization of strands into condensates. Afterwards, tubes were centrifuged for 3-10 minutes to allow for reformation of layers. We note that we did not use a refrigerated centrifuge for these experiments and observed that the rotor did heat up with each subsequent

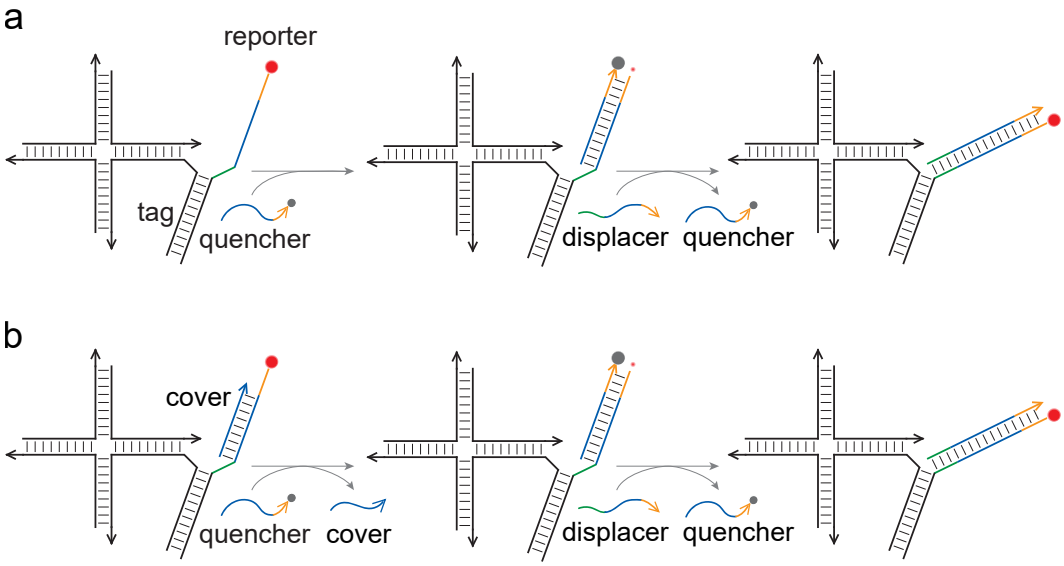

Figure 4.1: Nanostar-tag structures for capturing oligos. (a) In our initial design, nanostar-tag structures have an extended arm that binds to a fluorescent reporter strand (*left*). Addition of a complementary quencher strand will quench the fluorescence of the liquid (*center*). To recover fluorescence, the addition of a displacer strand displaces the quencher strand from the reporter (*right*). (b) To solve the orthogonality issues observed in Fig 4.2b-ii, we annealed a cover strand on to the single-stranded region of the reporter to inhibit any spurious interactions. The subsequent addition of quencher and displacer strands remains unchanged.

spin. Quencher and displacer strands were added at a final concentration that was twice the concentration of the reporter.

Fig 4.2a shows our initial experiment to sequentially quench and recover fluorescence in a two-layer system. After formation of the two layers (Fig 4.2a-i), we sequentially add the corresponding quencher and displacer strands for the yellow liquid to quench and then recover fluorescence (Fig 4.2a-ii and iii). We next repeat this for for the green liquid (Fig 4.2a-iv and v). We observe selective quenching and recovery of fluorescence for each liquid upon the addition of the corresponding oligo. Localization of each strand was on the order of minutes.

When we repeat this experiment by quenching the green liquid first, however, we observe that the fluorescence of the yellow liquid is partially quenched (Fig 4.2b-ii). This suggests the quencher for the green liquid potentially has spurious interactions with the reporter of the yellow liquid. We observe that this issue is even more pronounced in Fig 4.3a and b, which shows attempted sequential fluorescence quenching and recovery in another two-layer system. In Fig 4.3a, we first attempted to quench the yellow liquid, but observed that both the yellow and red liquid were

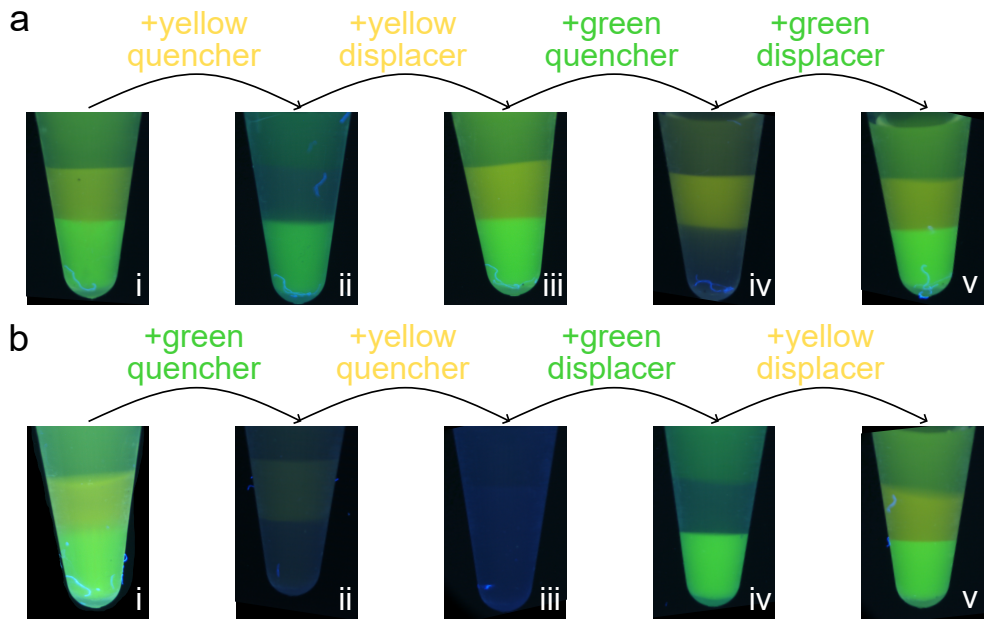

Figure 4.2: Localization of oligos via nanostar-tag structures. Two layer system with each liquid composed of 2% nanostar-tag structures. Yellow liquid nanostar is 4-ns25-6SE48-v1. Green liquid nanostar is 4-ns20-6SE49-v3. Strands were STD. (a) We sequentially add the corresponding quencher (ii) and displacer (iii) strand to quench and recover fluorescence, respectively, of the yellow liquid. We repeat the same procedure for the green liquid (iv and v) and observe a similar behavior. (b) When we attempt to quench the green liquid first, we observe simultaneous quenching of the yellow liquid as well, suggesting spurious interactions between the yellow liquid reporter and the green liquid quencher.

partially quenched, suggesting that the yellow quencher localized within both liquids. The addition of the corresponding displacer strand allowed for fluorescence recovery of the yellow liquid, but complete quenching of the red, indicating that most of the yellow quencher was now localized within the red liquid. Fig 4.3b demonstrates the same problems when we attempt to quench the red liquid first.

To resolve this issue, we annealed our nanostar-tag structures with a cover strand to inhibit any spurious interactions with the previously single-stranded reporter domain (Fig 4.1b; left). We test this "covered" nanostar-tag design in Fig 4.3c. We now observe that upon addition of the yellow quencher, only the fluorescence of the yellow liquid is quenched. Addition of the yellow displacer also only affects the fluorescence recovery of the yellow liquid. The same behavior is observed upon addition of red quencher and displacer. We note that in Fig 4.3c-iv, the fluorescence of the red liquid was not completely quenched upon addition of the corresponding quencher despite multiple rounds of pipetting and vortexing. Addition of the cover strand potentially increases the viscosity of the liquid, which could slow the partitioning

of oligos.

We note an interesting observation about the layering quality of samples in Fig 4.3. The appearance of each tube in all three experiments initially shows an ill-defined interface between the two liquids (Fig 4.3a-i, b-i, c-i). While this is not as surprising for Fig 4.3a-i and b-i, as these samples were annealed at a rate of 0.5°C/min, the sample in Fig 4.3c-i was annealed at a rate of 0.1°C/min, which was found to be an optimal annealing rate as described in Section 3.1. We had also expected that the addition of a cover strand to prevent spurious interactions would further improve the layering quality of Fig 4.3c-i compared to Fig 4.3a-i and b-i, but that does not appear to be the case. However, the addition of each oligo seems to sharpen the interface, such that by the end of the experiment, there is a clearly defined interface between the two liquids in all three cases. We suspect that that the temperature of the tube increased with each spin in the centrifuge. This could allow unlike nanostars that were interacting to re-anneal and interact with their like species instead. Another possibility is that the addition of each oligo changes the density of the liquid in such a way that the density difference between liquids increased, which aligns with the observed trends in Section 3.4. We also comment that the volume of liquid phase decreases with each addition of oligo. This is most likely due to loss of material when we pipette mix, as the liquid is quite viscous and tends to stick to the sides of the pipette tip.

While these experiments demonstrate the basic mechanism by which we would like to localize biomolecules, there are still many unanswered questions. How does the nanostar-tag structure affect the density of the liquid compared to the typical nanostar structure? The nanostar-tag structure has a higher molecular weight due to the addition of the extended arm and reporter strand, but also potentially occupies a larger volume. In addition, while captured oligos do not bind directly to sticky ends, does this double-stranded protrusion from the extended arm interfere with sticky end interactions? Do *et al.* found that at comparable concentrations to the liquid phase, their sticky end bound clients cause dissolution of the liquid droplets (Do et al., 2022). While our design does not rely on oligos binding to the sticky end, if sticky end interactions are inhibited, does that limit the amount of nanostar-tag structures that can form liquids? In other words, could we form liquid layers using only nanostar-tag structures? These questions can be answered by measuring the liquid phase concentration of various mixtures of typical nanostar and nanostar-tag structures via our capillary method. Understanding how tag domains affect

density would also inform us on how to achieve optimal layering quality. We could potentially tune densities by varying the amount of nanostar-tag structures in one liquid to increase density differences between two layers. In addition, a quantitative measurement of the fluorescent intensity of each layer after the addition of oligos would inform us of the yield of captured oligos in these liquids.

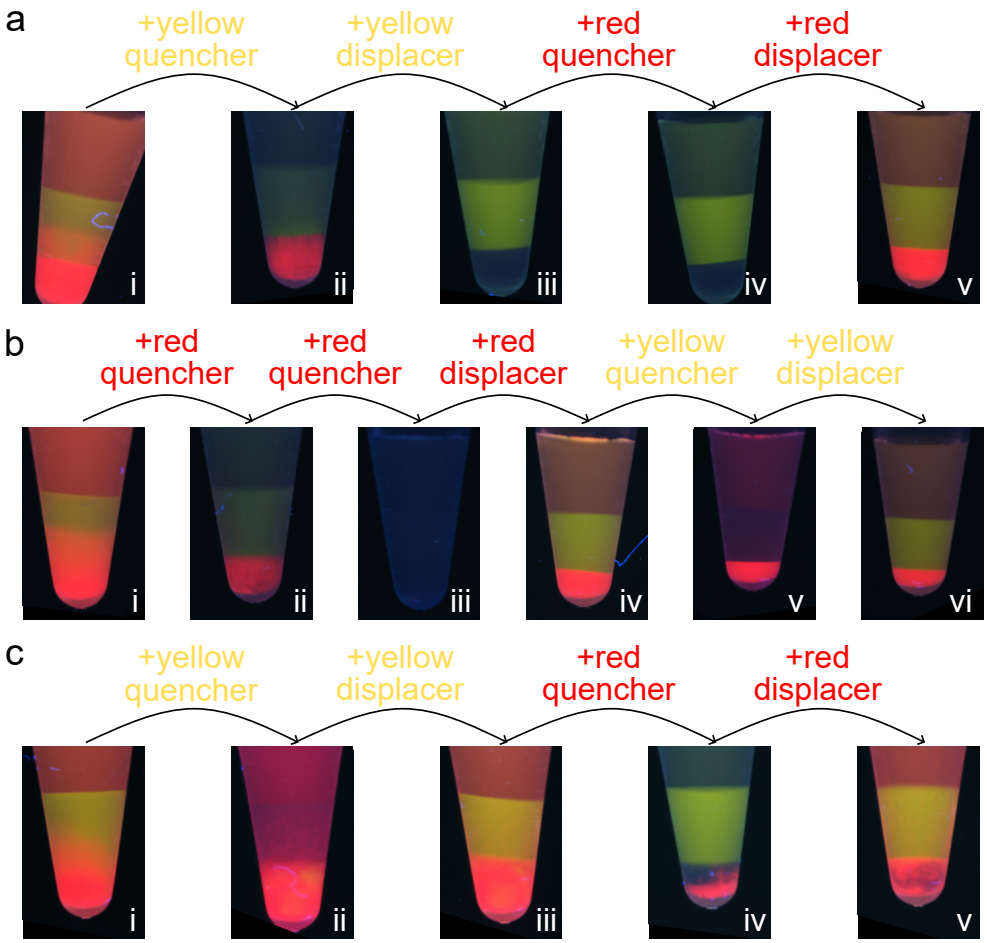

Figure 4.3: Localization of oligos via nanostar-tag structures with cover strand. Two layer system with each liquid composed of 2% nanostar-tag structures that had either a (a,b) single-stranded reporter or (c) a "covered" reporter. Yellow liquid nanostar is 4-ns25-6SE48-v1. Red liquid nanostar is 4-ns15-6SE36-v1. Strands were STD. (a,b) We observe that when reporters are single-stranded, spurious interactions can result in the unintentional quenching of an incorrect liquid (a-ii, a-iii, b-ii, b-iii). In b-iii, we attempted to completely quench the red liquid by adding more of the corresponding quencher, but found that it resulted in the complete quenching of yellow liquid as well. Addition of the red displacer in b-iv displaced the red quencher from both liquids. (c) When we annealed nanostar-tag structures with a cover strand and performed the sequential addition of oligos, the spurious interactions were inhibited and the correct sequence of fluorescent quenching and recovery was observed. In c-iv, the red liquid was not completely quenched after multiple rounds of vigorous pipetting and vortexing. The addition of cover strands potentially increased the viscosity of the liquid, which could slow the localization of oligos.

4.2 Localization and displacement of streptavidin

We next attempt localization of a green fluorescent streptavidin within a single liquid layer by modifying nanostars with a streptavidin-binding DNA aptamer. Previous studies have demonstrated successful partitioning of streptavidin into microscopic DNA droplets through a variety of binding moieties. Sato *et al*. capture streptavidin in DNA liquid droplets via biotinylated-DNA strands that have the same sticky end sequences as nanostars (Sato, Sakamto, and Takinoue, 2020). Dizani *et al*. recruit streptavidin into hybrid DNA-RNA condensates by attaching an RNA aptamer onto the nanostar structure (Dizani et al., 2024). Localization occurred on the order of hours in their experiments, as condensate formation and growth occurred simultaneously with recruitment of the protein.

We use the St-2-1 DNA aptamer sequence as reported in Bing *et al*. to recruit streptavidin into the liquid layers (Bing et al., 2010). Similar to the nanostar-tag structure in Section 4.1, we extend one arm of the nanostar and attach the aptamer onto this extension to form a nanostar-aptamer structure (Fig 4.4a). After localization of the protein into the liquid phase, we would like to release it back into the gas phase for downstream collection. To achieve this, we perform a kleptamer reaction (Lloyd et al., 2018) where we add a complementary displacer strand that can unfold the aptamer and therefore displace the protein.

We tested two protocols for localization of streptavidin. Our first method involves annealing a mixture of nanostars and nanostar-aptamer structures at low NaCl concentration (0.1 M). Nanostar-aptamer structures make up 25% of the mixture ($\sim$ 20 μM). After annealing, fluorescent streptavidin was gently mixed in at a final concentration of $\sim$ 3 μM and the NaCl concentration was increased to our usual concentration of 0.5 M. The sample was then incubated for 1 hr at room temperature before centrifugation. Based on our experiments in Section 4.1, we were concerned that annealing at our usual NaCl concentration of 0.5 M would result in viscous liquids that would significantly slow down localization kinetics. As we cannot vigorously mix the solution for fear of denaturing the protein, we attempted this low salt anneal to allow for formation of the nanostar and aptamer structures while reducing the viscosity of the liquid initially.

Our second method involved no annealing of the nanostar and aptamer strands beforehand. Instead, we mixed nanostar strands, the aptamer, and fluorescent streptavidin together at room temperature and directly added a final NaCl concentration of 0.5 M to the mixture. The concentrations of aptamer and streptavidin were iden-

tical to what was described in the first method. The sample was then incubated for 1 hr at room temperature before centrifugation. Formation of a liquid layer is still possible without annealing of nanostar strands (see Fig 3.2 for a previous example). As the initial mixture of aptamer strands and streptavidin is homogenous, these two molecules are spatially more accessible to each other for binding when salt is added and would hopefully increase yield of capture. In comparison, the low salt anneal method would require streptavidin to diffuse through viscous liquids in order to bind to an aptamer.

For each method, we made a corresponding control tube that consisted of regular nanostar structures only mixed with streptavidin (Fig 4.4b). As the nanostars do not have an aptamer, streptavidin should not localize within the liquid phase. This control is to ensure that localization of the protein is due to binding to the aptamer, and not due to spurious interactions with nanostar strands or centrifugal forces.

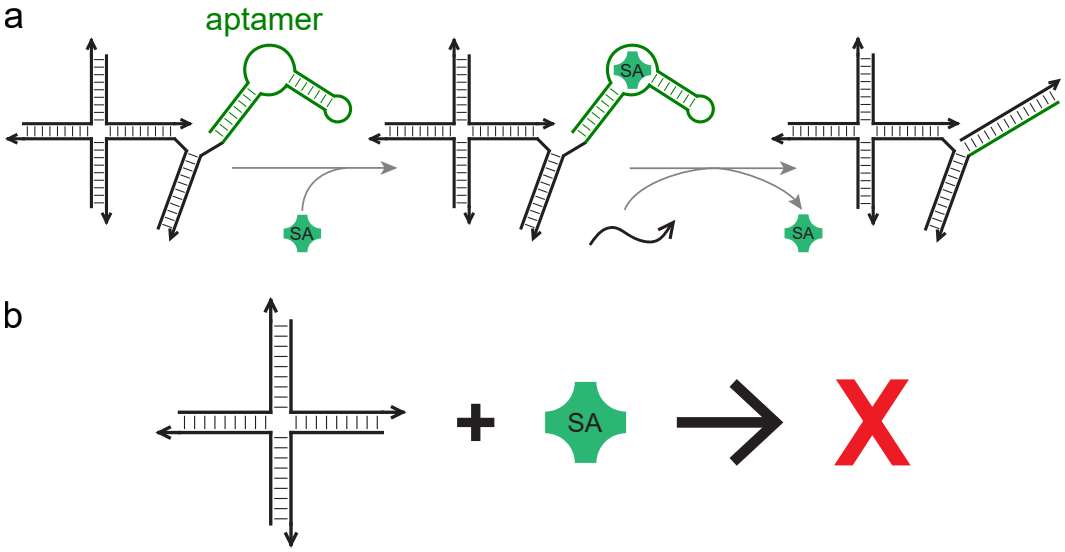

Figure 4.4: Nanostar-aptamer structure for capturing streptavidin. (a) One arm of the nanostar is extended to allow binding of the St-2-1 DNA aptamer (Bing et al., 2010) to form a nanostar-aptamer structure. (b) To release streptavidin from the liquid phase, we perform a kleptmaer reaction where we add a complementary displacer strand that can unfold the aptamer and therefore displace the protein. (c) Control tubes contain typical nanostar structures that do not have the aptamer attached and therefore will not interact with streptavidin.

Fig 4.5a shows the results of the low salt anneal method. Fig 4.5a-i show images of the control and sample tube taken on a UV transilluminator. We observe that the liquid phase of the control tube appears clear in color and that the majority of the green fluorescence is localized in the gas phase. This suggests that most of the

streptavidin remained in the gas phase and did not localize within the liquid layer. The sample tube, which contains the nanostar-aptamer liquid mixed with streptavidin (aptamer + SA), appears to have some fluorescence intensity in the liquid phase as well as in the gas phase. This suggests that some amount of streptavidin was localized, but not all of it. Given that there is almost five times the amount of aptamer compared to protein, we suspect that the kinetics of localization is hindered by the viscosity of the liquid and that with enough time, complete localization of all streptavidin could be achieved. After localization, we added the displacer strand to unfold the aptamer. We gently mixed the solution and allowed it to incubate for 1 hr at room temperature before centrifugation. We observe that the fluorescence of the liquid phase decreased after the addition of displacer, but not completely. We again attribute this to the viscosity of the liquid and that given enough time, complete displacement could also occur.

We provide a rough quantitative measure of the amount of protein captured and displaced by drawing a rectangular ROI in the gas phase of all tubes and measuring the mean gray value within that region (Fig 4.5a-ii; images taken on a gel scanner). We normalize the fluorescence intensity of the sample and displacer ROI to the control one. We plot these normalized values in the graph on the right. A lower gray value indicates higher recruitment of protein within the liquid phase. We observe that the fluorescence of the gas phase is ~50% less than that of the control when protein recruitment occurred. Addition of the displacer strand resulted in almost complete recovery of fluorescence. We note that there appears to be some amount of fluorescence in the liquid phase of the control when observing Fig 4.5a-ii. We suspect that some amount of nonspecific binding might be occurring between the liquid phase and streptavidin.

Fig 4.5b shows the results of the "no annealing" method. Similar to Fig 4.5a-i, we observe that the majority of fluorescence is localized in the gas phase in the control tube, while the sample tube containing nanostar-aptamer structures displays fluorescence in both liquid and gas phase. Again, this indicates incomplete localization of the protein. As strands were not annealed, it is possible that aptamers that did not properly bind to a nanostar strand are left in the gas phase, which would then hinder complete localization of the protein. However, we observe that the fluorescence of the liquid phase in the sample tube is brighter in this "no annealing" method compared to the one in the low salt anneal. This is also reflected in the measurement of the mean gray value of the gas phase (Fig 4.5b-ii). This suggests that

the spatial proximity of aptamer and streptavidin before phase separation of nanostars allowed for higher yield of capture. Addition of a displacer strand similarly results in reduced fluorescence in the liquid phase, but once again, not all protein is released. We note that the increase in fluorescence of the gas phase after addition of displacer is smaller in the "no annealing" method compared to the increase in the low salt anneal. This suggests that the liquid is more viscous in the "no annealing" method. As nanostars were not annealed and properly formed, the strands are perhaps highly entangled with each other, resulting in a material that is more viscous than a material with properly formed nanostars that can transiently interact with each other.

Many of the questions we posed at the end of Section 4.1 apply to these experiments here. We are similarly interested in understanding how the localization of streptavidin affects the density of the liquid. Instead of measuring the density as a function of various amounts of localized proteins, which could waste precious material, we could use DNA-coated nanoparticles as a substitute. The advantage of using nanoparticles allows us to control the size of the localized target, which reflects the range of protein sizes we could potentially capture in the future.

It is unclear whether the nonspecific binding of streptavidin to liquid phase in the control tubes is due to binding to nanostar strands or centrifugal force or a combination of both factors. Changing the nanostar sequence or changing the speed of centrifugation and measuring if the same amount of nonspecific binding occurs might provide some insight into which variable is the dominating factor. This would also require a more rigorous method of quantitatively measuring the yield of captured streptavidin. One possible method is to measure the absorbance of the gas phase at 280 nm on a spectrophotometer to determine how much target is leftover in the supernatant.

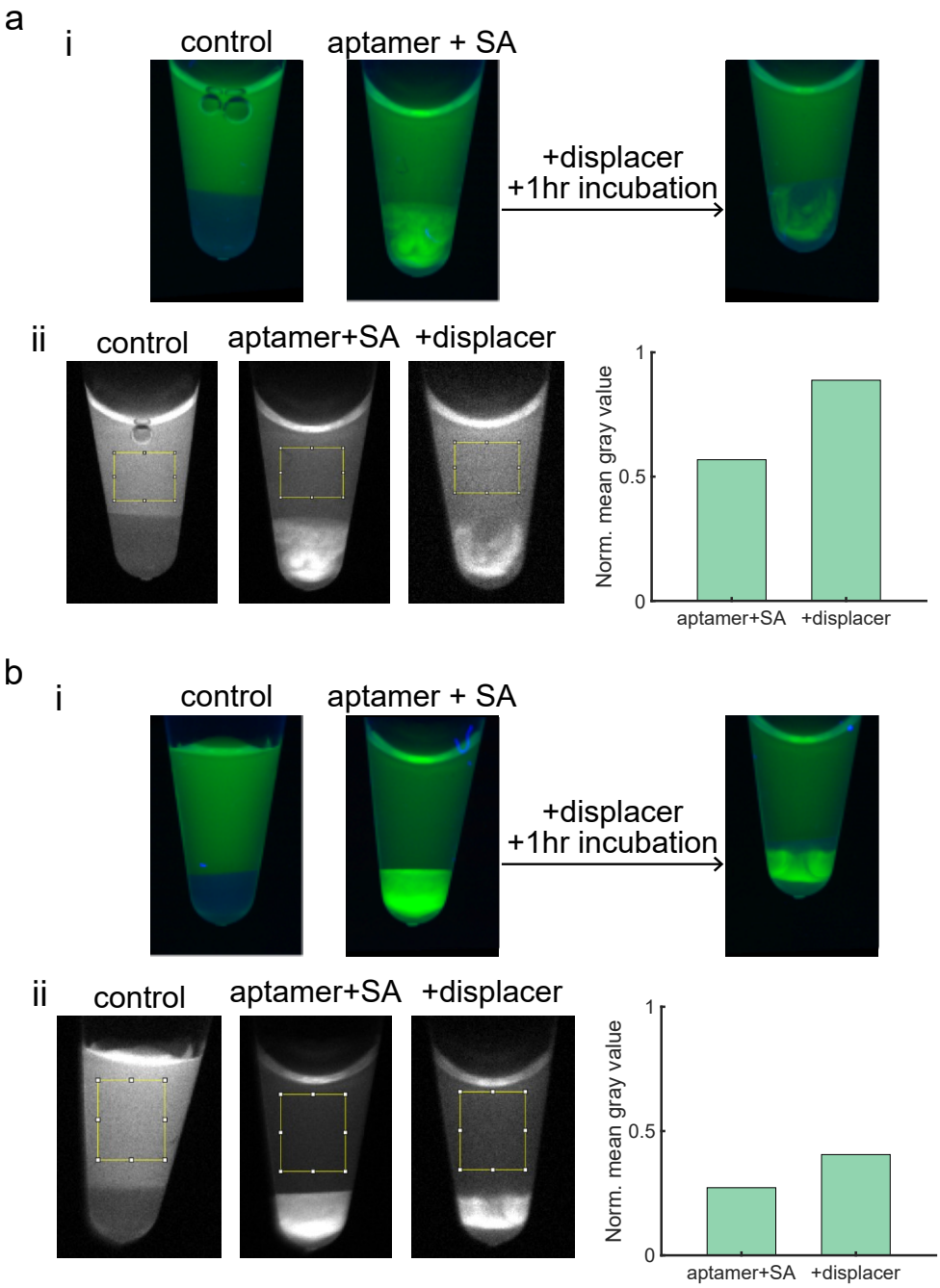

Figure 4.5: Localization and displacement of streptavidin. (a) Localization of fluorescent green streptavidin with nanostars annealed in low NaCl concentrations. (a-i) are images of the tubes taken on a UV transilluminator. (a-ii) are images of the same tubes taken on a gel scanner. We draw rectangular ROI in each of the three tubes and measure the mean gray value of that area. We normalize the sample and displacer ROI to the control to obtain a rough measure of the yield of captured streptavidin, which is plotted in the graph on the right. (b) Localization of fluorescent green streptavidin with nanostars that were not annealed. (b-i) are images of the tubes taken on a UV transilluminator. (b-ii) are images of the same tubes taken on a gel scanner. The same quantitative analysis was performed on these images. We observe that the "no annealing" samples had a higher yield of capture compared to nanostars annealed in a low salt concentration.

4.3 Considerations for other proteins and real-world applications

These rudimentary experiments provide insight into the realities of translating these liquids into a practical tool for separation. In Section 4.1, we were able to achieve localization of oligos on the order of minutes by thoroughly mixing solutions at room temperatures and at an NaCl concentration of 0.5 M. In comparison, Nguyen *et al*. required incubation on the order of hours at room temperature to achieve localization of DNA linkers, albeit at a higher NaCl concentration of 1 M. Do *et al*. demonstrated successful localization on the order of minutes by decreasing the salt concentration (350 mM) and increasing the temperature to 30°C. The ability to mix condensates to increase localization kinetics, especially at room temperature and high NaCl concentrations, is an advantage of macroscopic liquids.

While the use of a mechanical force to increase the kinetics of localization is viable for targets like nucleic acids, this would be detrimental to fragile proteins as they would denature under such force. In addition, proteins typically require cold environments to prevent denaturation. Low temperatures, however, would cause liquids to become even more viscous and decrease the kinetics of localization. Decreasing the salt concentration would decrease the viscosity but potentially result in weak binding between the target and the binding moiety. Perhaps a more realistic protocol would be a two-step one, where proteins are first mixed with aptamers at low temperatures followed by addition of nanostars that bind to the aptamer and localize protein-bound aptamers within liquids. The slow localization kinetics is potentially an unavoidable limitation. Given that traditional protein purification techniques usually requires multiple steps that can take on the order of hours or days, the simplicity of just a two-step process—even with slow kinetics that takes hours—might be good practical tradeoff.

Surprisingly, these experiments also indicate that the need for a layering structure can be unnecessary depending on the application. Partitioning and collection of the target can still take place whether optimal layer formation occurs or not, as indicated by the results of Fig 4.3. If the goal is to just separate proteins, we could potentially relax the design requirements to achieve layers and work at low temperature settings. The need for layer formation is most useful in applications regarding detection. For example, if one desires to detect multiple analytes in a solution, specific localization of each target to a unique layer would be important to visualize which analytes are present. An interesting research direction would be to integrate these macroscopic liquids with the ROSALIND detection system designed

by Jung *et al*. (Jung, Alam, et al., 2020). ROSALIND, which stands for RNA Output Sensors Activated by Ligand Induction, is a cell-free in vitro transcription system that detects contaminants in water. When a contaminant of interest is detected, transcription of a fluorogenic RNA aptamer occurs. Currently, multiplex detection of analytes can occur through a series of logic gates (Jung, Archuleta, et al., 2022). However, we believe we can provide a simpler method for detection of multiple analytes. For each analyte detected, a unique fluorogenic aptamer can be transcribed which can then be localized into a unique liquid layer. As the reporting molecule is a nucleic acid, this system would be robust to the mixing needed to increase localization kinetics.

We demonstrated one case of using DNA aptamers to localize a simple protein. Expansion to more high value proteins is possible by sourcing current aptamers in the literature for various targets such as BSA and blood-clotting factors (Wang et al., 2019; Forier et al., 2017), which are common protein therapeutics. If no aptamer sequences currently exist for a particular protein target, we could modify proteins with a His-tag and localize proteins via His-tag aptamers (Bartnicki et al., 2015). We remark that doing so would limit the number of proteins one could separate in a single step if there are multiple his-tagged proteins present.

The yield and purity of captured targets most likely depends on the particular aptamer used. Aptamers are usually reported with a certain dissociation constant (K_D), with lower K_D indicating better binding affinity between aptamer and target. However, under different conditions, the K_D can change, and aptamers can perform worse than initially reported, both in yield and in specificity (McKeague et al., 2015). In the crowded environment of a condensate, the performance of aptamers can certainly differ from what is reported in literature, so careful selection and analysis of aptamers is necessary to optimize aptamer-modified liquids for localization.

A limitation of using DNA condensates to localize proteins is non-specific binding with certain positively charged proteins, as DNA is negatively charged. Of course, depending on the protein, one could change the pH of the solution such that the protein of interest is neutrally charged, as long as it is within a viable pH range for DNA.

Chapter 5

CONCLUSIONS

The work presented here acts as a foundation for a potentially exciting and novel protein separation method. While I did not get the chance to fully explore the separation aspect of this project, I have learned many fundamental principles about DNA liquids, DNA synthesis, and DNA nanotechnology that were thought provoking, sometimes exasperating, and always exciting.

In developing our capillary-based method for liquid phase concentration measurements, we discovered that benzamide contamination of STD strands can significantly affect our measurements and the appearance of our layers. In addition, the amount of benzamide can vary from sample to sample, making measurements difficult to reproduce[1]. Removal of benzamide via ethanol precipitation helps to improve the quantification accuracy and the appearance of layers, but does not completely remove sample variability. I highly encourage other scientists to carefully consider the impact of contamination leftover from oligo synthesis within their work, especially in cases where purification of STD strands is not possible.

Our goal is to engineer DNA nanostars to form macroscopic DNA liquids that can separate multiple biomolecular targets. One of the key features of this idea is the formation of multiple layers to allow for multiplexed separation. Formation of multilayer DNA liquids requires programmable control of the layering order and layering quality. The layering order is determined by the density of the liquid, which in turn is determined by the geometry of the nanostar. We found that the layering quality is determined by a combination of density differences between liquids and the sticky end orthogonality of nanostars. The tradeoff between the number of attainable layers and sticky end orthogonality provides a practical flexibility for users depending on their application. For now, we were able to create up to five immiscible liquid layers, but we believe that careful design of nanostars to achieve more liquid layers with smaller density differences is certainly possible.

How realistic is our goal to develop macroscopic DNA liquids as a protein separation

[1] This was the most exasperating portion of my research. I truly believe that it would be in the best interest—both financially and practically—of the DNA molecular programming groups at Caltech to invest in some oligo synthesizer so that future researchers in the lab can reliably and reproducibly synthesize their strands in-house.

tool? The cost-effectiveness of liquids for separation has yet to be determined. In terms of manufacturing cost, we estimate in the range of $100-$300 per mL of DNA liquid phase using STD strands from IDT. For comparison, resins for affinity chromatography cost on the order of $10 per mL. The upfront costs of synthesis is far more expensive for DNA liquids, but this does not denote that the overall cost-effectiveness of liquids is worse than traditional separation techniques. DNA origami nanostructures as a drug-delivery system to target cancer has been shown to potentially be more cost-effective than current delivery systems if one accounts for the type and amount of drugs, number of treatments needed, and various other factors (Coleridge and Dunn, 2020). We believe that the same could be applied to DNA liquids as a separation tool if we factored in the cost of the entire procedure. As to what this procedure looks like, further exploration and innovative designs are needed to potentially make liquids more cost-effective tool.

The study of condensates is an incredibly rich and exciting area right now, and the explosion of publications in recent years on new condensates discovered or engineering of condensates for novel uses highlights this excitement. Many investigations focus on condensates on the microscopic scale, which makes practical sense as most of these studies are on protein-based condensates, and it is difficult to scale up with proteins. I hope that this work and our ability to scale up to macroscopic sizes with DNA condensates inspires others to explore what else can be done besides just studying condensates under the microscope. We highlighted one potential avenue of exploration in Chapter 4, where we discussed integrating the ROSALIND detection system with macroscopic liquids. There are many other potential ideas that can be explored with macroscopic liquids, and I hope that this body of work can act as a catalyst to trigger that exploration.

On a philosophical note, there is a certain beauty in the fact that I can make small changes to nanostars— nanoscale molecules that are not visible to the eyes without special equipment— and that these small changes can have such powerful and drastic effects on DNA liquids— something that I can see with just my naked eyes. It parallels what occurs in science. Every study or paper contributes a small change in our understanding of the world, and these small changes add up to large impacts on our scientific knowledge. So too do I hope that the small contribution of this work does in advancing the fields of DNA nanotechnology and DNA liquids. And if enough small changes occur, the field could produce something more beautiful and colorful than a rainbow.

BIBLIOGRAPHY

Addison, Christopher J. et al. (2011). "Residual benzamide contamination in synthetic oligonucleotides observed using UV resonance Raman spectroscopy". In: *Journal of Raman Spectroscopy* 42.3, pp. 349–354. DOI: https://doi.org/10.1002/jrs.2715.

Agarwal, Siddharth, Dino Osmanovic, Mahdi Dizani, et al. (2024). "Dynamic control of DNA condensation". In: *Nature Communications* 15 (1).

Agarwal, Siddharth, Dino Osmanovic, Melissa A. Klocke, et al. (2022). "The Growth Rate of DNA Condensate Droplets Increases with the Size of Participating Subunits". In: *ACS Nano* 16 (8), pp. 11842–11851. DOI: 10.1021/acsnano.2c00084.

Alberti, S., A. Gladfelter, and T. Mittag (2019). "Considerations and Challenges in Studying Liquid-Liquid Phase Separation and Biomolecular Condensates". In: *Cell* 176.3, pp. 419–434. DOI: https://doi.org/10.1016/j.cell.2018.12.035.

Alberti, S. and A. A. Hyman (2021). "Biomolecular condensates at the nexus of cellular stress, protein aggregation disease and ageing". In: *Nature Reviews Molecular Cell Biology* 22, pp. 196–213. DOI: https://doi.org/10.1038/s41580-020-00326-6.

Bartnicki, F. et al. (2015). "Imidazole-free purification of His3-tagged recombinant proteins using ssDNA aptamer-based affinity chromatography". In: *J. Chromatogr. A* 1418, pp. 130–139.

Biffi, S. et al. (2013). "Phase behavior and critical activated dynamics of limited-valence DNA nanostars". In: *PNAS* 110.39, pp. 15633–15637. DOI: https://doi.org/10.1073/pnas.1304632110.

Bing, T. et al. (2010). "Conservative secondary structure motif of streptavidin-binding aptamers generated by different laboratories". In: *Bioorg Med Chem.* 18, pp. 1798–1805. DOI: doi:10.1016/j.bmc.2010.01.054.

Brangwynne, Clifford P. et al. (2009). "Germline P Granules Are Liquid Droplets That Localize by Controlled Dissolution/Condensation". In: *Science* 324.5935, pp. 1729–1732. DOI: 10.1126/science.1172046. eprint: https://www.science.org/doi/pdf/10.1126/science.1172046. URL: https://www.science.org/doi/abs/10.1126/science.1172046.

Burnouf, Thierry (2007). "Modern Plasma Fractionation". In: *Transfusion Medicine Reviews* 21.2, pp. 101–117. ISSN: 0887-7963. DOI: https://doi.org/10.1016/j.tmrv.2006.11.001.

Coleridge, Edward L. and Katherine E. Dunn (2020). "Assessing the cost-effectiveness of DNA origami nanostructures for targeted delivery of anti-cancer drugs to tumours". In: *Biomed Phys Eng Express* 6, p. 065030.

Conrad, N. et al. (2019). "Increasing valence pushes DNA nanostar networks to the isostatic point". In: *PNAS* 116 (15), pp. 7238–7243.

Conrad, Nathaniel et al. (Dec. 2022). "Emulsion imaging of a DNA nanostar condensate phase diagram reveals valence and electrostatic effects". In: *The Journal of Chemical Physics* 157.23, p. 234203. ISSN: 0021-9606. DOI: 10.1063/5.0130808. eprint: https://pubs.aip.org/aip/jcp/article-pdf/doi/10.1063/5.0130808/16556555/234203_1_online.pdf. URL: https://doi.org/10.1063/5.0130808.

Decker, John S. et al. (2024). "Phase separation methods for protein purification: A meta-analysis of purification performance and cost-effectiveness". In: *Biotechnology Journal* 19.4, p. 2400005. DOI: https://doi.org/10.1002/biot.202400005.

Dizani, Mahdi et al. (2024). "Protein Recruitment to Dynamic DNA-RNA Host Condensates". In: *Journal of the American Chemical Society* 146 (43), pp. 29344–29354. DOI: 10.1021/jacs.4c07555.

Do, Sungho et al. (2022). "Engineering DNA-based synthetic condensates with programmable material properties, compositions, and functionalities". In: *Science Advances* 8.41, eabj1771. DOI: 10.1126/sciadv.abj1771.

dos Santos, Raquel, Ana Luísa Carvalho, and A. Cecília A. Roque (2017). "Renaissance of protein crystallization and precipitation in biopharmaceuticals purification". In: *Biotechnology Advances* 35.1, pp. 41–50. ISSN: 0734-9750. DOI: https://doi.org/10.1016/j.biotechadv.2016.11.005.

Du, Miao et al. (2022). "1Progress, applications, challenges and prospects of protein purification technology". In: *Frontiers in Bioengineering and Biotechnology* 10. DOI: 10.3389/fbioe.2022.1028691.

Dzuricky, M. et al. (2020). "De novo engineering of intracellular condensates using artificial disordered proteins". In: *Nature Chemistry* 12, pp. 814–825. DOI: https://doi.org/10.1038/s41557-020-0511-7.

Evans, Constantine G. and Erik Winfree (2017). "Physical principles for DNA tile self-assembly". In: *Chem. Soc. Rev.* 46 (12), pp. 3808–3829. DOI: 10.1039/C6CS00745G.

Feric, M. et al. (2016). "Coexisting Liquid Phases Underlie Nucleolar Subcompartments". In: *Cell* 165, pp. 1686–1697.

Forier, Cynthia et al. (2017). "DNA aptamer affinity ligands for highly selective purification of human plasma-related proteins from multiple sources". In: *Journal of Chromatography A* 1489, pp. 39–50.

Gong, Jing et al. (2022). "Computational DNA Droplets Recognizing miRNA Sequence Inputs Based on Liquid–Liquid Phase Separation". In: *Advanced Functional Materials* 32.37, p. 2202322. DOI: https://doi.org/10.1002/adfm.202202322.

Hegde, Omkar et al. (May 2024). "Competition between Self-Assembly and Phase Separation Governs High-Temperature Condensation of a DNA Liquid". In: *Phys. Rev. Lett.* 132 (20), p. 208401. DOI: 10.1103/PhysRevLett.132.208401. URL: https://link.aps.org/doi/10.1103/PhysRevLett.132.208401.

Huguet, J.M. et al. (2010). "Single-molecule derivation of salt dependent base-pair free energies in DNA". In: *PNAS* 107, pp. 15431–15436.

Jeon, B., D. T. Nguyen, G. R. Abraham, et al. (2018). "Salt-dependent properties of a coacervate-like, self-assembled DNA liquid". In: *Soft Matter* 14, pp. 7009–7015. DOI: https://doi.org/10.1039/c8sm01085d.

Jeon, B., D. T. Nguyen, and O. A. Saleh (2020). "Sequence-Controlled Adhesion and Microemulsification in a Two-Phase System of DNA Liquid Droplets". In: *J. Phys. Chem. B* 124.40, pp. 8888–8895. DOI: https://doi.org/10.1021/acs.jpcb.0c06911.

Jung, Jaeyoung K., Khalid K. Alam, et al. (2020). "Cell-free biosensors for rapid detection of water contaminants". In: *Nature Biotechnology* 38, pp. 1451–1459.

Jung, Jaeyoung K., Chloé M. Archuleta, et al. (2022). "Programming cell-free biosensors with DNA strand displacement circuits". In: *Nature Chemical Biology* 18, pp. 385–393.

Ke, Yonggang et al. (2012). "Three-Dimensional Structures Self-Assembled from DNA Bricks". In: *Science* 338.6111, pp. 1177–1183. DOI: 10.1126/science.1227268.

Kengmana, E. et al. (2024). "Spatial Control over Reactions via Localized Transcription within Membraneless DNA Nanostar Droplets". In: *J. Am. Chem.* 146, pp. 32942–32952.

Lee, Taehyun et al. (2021). "The flexibility-based modulation of DNA nanostar phase separation". In: *Nanoscale* 13 (41), pp. 17638–17647. DOI: 10.1039/D1NR03495B.

Li, Pilong et al. (2012). "Phase transitions in the assembly of multivalent signalling proteins". In: *Nature* 483, pp. 336–340.

Lloyd, Jonathan et al. (2018). "Dynamic Control of Aptamer–Ligand Activity Using Strand Displacement Reactions". In: *ACS Synth. Biol.* 7.

Locatelli, Emanuele et al. (2017). "Condensation and Demixing in Solutions of DNA Nanostars and Their Mixtures". In: *ACS Nano* 11.2, pp. 2094–2102.

Lyon, A. S., W. B. Peeples, and M. K. Rosen (2021). "A framework for understanding the functions of biomolecular condensates across scales". In: *Nature Reviews Molecular Cell Biology* 22.3, pp. 215–235. DOI: https://doi.org/10.1038/s41580-020-00303-z.

McKeague, Maureen et al. (2015). "Comprehensive Analytical Comparison of Strategies Used for Small Molecule Aptamer Evaluation". In: *Analytical Chemistry* 87, pp. 8608–8612.

Nguyen, D. T. et al. (2019). "Length-Dependence and Spatial Structure of DNA Partitioning into a DNA Liquid". In: *Langmuir* 35, pp. 14849–14854. DOI: https://doi.org/10.1021/acs.langmuir.9b02098.

Nguyen, Dan T. and Omar A. Saleh (2017). "Tuning phase and aging of DNA hydrogels through molecular design". In: *Soft Matter* 13 (32), pp. 5421–5427. DOI: 10.1039/C7SM00557A.

Ouyang, Jinbo et al. (2019). "Solubility determination and modelling of benzamide in organic solvents at temperatures from 283.15K and 323.15K, and ternary phase diagrams of benzamide-benzoic acid cocrystals in ethanol at 298.15K". In: *Journal of Molecular Liquids* 286, p. 110885. ISSN: 0167-7322. DOI: https://doi.org/10.1016/j.molliq.2019.110885.

Patel, Avinash et al. (2015). "A Liquid-to-Solid Phase Transition of the ALS Protein FUS Accelerated by Disease Mutation". In: *Cell* 162, pp. 1066–1077.

Perret, G. and E. Boschetti (2017). "Aptamer affinity ligands in protein chromatography". In: *Biochimie* 145, pp. 98–112.

Perret, Gérald and Egisto Boschetti (2018). "Aptamer affinity ligands in protein chromatography". In: *Biochimie* 145. Aptamer Technology and Applications, pp. 98–112. ISSN: 0300-9084. DOI: https://doi.org/10.1016/j.biochi.2017.10.008. URL: https://www.sciencedirect.com/science/article/pii/S0300908417302602.

Qian, Lulu and Erik Winfree (2011). "Scaling Up Digital Circuit Computation with DNA Strand Displacement Cascades". In: *Science* 332.6034, pp. 1196–1201. DOI: 10.1126/science.1200520.

Rodriguez, Elliott L. et al. (2020). "Affinity chromatography: A review of trends and developments over the past 50 years". In: *Journal of Chromatography B* 1157, p. 122332. ISSN: 1570-0232. DOI: https://doi.org/10.1016/j.jchromb.2020.122332. URL: https://www.sciencedirect.com/science/article/pii/S1570023220309703.

Rothemund, P. W. K. (2006). "Folding DNA to create nanoscale shapes and patterns". In: *Nature* 440, pp. 297–302. DOI: https://doi.org/10.1038/nature04586.

Rovigatti, Lorenzo, Francesca Bomboi, and Francesco Sciortino (2014). "Accurate phase diagram of tetravalent DNA nanostars". In: *The Journal of Chemical Physics* 140.15, p. 154903.

Rovigatti, Lorenzo, Frank Smallenburg, and Flavio Romano (2014). “Gels of DNA Nanostars Never Crystallize”. In: *ACS Nano* 8 (4), pp. 3567–3574.

Sato, Y., T. Sakamto, and M. Takinoue (2020). “Sequence-based engineering of dynamic functions of micrometer-sized DNA droplets”. In: *Science Advances* 6.23, eaba3471. DOI: https://doi.org/10.1126/sciadv.aba3471.

Simon, J. R. et al. (2019). “Engineered Ribonucleoprotein Granules Inhibit Translation in Protocells”. In: *Molecular Cell* 75, pp. 66–75. DOI: https://doi.org/10.1016/j.molcel.2019.05.010.

Skipper, Karuna and Shelley F.J. Wickham (2024). “Core-shell coacervates formed from DNA nanostars”. In: *ChemRxiv*. DOI: 10.26434/chemrxiv-2024-07pvd.

Valentin, Gabriel (1837). *Repertorium für anatomie und physiologie*.

Wagner, Rudolph (1835). “Einige bemerkungen und fragen über das keimbläschen (vesicular germinativa)”. In: *Müller’s Archiv Anat Physiol Wissenschaft Med* 268.1835, pp. 373–7.

Wang, C. et al. (2019). “Label- and modification-free-based in situ selection of bovine serum albumin specific aptamer”. In: *Journal of Separation Science* 42, pp. 3571–3578.

Xu, Zhengyu et al. (2023). “Liquid-liquid phase separation: Fundamental physical principles, biological implications, and applications in supramolecular materials engineering”. In: *Supramolecular Materials* 2, p. 100049. ISSN: 2667-2405. DOI: https://doi.org/10.1016/j.supmat.2023.100049.

Appendix A

DERIVATION OF RELATIONSHIP BETWEEN LIQUID PHASE DENSITY AND CONCENTRATION

We derive here the relationship between liquid phase density and concentration. The liquid phase is composed of DNA and the aqueous buffer or solvent it is resuspended in. The density of the liquid phase can therefore be written as

$$\rho_{liq} = \frac{m_{DNA} + m_{sol}}{V_{liq}}$$

where m_{DNA} and m_{sol} are the mass of DNA and solvent, respectively, and V_{liq} is the volume of liquid phase.

We can rewrite m_{DNA} in terms of the concentration of DNA in the liquid phase (C_{liq}) and m_{sol} in terms of the solvent density:

$$m_{DNA} = C_{liq} V_{liq}$$
$$m_{sol} = \rho_{sol} V_{sol}$$

where ρ_{sol} and V_{sol} are the density and volume of solvent, respectively. Note that C_{liq} is in units of mass concentration, i.e., mg/mL.

The volume of liquid phase is equal to the sum of the volumes of solvent and DNA. We can therefore rewrite the mass of solvent in the following way:

$$m_{sol} = \rho_{sol} \left(1 - \frac{V_{DNA}}{V_{liq}}\right) V_{liq}$$

The term V_{DNA}/V_{liq} is the volume fraction of DNA inside the liquid phase. We can rewrite this in terms of the concentration of DNA in the liquid phase and the density of DNA:

$$\frac{V_{DNA}}{V_{liq}} = \frac{m_{DNA}}{V_{liq}} \frac{V_{DNA}}{m_{DNA}} = \frac{C_{liq}}{\rho_{DNA}}$$

We can now rewrite the liquid phase density in terms of the densities of DNA and solvent, which are known numbers, and the concentration of DNA in liquid phase, which we can measure via UV spectrophotometer:

$$\rho_{liq} = \frac{C_{liq}V_{liq} + \rho_{sol}\left(1 - \frac{C_{liq}}{\rho_{DNA}}\right)V_{liq}}{V_{liq}}$$

$$\therefore \rho_{liq} = C_{liq} + \rho_{sol}\left(1 - \frac{C_{liq}}{\rho_{DNA}}\right)$$

Appendix B

EFFECT OF HIGH TEMPERATURE SPINS

Nanostars that form viscous liquids can stick to the sides of the capillary. When this happens, the volume fraction measurement is underestimated since not all of the liquid phase sediments to the bottom of the capillary. To address this problem, we spin such samples at higher temperatures so that the liquid phase becomes less viscous and can flow more easily to the bottom of the capillary. After a high temperature spin, we let the capillary sit and come back to room temperature for about 15 minutes before continuing with imaging and measurement of concentration. We believed that this was a sufficient amount of time as the capillaries were thin (outer diameter < 1.5 mm). However, we observe that there is a marginal, but systematic increase in gas phase concentration as spin temperature increases (blue bars in Fig B.1). We were concerned that this was an indication that the system had not cooled down sufficiently by the time of measurement. We tested adding a third spin in the swinging bucket rotor at 20°C, which is the temperature that we typically spin samples at if they are not viscous, to see if that would eliminate this systematic increase. The orange bars in Fig B.1 show that the gas phase concentration still increases with spin temperature despite this extra cooling spin. We hypothesize that perhaps the system is not quite at equilibrium yet with room temperature by the time of measurement. The increase in gas phase concentrations is marginal, and we did not observe any severe effects on the calculated liquid phase concentration. We therefore opted to not include this third cooling spin in our typical protocol.

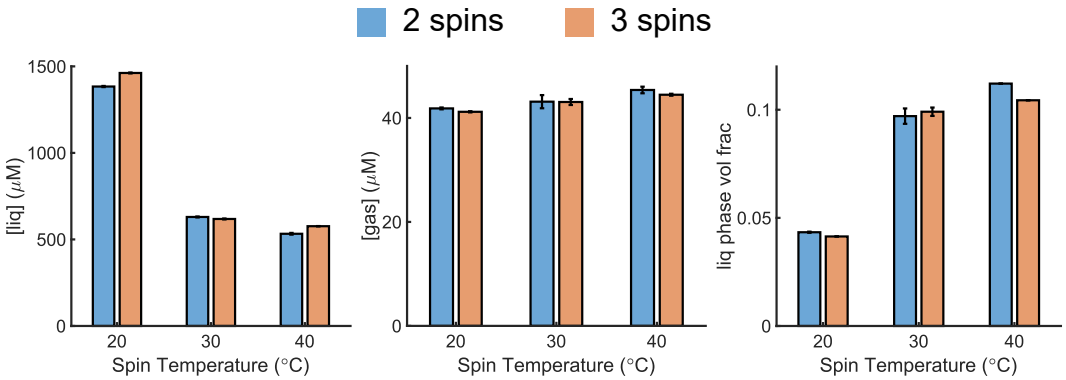

Figure B.1: Measurements of the liquid phase concentration (*left*), gas phase concentration (*center*), and liquid phase volume fraction (*right*) for samples that underwent the typical two spins (blue bars) at the spin temperature listed on the x-axis and an extra cooling third spin at 20°C (orange bars). Under both spin conditions, we see a marginal but systematic increase in the gas phase concentration as the spin temperature increases.

Appendix C

ESTIMATION OF BENZAMIDE CONCENTRATION IN IDT STOCK TUBES

We estimate the amount of benzamide in a single IDT stock tube by measuring the absorbance spectrum of a single STD strand and subtracting the spectrum of the same strand after ethanol precipitation (Fig C.1c). Comparison of this difference spectrum with the spectra of benzamide solutions at various concentrations (Fig C.1d) suggests that the amount of benzamide is between 1 mM to 5 mM. Given that the the absorbance spectrum in Fig C.1c qualitatively matches the spectrum of the 1 mM sample in Fig C.1d but is almost double in absorbance value, we estimate that the amount of benzamide is ~2 mM. As the original STD strand was diluted by a factor of 17 from the stock tube to measure the spectrum shown in Fig C.1a, we estimate that the amount of benzamide in the original stock tube is ~30 mM.

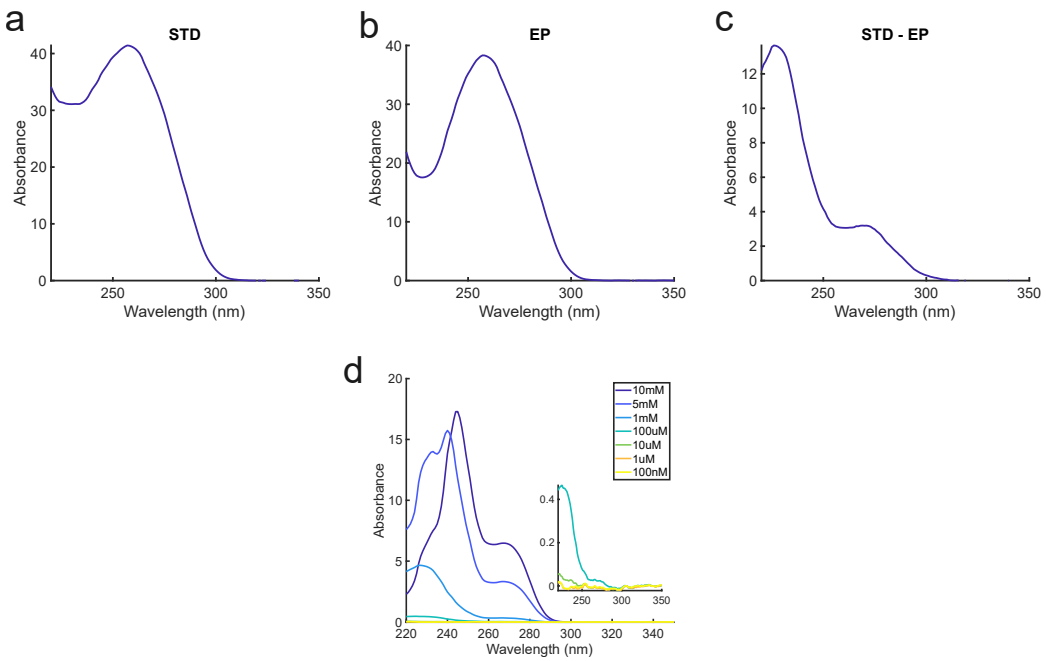

Figure C.1: (a) Absorbance spectrum of a single STD strand ordered from IDT at a concentration of 100 μM. (b) Absorbance spectrum of the STD strand shown in (a) after ethanol precipitation. Note the drop in absorbance around 230 nm, indicating successful removal of benzamide. (c) Subtraction of the EP spectrum in (b) from the STD spectrum in (a) results in the shown difference spectrum. We compare this difference spectrum with the spectra of benzamide solutions at various concentrations in (d) to estimate the amount of benzamide in the original stock tube. (d) Spectra of various benzamide concentrations ranging from 100 nM to 10 mM. Interestingly, the spectrum exhibits a red shift at a concentration of 5 mM and above. We suspect that at high concentrations, benzamide forms dimers **??**, which could result in the observed shift.

Appendix D

ESTIMATION OF LIQUID PHASE CONCENTRATION ERROR

The effect of benzamide on the total concentration should be negligible, as comparison of the spectra of single STD strands in Fig 2.3c with the various benzamide spectra in Fig 2.4a suggests that the ratio of benzamide to DNA in our initial stock tubes is at most 10:1, which is not within the regime where benzamide adversely affects DNA quantification. We therefore assume that the total concentration is essentially equal to our intended amount of 100 μM.

Volume fractions could potentially be affected by hydrogen binding of benzamide to the nucleotides, but we hypothesize that most of the benzamide is expelled into the gas phase as indicated by Fig 2.3a and b. We therefore assume that the measured liquid phase volume fraction is not impeded by the presence of benzamide.

Given these assumptions, the error in liquid phase concentration calculations mainly comes from the error in the measured gas phase concentration due to the presence of benzamide. In our experiments, gas phase concentrations range from 10 μM to 75 μM. On average, the liquid phase volume fraction is 0.15. If the overestimation of gas phase concentration due to benzamide is 20%, which is what we estimate to be the greatest margin of error, then the percent error between the true liquid phase concentration and the underestimated one is

$$C_{liq}^{under} = \frac{100\mu M - 75\mu M \cdot 0.85}{0.15} = 242\mu M$$

$$C_{liq}^{true} = \frac{100\mu M - 0.8 \cdot 75\mu M \cdot 0.85}{0.15} = 327\mu M$$

$$\% \text{ error} = \left|\frac{242 - 327}{327}\right| \times 100 = 26\%$$

Appendix E

COMPARISON OF IDT AND THERMOFISHER STRANDS

We were curious to see if oligos from other manufacturers besides IDT also suffered from excess contaminants. We therefore ordered STD strands from ThermoFisher and compared usage of these strands in our experiments with the same sequences ordered STD from IDT. We also ordered HPLC purified strands of the same sequences from IDT to use as a baseline for the purest strands that we could obtain. The two nanostars used in these experiments were 4-ns20-6SE43-v1 and 4-ns20-6SE31-v1.

Fig E.1a shows the absorbance spectra of STD (light blue lines) and HPLC (dark blue lines) strands from IDT and ThermoFisher STD strands (magenta lines). We observed that the absorbance at 230 nm is lower in all ThermoFisher strands compared to the same STD strands from IDT. This at the very least suggests low or zero presence of benzamide in ThermoFisher STD strands. Interestingly though, when we filled capillaries with solutions of these nanostars, we noticed a stark difference in the volume fraction between ThermoFisher and both types of IDT strands. The volume fraction of the ThermoFisher samples was always larger than their IDT counterparts (Fig E.1b). In fact, the ThermoFisher samples required longer spin times than IDT samples to show visible phase separation in the capillaries. Although the absorbance spectra of the gas phases for the ThermoFisher samples do not seem to suggest the presence of any contaminants (unless there are contaminants that absorb strongly at 260 nm) (Fig E.1c), there are clearly some unknown factors that cause the ThermoFisher samples to behave differently from their IDT counterparts. Since the volume fraction of the ThermoFisher samples is significantly larger than the IDT ones, the calculated liquid phase concentration of ThermoFisher nanostars was always lower than IDT nanostars (Fig E.1d), which is to be expected. The most confounding result, however, is that the relative ordering of the liquid phase concentrations of the two nanostars flip when comparing between IDT and ThermoFisher samples. As such, the pairwise liquids formed in tubes reflect this difference in ordering when using IDT versus ThermoFisher strands (Fig E.1e).

While ThermoFisher STD strands appear to have the boon of zero to low amounts of benzamide, it is clear that there is something else present (or maybe not present) that causes nanostars formed from them to behave very differently from the ones formed

from IDT products. In fact, since the order of liquids formed from STD IDT strands aligns with the ordering of those formed from IDT HPLC strands, which has the highest purity of DNA out of the samples tested, it is tempting to conclude that the ordering of the ThermoFisher liquids is "inaccurate." However, the best conclusion we can draw from this experiment is that the same stock of strands used in measuring liquid phase concentrations must be the same ones used to form macroscopic liquids in order for measured values to align with what we observe visually.

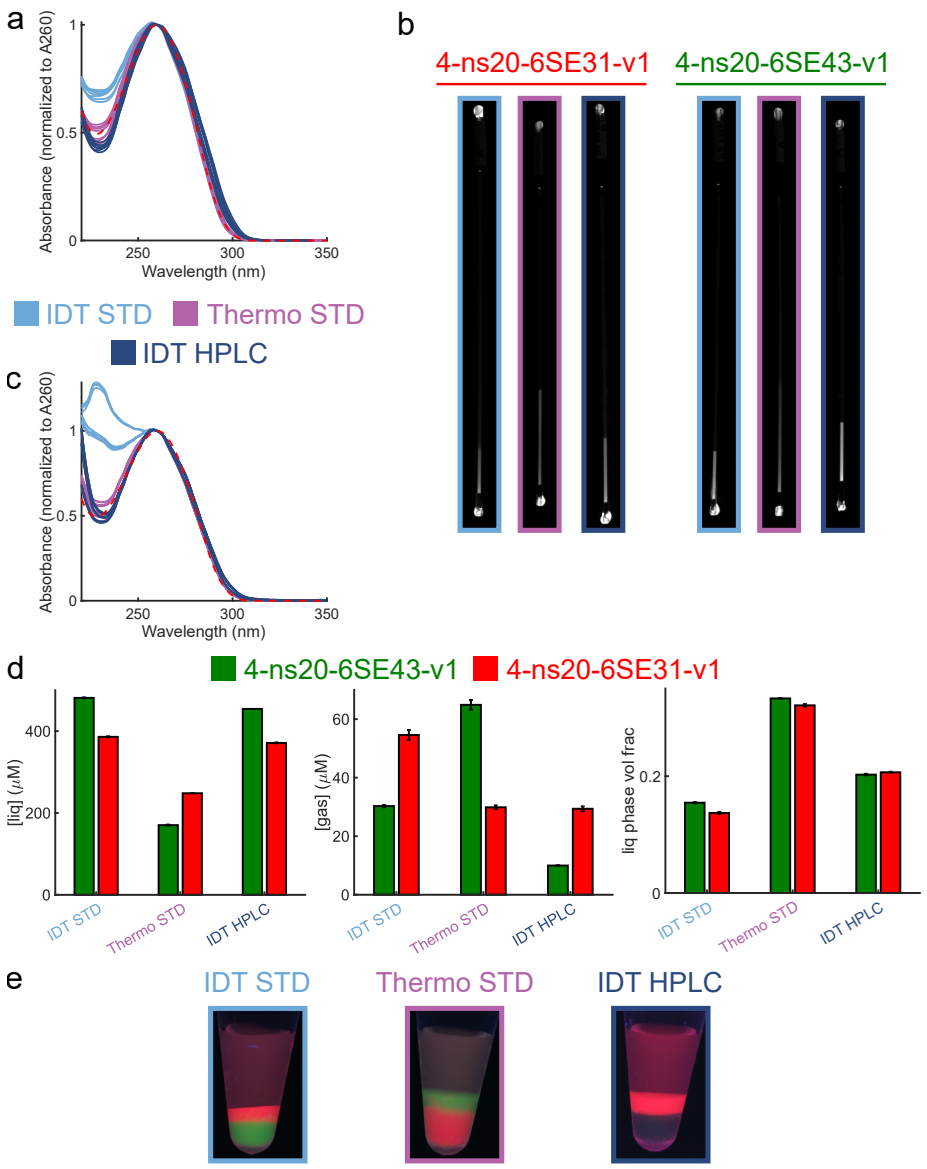

Figure E.1: UV-Vis absorbance spectra of (a) single strands and (c) gas phase. ThermoFisher strands (magenta lines) is more qualitatively similar to IDT HPLC strands (dark blue lines) than IDT STD strands (light blue lines), indicating low benzamide contamination. (b) Images of capillaries filled with solutions of 4-ns20-6SE31-v1 and 4-ns20-6SE43-v1. ThermoFisher samples (outlined in magenta) had larger liquid phase volume fractions compared to IDT STD and IDT HPLC strands. (d) Measurements of the liquid phase concentration (*left*), gas phase concentration (*middle*), and liquid phase volume fraction (*right*) of 4-ns20-6SE43-v1 (green bars) and 4-ns206SE31-v1 (red bars). The order of liquid phase concentrations is reversed when comparing between IDT STD and ThermoFisher strands. (e) Images of liquid layers composed of 4-ns20-6SE43-v1 (dyed green) and 4-ns20-6SE31-v1 (dyed red). The order in which the liquids layer corresponds to the measured liquid phase concentration and demonstrates that the layers flip when comparing between IDT STD and ThermoFisher strands. The fluorescence of the green liquid in the IDT HPLC sample is potentially dim because of G-quenching of the fluorophore.

Appendix F

EFFECT OF ARM LENGTH ON TRANSITION TEMPERATURES

The transition temperature is the temperature at which liquid droplets begin to nucleate. In other words, as shown in Fig 2.1, it is the temperature at which the system moves from the one-phase to two-phase regime. This temperature is different from the melting temperature of nanostars, which is the temperature at which nanostar formation occurs.

Previous studies have shown that the transition temperature increases with increasing sticky end strength and valency (Sato, Sakamto, and Takinoue, 2020). The effect of arm length on transition temperature, however, has not yet been systematically studied. While we did not perform such a study ourselves, we hypothesize that the transition temperature decreases with increasing arm length. Fig F.1a shows a schematic of our hypothesized relationship. We believe that the relationship would be a monotonically decreasing one based on our results in Fig 3.7, where we increased the arm length of a nanostar from 15 bp to 25 bp. At 25 bp, we see poor phase separation of the nanostar, suggesting that the transition temperature of this monomer has decreased below that of other nanostars with shorter arm lengths. The decrease in transition temperature most likely results from increased flexibility of longer arms, resulting in the inhibition of phase separation (Lee et al., 2021). In addition, we suspect that the range of arm lengths under which phase separation can occur depends on the strength of the sticky end.

Fig F.1b shows images of the samples from Fig 3.2 prior to centrifugation. We observe that samples annealed at a rate of 0.1°C/min already demonstrate good layer formation, while those annealed at a rate of 0.5°C/min have a more mixed appearance. This supports our theory that at slow annealing rates, one liquid condenses completely before the other does.

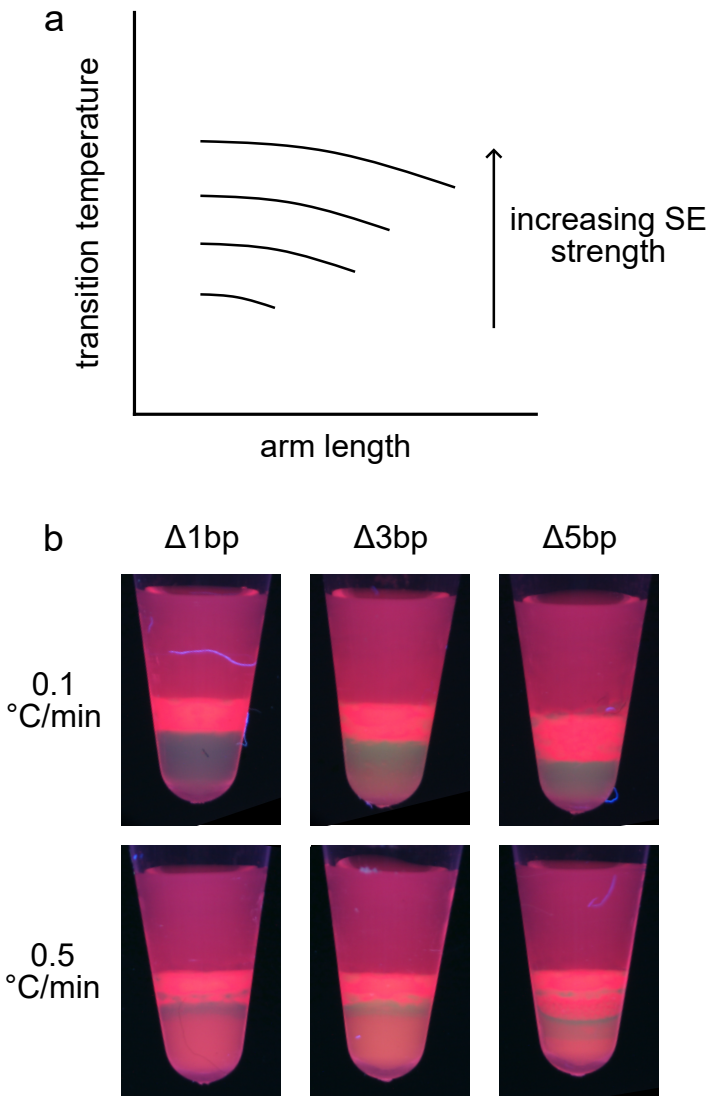

Figure F.1: (a) Schematic demonstrating our hypothesis on the relationship between transition temperatures and nanostar arm length. We expect the transition temperature to decrease with increasing arm length for a giving sticky end sequence. The range of arm lengths under which phase separation can occur depends on the strength of the sticky end.

Appendix G

MEASURED PROPERTIES AS A FUNCTION OF NANOSTAR FEATURES

Fig G.1 shows the measured liquid phase concentration, gas phase concentration, and liquid phase volume fraction as a function of the three nanostar features (arm length, sticky end strength, and valency) we changed. We observe that the liquid phase volume fraction is relatively constant when changing the sticky end free energy (Fig G.1b, rightmost plot). Our expectation from the Lever rule is that if this quantity is held constant, then the liquid and gas phase concentrations should change in some aspect relative to the sticky end free energy. As increasing the free energy of sticky ends should result in more nanostars binding and condensing, the lack of change in the liquid phase volume fraction would suggest that liquid phase concentration should increase.

Based on the weak trend observed in the liquid phase and gas phase concentration plots (Fig G.1b; leftmost and center plots), we consider the possibility that we are in a regime where the dense phase concentration begins to saturate with increasing sticky end strength (Fig G.2). The liquid phase concentration should be limited by the size and geometry of the nanostar. For any given nanostar, we suppose that the maximum liquid phase concentration should occur when all arms of a nanostar are fully bound to other nanostars. The probability of nanostars being fully bound should increase with increasing sticky end free energy (assuming that arm length and valency do not change). Once we have reached a sticky end free energy where all nanostars are bound, increasing the free energy even more should not increase the concentration. We therefore consider the possibility that the sticky end free energy range in Fig G.1b approaches that saturation regime, resulting in the weak trend observed.

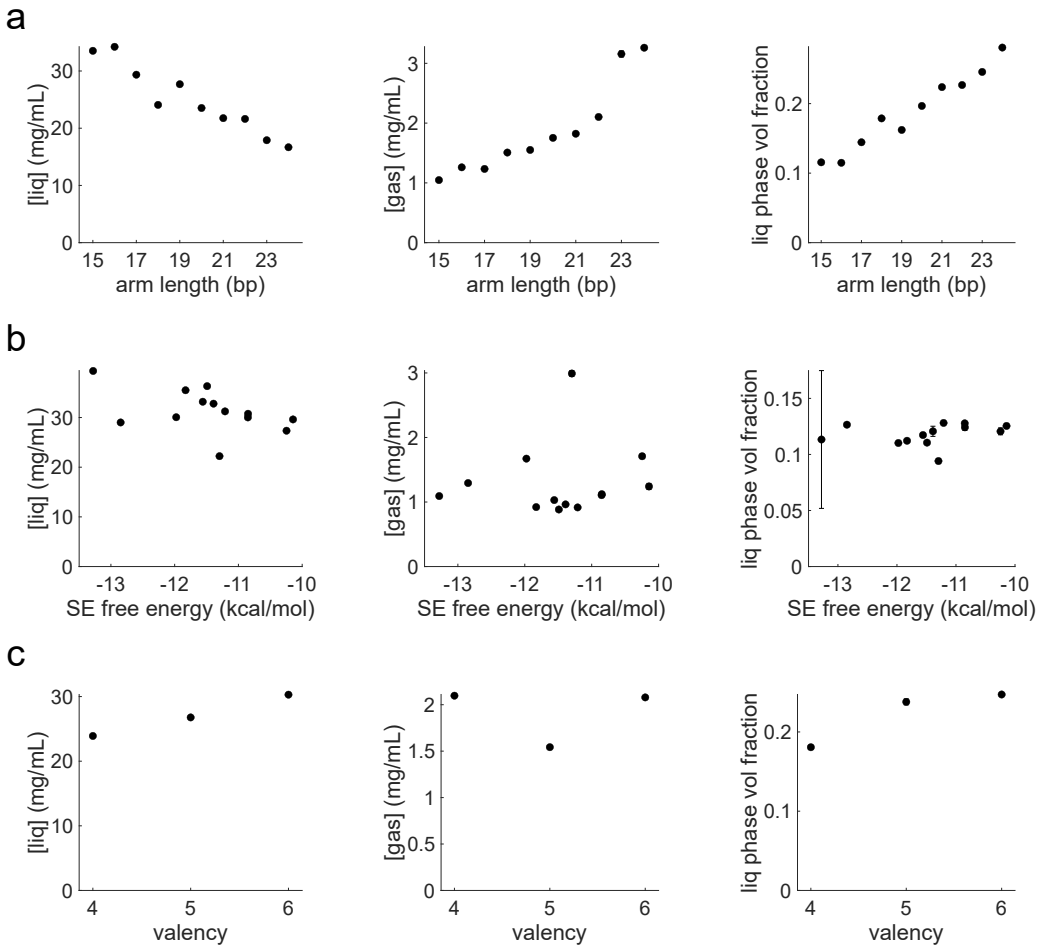

Figure G.1: Liquid phase concentration (*left*), gas phase concentration (*center*), and liquid phase volume fraction (*right*) as a function of (a) arm length, (b) sticky end strength, and (c) valency.

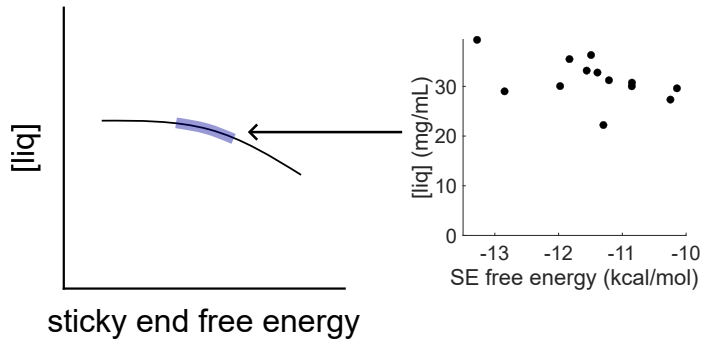

Figure G.2: Schematic of how the liquid phase concentration could potentially saturate with increasing sticky end free energy. The highlighted blue part indicates where our experimental measurements potentially lie within the saturation regime.

Appendix H

LACK OF ORDERING IN THE $[h, s]$ METRIC

Fig H.1 shows plots of LQ as a function of liquid phase concentration differences with non-[6,0] data points colored according to their $[h, s]$ (a), h (b), and s (c) values. [6,0] points are marked with blue crosses. If there were a certain ordering to these values, we would expect to see clusters of points according to their colors. Instead, we observe a uniform distribution of values across the plot, indicating that there is no bias towards any non-[6,0] values with regards to LQ.

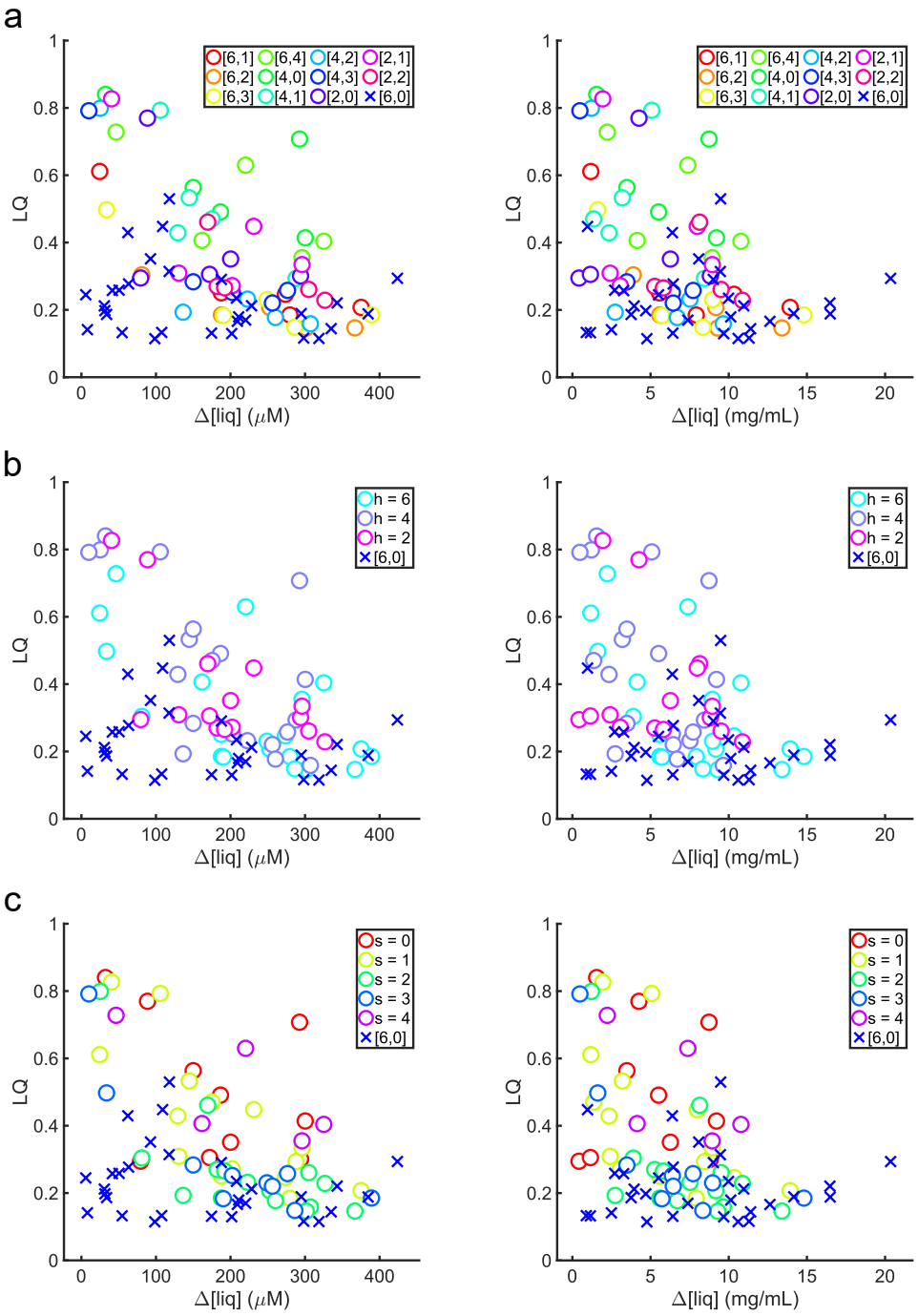

Figure H.1: LQ as a function of liquid phase concentration differences with non-[6,0] values colored according to their (a) [h,s] value, (b) h value, and (c) s value. The lack of clusters indicates that there is no ordering within non-[6,0] values of the $[h, s]$ metric. Concentration is in units of molarity and mass concentration for plots on the left and right column, respectively.

Appendix I

EXTENDED DISCUSSION ON CONCENTRATION TRENDS

We plot the concentrations of the green liquids in Fig 3.11 and Fig 3.13 as a function of arm length for each sticky end (Fig I.1 and Fig I.2). In general, the concentration decreases as arm length increases, which agrees with the results discussed in Section 3.3. We also note that the liquid phase volume fraction increases with increasing arm length, which is an expected result as the increasing monomer size would result in larger volumes of liquid phase.

In these experiments, we used a total nanostar concentration of 100 μM for each arm length. The trends we observed for the liquid phase concentration and volume fraction would then suggest that the gas phase concentration should increase with increasing arm length, as dictated by the lever rule. We instead observe variability in the gas phase concentration trends across all sticky end strengths. These results bolster the idea that variability in the gas phase is a critical flaw in our capillary-based method for measuring concentrations, as discussed in Section 2.3.

We were curious to determine if the change in concentration per basepair was dependent on the sticky end strength. We first assumed that the relationship between concentration and arm length was linear and performed a simple linear regression on each liquid phase concentration plot shown in Fig I.1 and Fig I.2. We plot the calculated slopes as a function of sticky end strength in Fig I.3. Given that the nearest-neighbor model does not accurately predict the free energy of sticky ends, it is difficult to determine if these slopes have a dependency on sticky end strength. At most, we can conclude that the change in concentration significantly increases per basepair when sticky end free energies are less than -13 kcal/mol.

Our initial assumption was that the relationship between liquid phase concentration and arm length was a linear one. Observation of Fig I.4 suggests that is most likely incorrect. Fig I.4 shows the measured gas phase concentration and liquid phase volume fraction used to calculate the liquid phase concentration of Fig 3.6a. We note that while the volume fraction most likely has a linear relationship with arm length (as also suggested by the bottom row of plots in Fig I.1 and Fig I.2), the gas phase concentration appears to have a nonlinear relationship. Based on visual inspection, the relationship is potentially a quadratic or cubic one. This would

suggest that a rational function would best describe the relationship between liquid phase concentration and arm length.

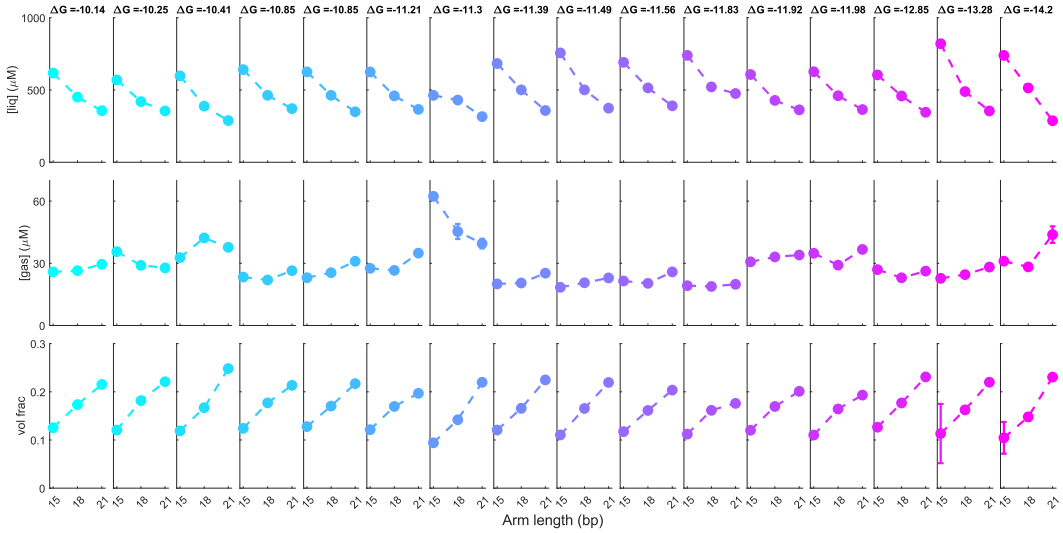

Figure I.1: We plot the liquid phase concentration (top row), gas phase concentration (middle row), and liquid phase volume fraction (bottom row) as a function of arm length for various sticky end free energies, which are written at the top of each column. Concentration units are plotted in units of molarity (μM).

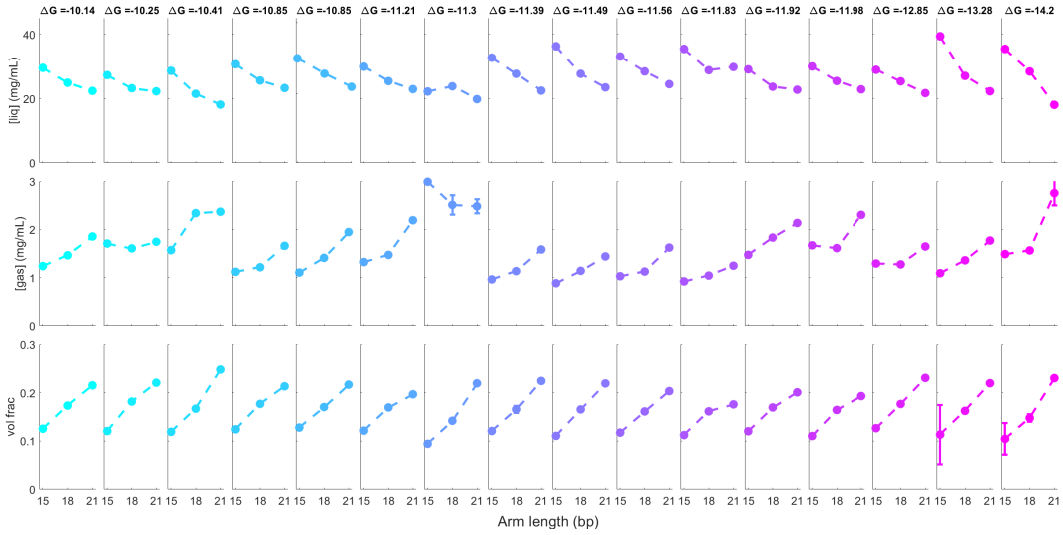

Figure I.2: Same plot as Fig I.2 with concentration units plotted in mass concentration (mg/mL).

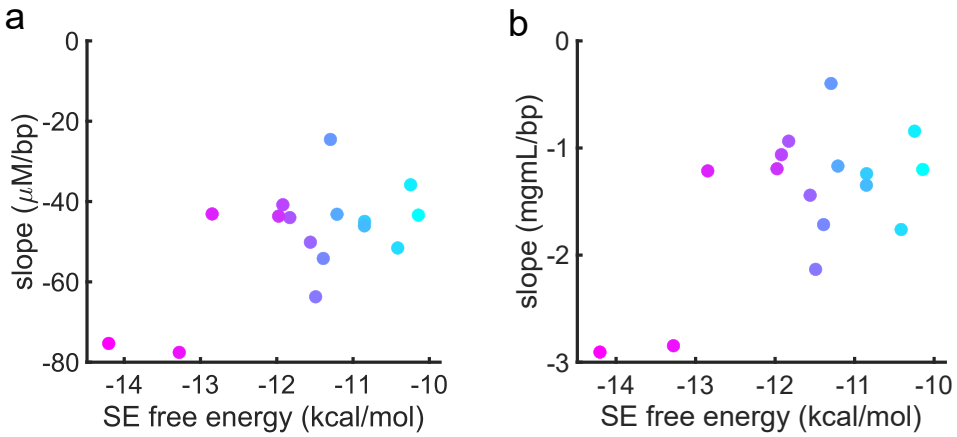

Figure I.3: We plot the change in liquid phase concentration per basepair as a function of sticky end free energy in units of (a) μM/bp and (b) mgmL/bp. Slopes are calculated via a linear fit to liquid phase concentration graphs in Fig I.1 and Fig I.2.

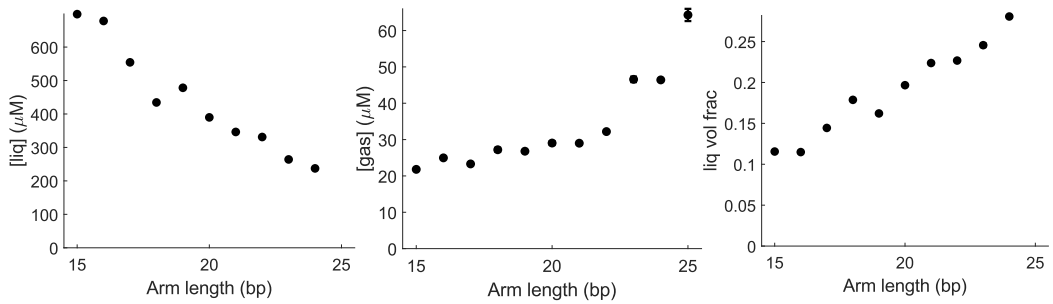

Figure I.4: Gas phase concentration (middle) and liquid phase volume fraction (right) of nanostars from Fig 3.6a (shown on the left again for convenience).

Appendix J

REPRODUCIBILITY OF LAYERING EXPERIMENTS

We repeat the layering experiment shown in the first row of Fig 3.9, i.e., pairs of liquids where nanostars had equal arm lengths to determine the reproducibility of these layers. Qualitatively (Fig J.1 and quantitatively, the layering quality appears reproducible (Fig J.4, top row).

For the Δ3bp and Δ6bp samples in Fig 3.9, we repeated the experiment using different versions of the green liquid nanostars. Fig J.2 and Fig J.3 shows the images of these repeat experiments. Comparison of their LQ values is shown in the middle and bottom row of Fig J.4. Surprisingly, even with different versions of the nanostar, the layering quality appears reproducible both qualitatively and quantitatively. We note that the fluorescence of the green liquid decreases in the repeat Δ6bp samples due to unintentional G-quenching of the fluorophore. The green liquid nanostar for the repeat Δ6bp [6,0] sample did not phase separate well, and we surmise that synthesis quality issues might be a contributing factor.

As we used different nanostars for these layering experiments, we also compared the liquid phase concentration of different nanostar versions (Fig J.5). In general, concentrations are similar across different versions. We attribute any significant differences to sample variability.

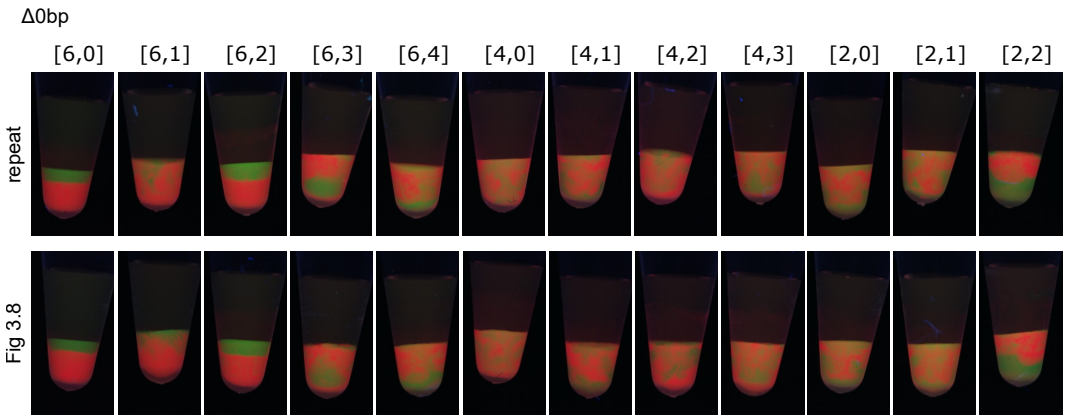

Figure J.1: Bottom row: Δ0bp samples from Fig 3.9. Top row: repeat of the layering experiments in the bottom row using the same version nanostars.

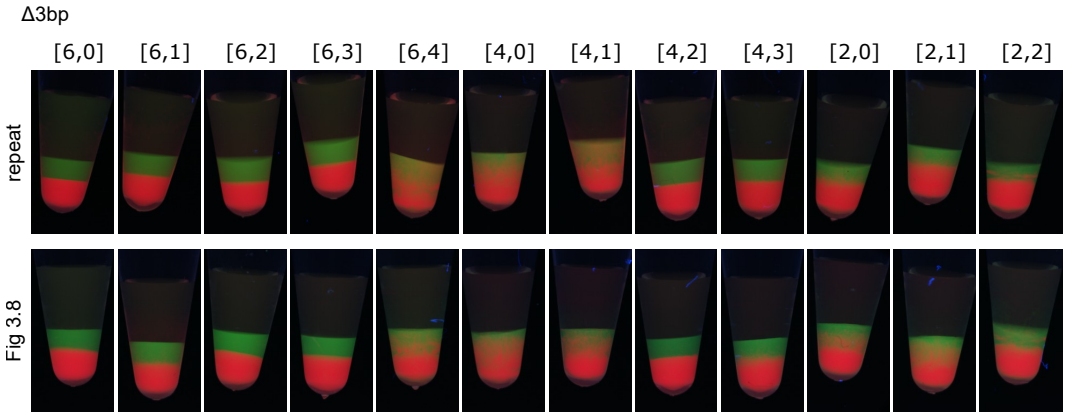

Figure J.2: Bottom row: Δ3bp samples from Fig 3.9. Top row: repeat of the layering experiments in the bottom row using different version nanostars.

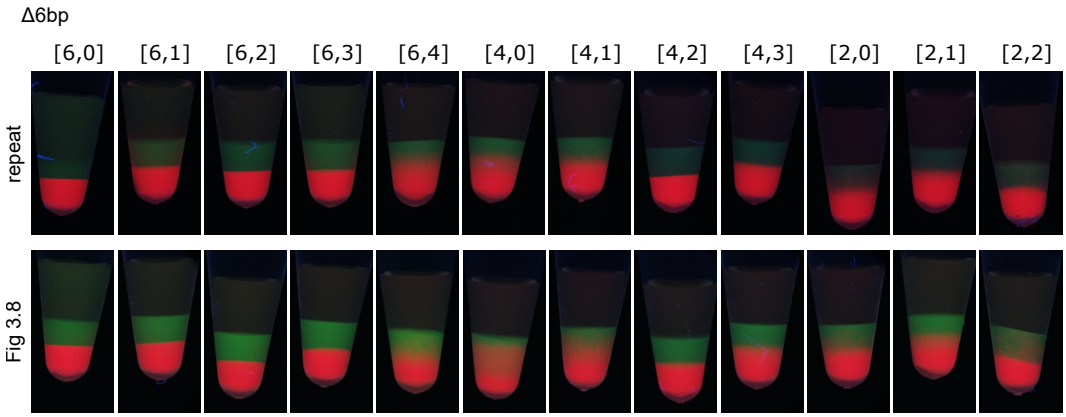

Figure J.3: Bottom row: Δ6bp samples from Fig 3.9. Top row: repeat of the layering experiments in the bottom row using different version nanostars. The fluorescence of green liquids in the repeat samples are dimmer due to unintentional G-quenching of fluorophores. The green liquid nanostar of the [6,0] repeat did not phase separate well.

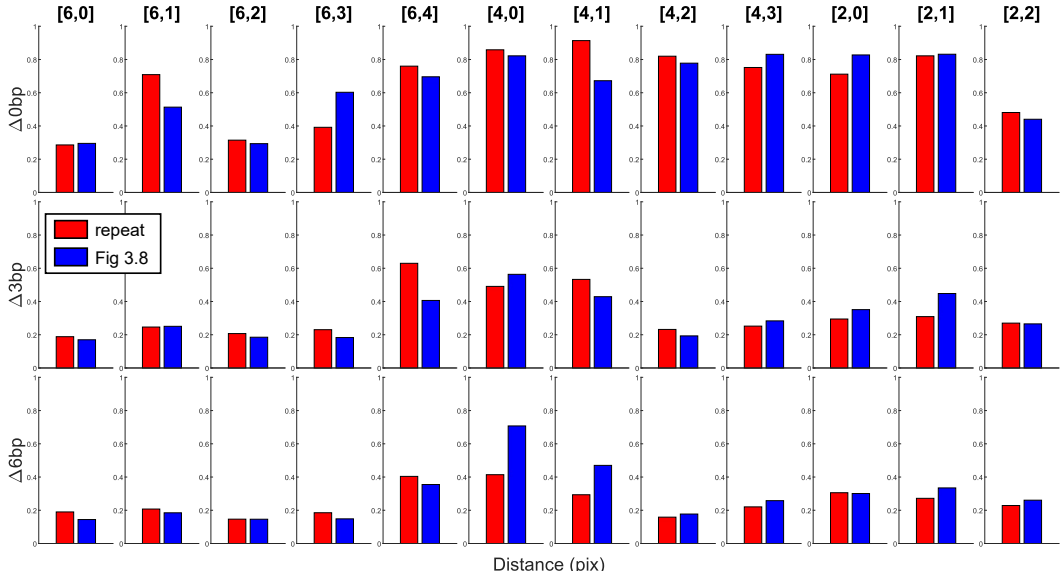

Figure J.4: Comparison of the LQ values from Fig 3.9 (blue bars) and the LQ values from the repeat samples (red bars). LQ value is reproducible across most samples.

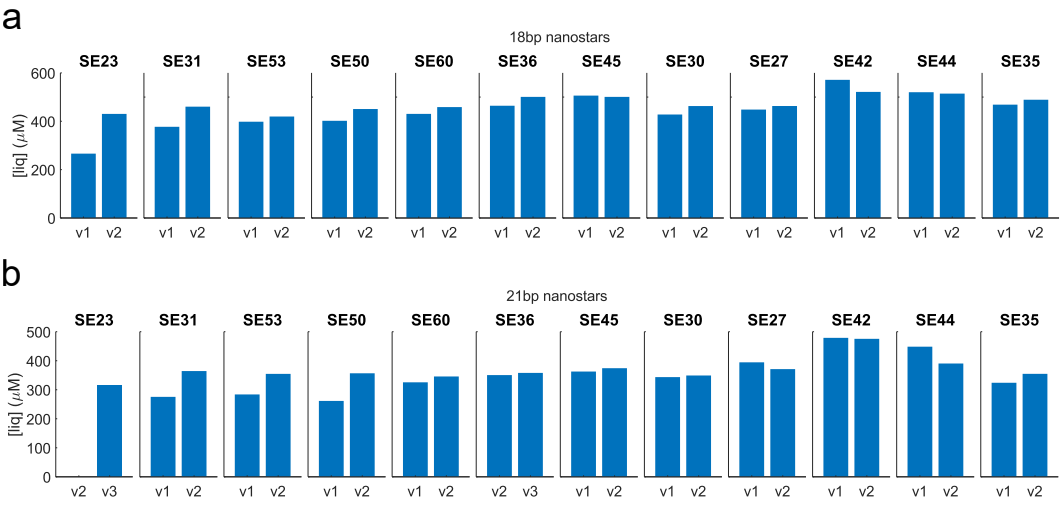

Figure J.5: Comparison of liquid phase concentrations for different nanostar versions with an arm length of (a) 18 bp and (b) 21 bp. We did not measure a concentration for 4-ns21-6SE23-v2 (b, leftmost plot) because it does not phase separate well.

Appendix K

COMPARISON OF $[h, s]$ METRIC AND NEAREST-NEIGHBOR MODEL

Fig K.1a shows LQ as a function of liquid phase concentration differences, but with the points colored according to the free energy of unlike sticky ends binding. We observe that many of the [6,0] points (crosses) tended to have free energies that were more positive compared to non-[6,0] (circles) points. We were curious to know how well the $[h, s]$ metric predicts layering quality in comparison to free energies as calculated by the nearest-neighbor model. In other words, is there a free energy threshold where the nearest-neighbor model predicts better than the $[h, s]$ metric?

Fig K.1b shows this comparsion using the dataset from Fig K.1a. Blue dots represent the fraction of sticky end pairs whose free energy is greater than the threshold free energy (x-axis) that had an LQ estimated to be greater than 0.3. Red dots represent the fraction of sticky end pairs whose free energy is less than or equal to the threshold that had an LQ estimated to be less than or equal to 0.3. In other words, the blue and red dots represent how often false negatives and false positives are predicted, respectively, based on the chosen threshold free energy. Blue and red dashed lines correspond to fraction of false negatives and positives with the $[h, s]$ metric, respectively. The number of false negatives predicted by $[h, s]$ (blue dashed line) is always less than the number of false negatives predicted by the nearest-neighbor model except around a free energy of -5 kcal/mol. We suspect that this improvement is due to the small sample size of sticky ends with this particular free energy (see Fig K.1c). On the other hand, the number of false positives predicted by $[h, s]$ (red dashed line) is more than that predicted by the nearest-neighbor model up until a threshold free energy of -6 kcal/mol. These facts taken together suggest that the $[h, s]$ metric is better than the nearest-neighbor model at predicting when layering quality will be high, but not when it will be low. We emphasize that this error analysis is made within the limited set of data points from Fig K.1a (n = 87), and this conclusion may not hold with a larger data set.

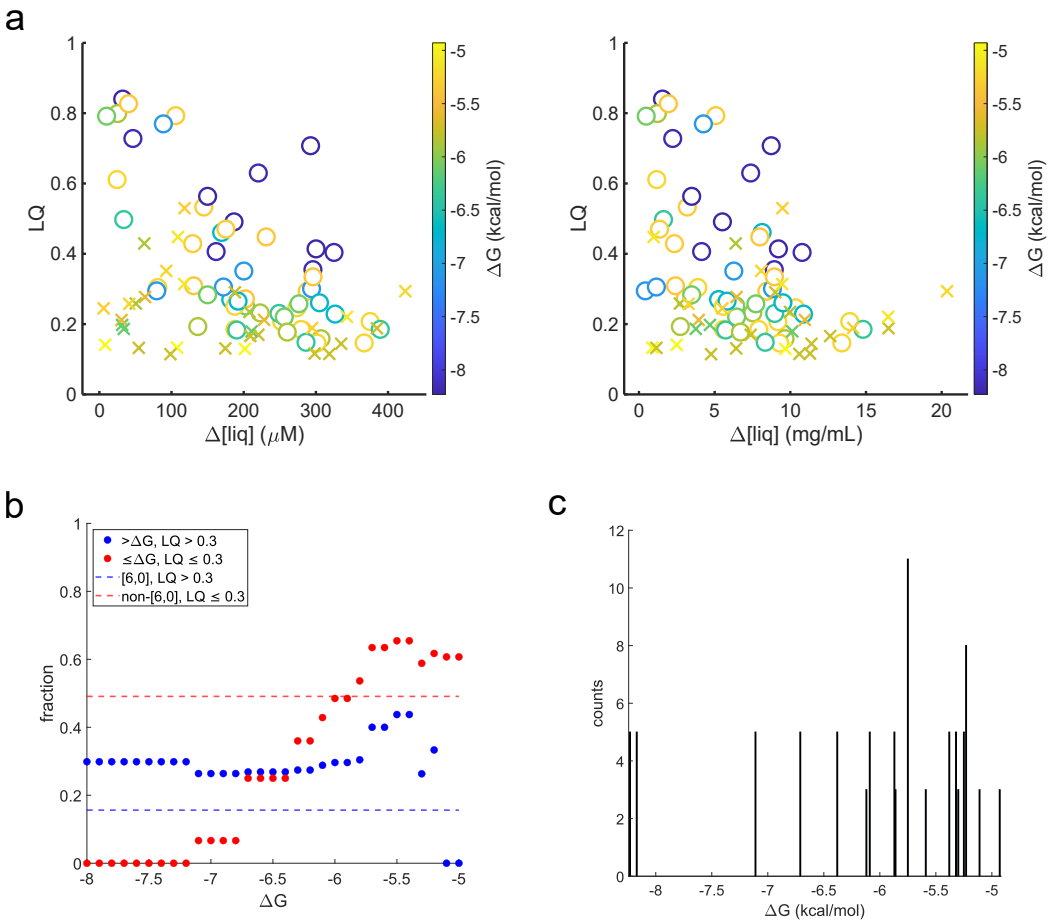

Figure K.1: (a) LQ as a function of liquid phase concentration differences in units of molarity (*left*) and mass concentration (*right*). Points are colored based on the free energy of unlike sticky ends binding. Crosses are [6,0] and circles are non-[6,0] data points. (b) Fraction of sticky ends predicted to be false negatives (blue dots) and false positives (red dots) according to a threshold free energy (x-axis). Dashed blue and red lines indicate the fraction of sticky ends predicted to be false negatives and positives, respectively, according to the $[h, s]$ metric. (c) Distribution of the sticky end free energies from (a).

Appendix L

LQ CALCULATIONS FOR FIVE LAYERS

The interfaces between each layer are angled differently in the five layer liquids shown in Fig 3.16. As a result, we could not draw a single rectangle across all layers. We instead drew separate rectangles (Fig L.1) for each interface to calculate LQ for each adjacent layer.

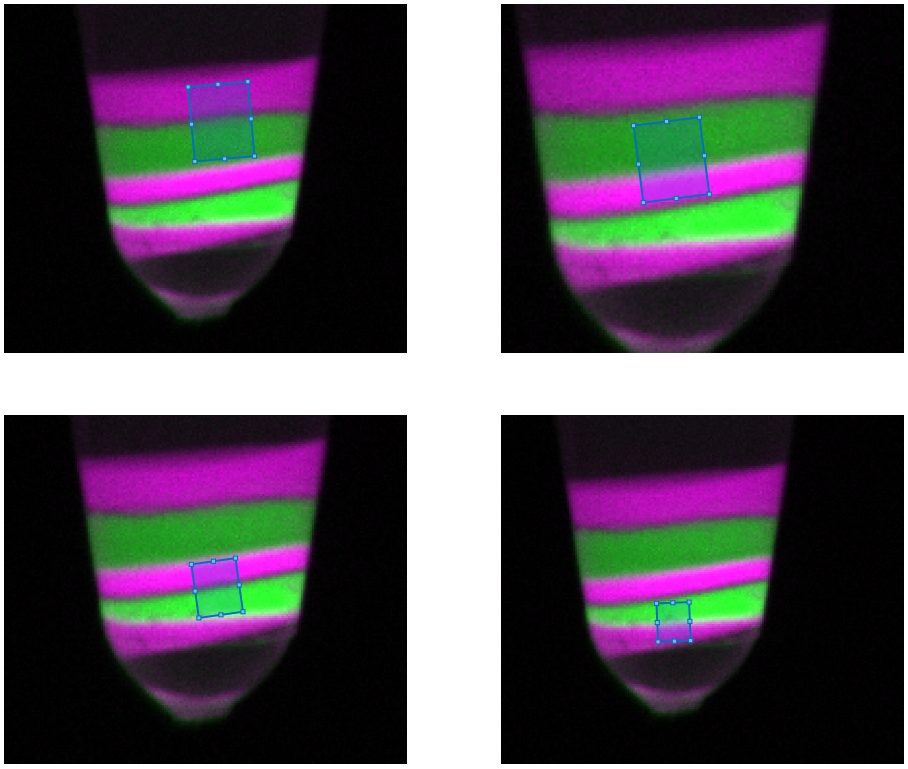

Figure L.1: We drew separate rectangles for each adjacent layer to avoid averaging over interfaces that were not parallel to each other.

Appendix M

EFFECT OF STOICHIOMETRY ON LAYERING QUALITY

Benzamide contamination of STD strands could potentially affect stoichiometric ratios and thereby the liquid phase concentration. As these liquids layer according to their densities, we explored how intentionally varying the stoichiometry of strands could potentially affect layering order and quality of liquids. This would illuminate the robustness of layer formation to stoichiometric changes, especially if one were to use STD strands.

Using nanostars from the experiment in Fig 3.12, we varied the concentration of one strand of 4-ns15-6SE21-v2 (dyed red in Fig M.1) from 0.5X to 1.5X (1X = 83.2 μM), while keeping all other strands at 1X and pairwise layered it with 4-ns15-6SE44-v1 and 4-ns21-6SE44-v2 (both dyed green in Fig M.1), whose strand concentrations were kept constant at 1X in all samples. As the layering order of 4-ns15-6E21-v2 relative to these two nanostars is opposite between the two (see third column, first and bottom row of Fig 3.12), changing the strand stoichiometry of 4-ns15-6SE21-v2 should result in different behaviors between the two pairs.

Fig M.1a and b show images of the layers containing 4-ns15-6SE44-v1 and 4-ns21-6SE44-v2, respectively. The LQ of each image is written at the top (white text). In samples containing 4-ns15-6SE44-v1, we observe that variations in the strand concentration of the red liquid does not change the layering order or quality, with the exception that the red liquid does not phase separate well at 0.5X. This indicates that for appreciable phase separation of the liquid on the macroscopic scale, the relative ratio of strand concentrations for a single nanostar should be no less than 0.75 at the very least. The lack of change for this pair of liquids across all strand concentrations is not entirely unexpected. Since the red liquid layers on top of the green when all strands have a 1:1 ratio, any changes in stoichiometry would result in lowering the density, as nanostars with a missing strand essentially form an $n-2$ valency nanostar (lower valency contributes towards lowering the density) and excess strands might inhibit sticky end interactions; therefore, the order of liquids would not change with varying strand concentration of the red liquid. Layering quality would also not change as a function of this strand concentration since the density difference between liquids would hypothetically be increasing. Potentially,

layering quality could have been affected by the possibility of malformed nanostars interacting with the other nanostar species in solution; however, if this phenomenon is occuring, it appears negligible given the consistent LQ value across all samples.

We observe a similar behavior for samples containing 4-ns21-6SE44-v2 when varying strand concentration from 0.5X to 1.25X. When the strand concentration was increased to 1.5X, we observe that the interface between the two liquids becomes blurred and that there is a thin "strip" of red liquid on top of the green. We again believe that the excess strands might inhibit sticky end binding, thus resulting in a decrease in liquid phase density. The thin "strip" of red liquid observed further suggests that some portion of the red liquid is already less dense than the green one. At 1.5X, the density of the red liquid approaches that of the green and the two liquids potentially cannot separate as well under the centrifugation speed used.

These results suggest that the layering behavior of these particular pairs of liquids are quite robust when varying the concentration of a single strand from 0.75X to 1.25X. In a realistic setting, the use of STD strands would most likely result in varying concentration ratios between all strands. We suspect that if we had varied the concentrations of more than one strand at various ratios, layer formation would not be as robust. In addition, we hypothesize that liquids that are closer in density when strand concentration ratios are 1:1 could be more affected by small changes in stoichiometry, as any small changes in density could cause them to mix or flip in order.

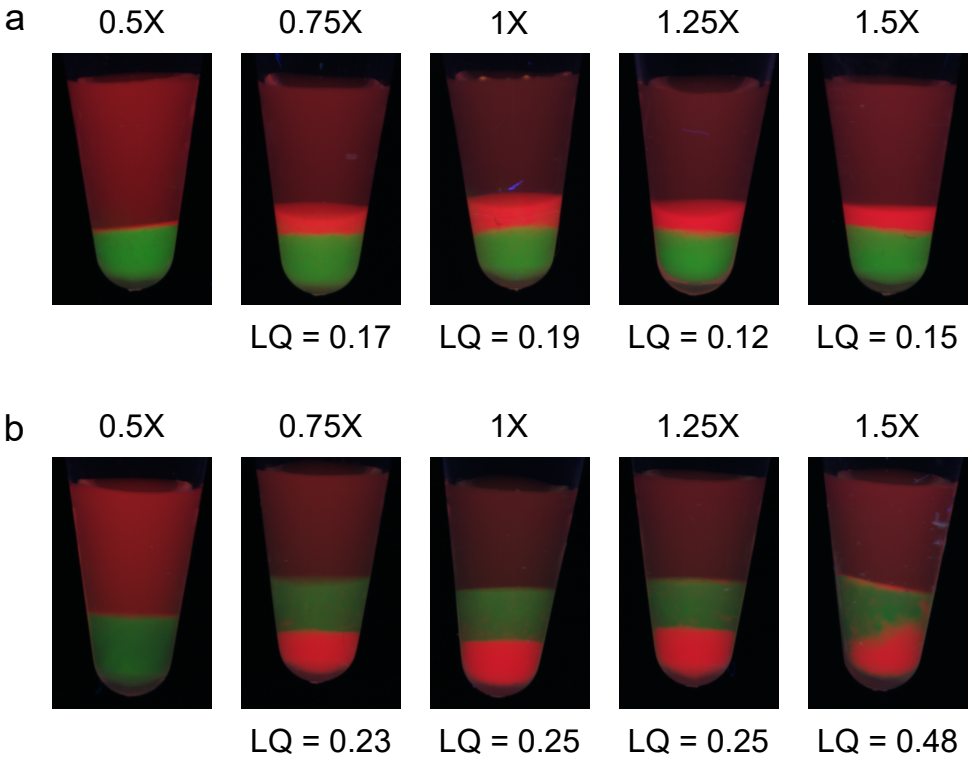

Figure M.1: Effect of stoichiometry on layering quality. Pairwise liquids of red liquid nanostar 4-ns15-6SE21-v2 with green liquid nanostars (a) 4-ns15-6SE44-v1 and (b) 4-ns21-6SE44-v2. The concentration of one strand of 4-ns15-6SE21-v2 is varied from 0.5X to 1.5X (1X = 83.2 μM). In general, layering order and quality is robust to variations in the concentration of a single strand from 0.75X to 1.25X. In b, when strand concentration is at 1.5X, the density of the red liquid potentially approaches that of the green, resulting in a more blurred interface as the two liquids are potentially somewhat mixing. We did not calculate LQ values for 0.5X samples since the red liquid did not phase separate.